Diss. ETH No. 19529

Modeling and Analysis of the Magnetization, Torque and Dynamics of Untethered Soft-Magnetic Microrobots

A dissertation submitted to
ETH ZÜRICH

for the degree of
Doctor of Sciences ETH

presented by
ZOLTÁN GYÖRGY NAGY
Dipl. Masch.-Ing. ETH
born 16 September 1980
citizen of Luxembourg

accepted on the recommendation of
Prof. Dr. Bradley J. Nelson, examiner
PD. Dr. ir. habil. Remco I. Leine, co-examiner

2011

Magnetism is one of the Six Fundamental Forces of the Universe, with the other five being Gravity, Duct Tape, Whining, Remote Control, and The Force That Pulls Dogs Toward The Groins Of Strangers.

Dave Barry (b. 1947) American author and columnist

Abstract

Untethered microrobots, that is, autonomous mobile devices with principle dimensions in the sub-millimeter range, can provide a means for advanced diagnostic and therapeutic procedures inside the human body. To power and drive such microrobots wirelessly, externally applied magnetic fields are seen most promising due to their long range. Several methods have been proposed for actuation, classic pulling with magnetic field gradients, bio-inspired cork-screw type motion, or more ingenious methods involving stick/slip behavior on a surface or impact driven propulsion. This thesis investigates two types of untethered soft-magnetic microrobots. One is assembled from multiple individual planar shapes. In an applied field their magnetization may interact and produce a complex behavior, unpredictable by current methods. Here, we propose a method to compute their magnetization faster than the standard method, while still yielding precisely the same results. In addition, the proposed description allows for the semi-analytical treatment of the magnetization to gain further insight. This description is then used to investigate the resulting torque on assembled shapes, and we show that linear superposition holds well. Second, we introduce non-smooth multi-body dynamics to describe the complex motion of microrobots involving stiction, sliding and impact. Because of the low mass and, thus, high resonant frequencies, it is extremely difficult to analyze these motions experimentally, and numerical solutions are required for analysis. We apply the theory to the Wireless Resonant Magnetic Microactuator and integrate its non-smooth and non-linear equations of motion numerically using Moreau's mid-point integration scheme. Our results are qualitatively consistent with experimental results, and predict several non-intuitive phenomena, such as switching of the direction of the velocity with changing excitation frequency. This thesis provides the reader with practical knowledge on how a particular magnetic device will behave in magnetic fields and field gradients. From an engineering perspective, we provide methods and results that help develop intuition and which guide during the design and actuation of complex untethered soft-magnetic microrobots.

Zusammenfassung

Ungebundene Mikroroboter, d.h Roboter deren Hauptmasse im Submillimeter Bereich liegen, können neuartige Möglichkeiten für medizinische Diagnose und Eingriffe im menschlichen Körper bieten. Wegen ihrer grossen Reichweite scheinen von aussen angelegte Magnetfelder sehr erfolgsversprechend um solchen Robotern kabellos Energie zuzuführen oder sie zu steuern. Mehrere Methoden für solche Antriebe wurden bereits vorgeschlagen: klassisches Ziehen mit magnetischen Feldgradienten, von biologischen Systemen inspirierte Korkenzieher-ähnliche Fortbewegung, aber auch ausgeklügeltere Methoden basierend auf Haft/Gleit Übergänge auf einer Oberfläche oder Fortbewegung basierend auf Stössen. Die vorliegende Arbeit untersucht zwei Arten von ungebundenen weichmagnetischen Mikrorobotern. Einerseits, solche die aus mehreren planaren Formen zusammengesetzt werden. Im angelegten Magnetfeld kann deren Magnetisierung interragieren und ein komplexes Verhalten erzeugen, was durch vorhandene Methoden nicht vorhersagbar ist. Hier wird zunchst eine Methode vorgeschlagen um die Magnetisierung einer einzelnen Form schneller zu berechnen als mit der Standartmethode, während gleichzeitig das gleiche Ergebnis erreicht wird. Zusätzlich erlaubt die vorgeschlagene Beschreibung lineares und gesättigtes Verhalten analytisch mit einer einzigen Formel zu betrachten. Diese Beschreibung wird dann verwendet um das magnetische Moment, das auf die zusammengesetzte Formen wirkt zu untersuchen, und wir zeigen dass die Annahme von linearer Superposition vernünftig ist. Zweitens wird die komplexe Fortbewegung von Mikrorobotern basierend auf Haften, Gleiten und Stössen mit nicht-glatter Mehrkörperdynamik beschrieben. Wegen den kleinen Massen und die daraus resultierend grossen Resonanzfrequenzen ist es praktisch unmöglich diese Bewegungen experimentell zu untersuchen, und numerische Lösungen bieten die einzige Möglichkeit für die Analyse. Die Theorie wird auf den *Wireless Resonant Magnetic Microactuator* angewandt und die nicht-glatten und nicht-linearen Bewegungsgleichungen werden basierend auf Moreau's Mittelpunkt Integrationsschema numerisch integriert. Die Resultate sind qualitativ konsistent mit experimentellen Beobachtungen und sagen mehrere nicht intuitive Verhalten, wie z.B. das Wechseln der Geschwindigkeitsrichtung mit wechselnder Anregungsfrequenz, vorher. Im Allgemeinen bietet die vorliegende Arbeit dem Leser praktisches Wissen wie sich ein magnetischer Mikroroboter in Magnetfeldern und Magnetfeldgradienten verhalten wird. Der ingineur-mässige Ansatz bietet Verfahren und Resultate um Intuition für Auslegung und Aktuierung von komplexen ungebundenen weichmagnetischen Mikrorobtern aufzubauen.

Acknowledgements

You'll Never Walk Alone and many many people have been accompanying me on the way to finishing or prolongating this thesis. In particular, I wish to express my gratitude to

Dr. Bradley Nelson, for providing the big picture for my research and putting it into the right context. Dr. Nelson has this incredible talent to motivate and to create a work environment that is just fun to work in;

Dr. Remco Leine, who has sparked my interest in the beauty of complex mechanical systems, and always had an open door for inspiring discussions on multi-body dynamics;

Dr. Jake Abbott, for motivating me to dig further and further into magnetic modeling. Much of Chapters 2 and 3 would not have been possible without his steady encouragement;

my colleagues providing experimental validations for my mostly theoretical results. I have had excellent support from Olgaç Ergeneman, Salvador Pané i Vidal and Michael Kummer for Chapter 3, and Dominic Frutiger for Chapter 4;

my officemates, (in order of graduation) Chauncey—*the fly*—Grätzel, Dominic—*the paranoid*—Frutiger, and Christos—*the bergy*—Bergeles, who over the years have become good friends. Of course, the same holds true for the rest of the IRIS group, and numerous excellent BSc, MSc, and summer intern students, that I have had the pleasure to advise.

Last but most importantly, many thanks to my family, and especially my girlfriend Julie for all those things that really matter in life.

Contents

List of Figures

List of Tables

This almost makes me want to learn how magnets work.

Bart Simpson - [making Skinner dance with magnets]

CHAPTER 1

Introduction

1.1 Microrobotics

The terms microrobotics or microrobots are widely and elastically used without a precise definition. Yet, two main directions can be identified depending on the use of the prefix *micro*. On one hand, in its etymological sense[1] to designate something generally small or minaturized, i.e., smaller than the scope of focus. On the other hand, capitalizing on the fact that *micro* is a prefix in the SI unit system (symbol μ) designating one millionth (10^{-6}), objects (e.g. organisms, robots) that have principal dimensions or structures in the micrometer (µm) range may be referred to as microobjects (e.g. microorganisms, microrobots).

Historically, microrobots designate robots that are generally small, typically having volumes of a few cm^3. These robots are fabricated traditionally, by mechanical assembly of very small components, i.e. bolts, screws, microchips etc. The reason to call these robots microrobots is because during their development the focus is laid on their small size. Research is focused on using smaller components, sophisticated assembly techniques and algorithms to allow the robots to deal with their limited functionality. Examples of such robots are the one cubic-inch robot presented by Flynn et al. [1989] or the sugar-cubed mobile microrobot Alice by Caprari et al. [2002] (Figure 1.1).

In the 1990s, the advancement of microtechnology, i.e., the processes used to fabricate integrated circuits (ICs) such as photolithography, electroplating and various etching and deposition methods, made actuated structures, such as cantilevers and membranes at the microscale possible. The terms microactuators and microrobots were coined to designate devices created by these microfabrication techniques. As an extension to this, large systems having working dimensions in the microscale are also commonly referred to as

[1] from ancient greek *μικρός*, mikros, "small"

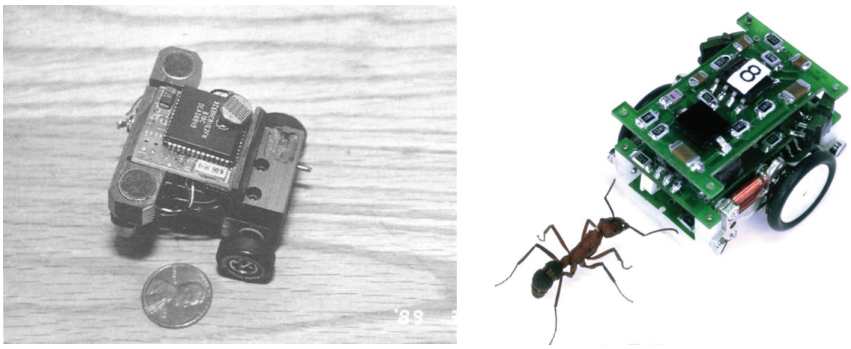

Figure 1.1: MIT's cubic-inch robot (left) and EPFL's sugar-cubed mobile microrobot (right) are examples where *micro* is used as designating *very small* in general

micro- or nanorobotic systems. In this work, we will employ this latter, scale-based, definition. For the interested reader, Abbott et al. [2007b] provide a tutorial type introduction to microrobotics.

1.1.1 Potential Applications

Traditionally, large robots are used in areas that are too dangerous or unreachable for humans, e.g. deep-see or space exploration. In addition, widespread industrial applications of robots include high-speed and precise manipulators with several degrees of freedom to perform specific preprogrammed tasks, such as welding, assembly, painting, etc.

Extending this scheme to microrobots, two possible areas of applications can be identified:

Microhandling or microassembly of microscopic objects. Here, microrobots can be seen as end-effectors that are able to move and operate with extremely high, near atomic, precision. In addition, microassembly may allow for advanced fabrication techniques. Gauthier and Regnier [2010] summarize the challenges and opportunities for this, and Cohn et al. [1998] give an overview of various microassembly technologies.

Medical applications of microrobots are thought to have a large impact on society. According to Nelson et al. [2010] the trend in medicine is towards smaller devices and components to reduce recovery times and risks for the patients; and untethered microrobots can provide a means for advanced diagnostic and therapeutic procedures inside the human body. See Fig. 1.2 for examples of possible medical applications of microrobots.

1.1.2 Microactuation Principles

Because of their limited size, microactuators are often made of smart materials, where one physical quantity is transduced into another one due to

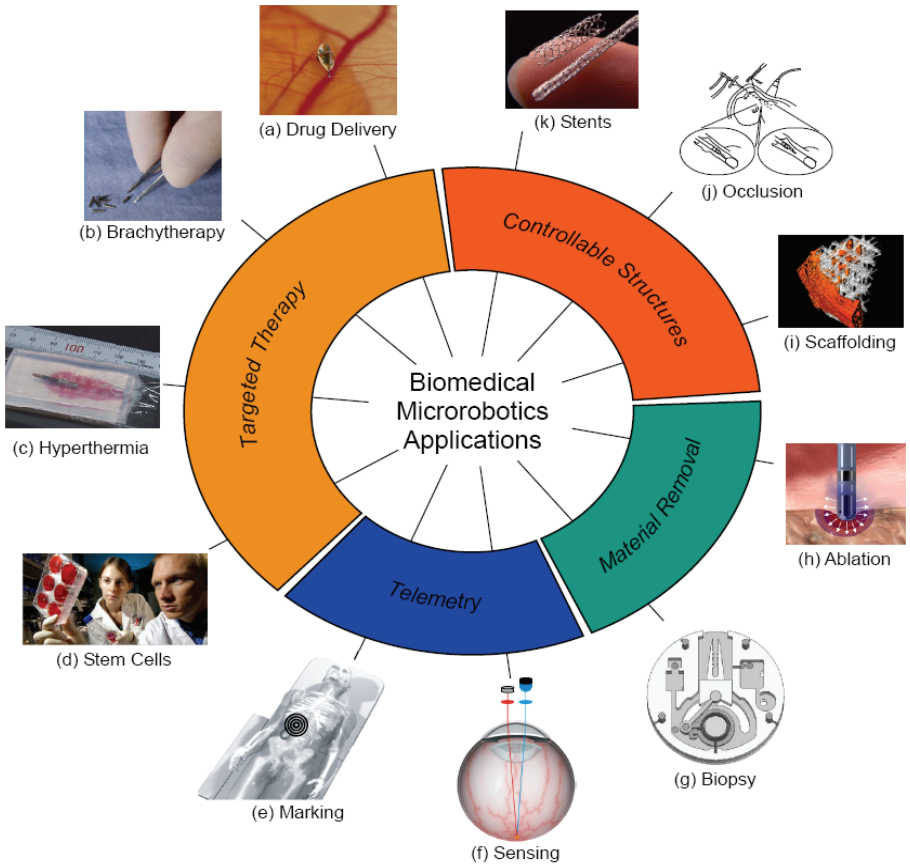

Figure 1.2: Possible medical applications of microrobots, adapted from [Nelson et al., 2010]

the properties of the material. Examples of such smart material behavior are piezoresistive, thermomechanical, piezoelectric, shape-memory alloys, electroactive polymers, etc. A thorough overview is beyond the scope of this work but there are extensive reviews in literature available that present and compare microactuation technologies, see for example Breguet et al. [2006]; Dario et al. [1992]; Fujita [1995]; Liu et al. [2010]; Madden et al. [2004] and references therein.

One actuation technique capitalizes on the electrostatic interaction between polysilicon components to create, e.g., micromotors and resonant microstructures. State of the art reviews on modeling electrostatic interaction are given for example by Batra et al. [2007] and Chuang et al. [2010]. The inherent limitation of electrostatic actuators is their small travel range which depends on the distance between two opposing plates. Continuous linear and rotational motion, a key requirement for autonomous microrobots, has been been made possible by the scratch drive actuators introduced by Akiyama and Shono [1993] (Fig. 1.3(a)). This concept has been refined and

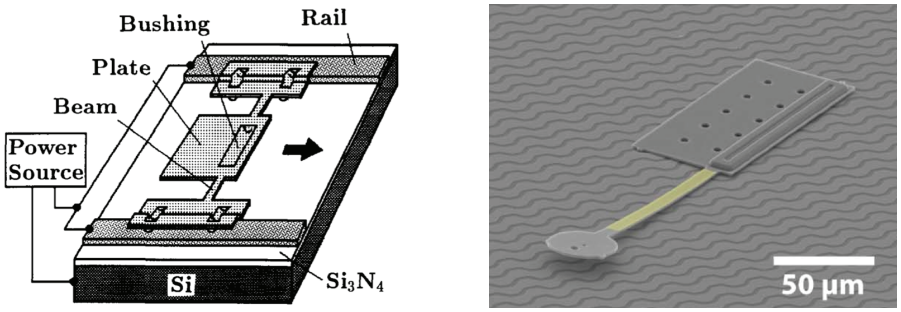

(a) Scratch drive introduced by Akiyama and Shono [1993]

(b) Untethered microrobot presented in Donald et al. [2008]

Figure 1.3: Electrostatically actuated microrobots

researched through the years and optimized to devices capable of nanometer positioning [Linderman and Bright, 2001].

Yet, scratch drive actuators still require tethers, such as, guiding rails for both power and motion, making arbitrary motion impossible. By using a surface with individually addressable electrodes to partially and temporarily fix the actuator, the first electrostatic untethered microrobots were proposed by Donald et al. [2003]. The same group then demonstrated arbitrarily steerable electrostatic microrobots on a planar surface [Donald et al., 2006], and multiple individually controllable planar microrobots in Donald et al. [2008] (Fig. 1.3(b)).

1.2 Wireless Magnetic Microrobots

Wireless microrobots that are capable of navigating bodily fluids to perform localized sensing or targeted drug delivery will open the door to a variety of new diagnostic and therapeutic procedures. These untethered devices can be used in parts of the body that are currently inaccessible or too invasive to access. Energy storage and onboard actuation mechanisms at the scale of these microrobots are currently insufficient to generate the forces and torques required to move through bodily fluids.

Due to their large range (larger than electrostatic fields), the most promising method of providing wireless power and control for such *in vivo* microrobots is through magnetic fields generated by external sources. Also, as reviewed by Gillies et al. [1994], magnetic fields have a long history of handling objects inside the human body, which further motivates their use for powering and propelling microrobots.

In addition to powering, when moving in fluids at the microscale, one has to face low Reynolds number flow regime. In this regime, as detailed by Purcell [1977], inertia and time are negligible. This means that symmetri-

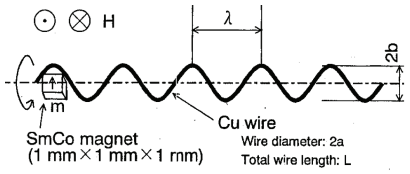

(a) Schematic view of the spiral-type swimmer presented by Honda et al. [1996]

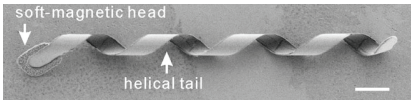

(b) Artificial bacterial flagella introduced by Zhang et al. [2009a]. The length of the scale bar is 4µm.

Figure 1.4: Bio-inspired microrobots mimic a rotating flagella and actuated by rotating magnetic fields

cal propulsion methods, such as employed by fish, will not lead to propulsion because the forward and backward motion pattern is the same. He then also proposes successful swimming mechanisms comprising a flexible oar and a corkscrew type motion and derives their propulsion matrix, the linear relationship between the rotational and linear velocity of the swimmer. His work is in close relation to the discovery by Berg [1973] that the Escherichia coli bacteria swims by rotating its flagella.

Following this example of nature, asymmetric propulsion methods have been proposed, most prominently helical swimmers such as those introduced by Honda et al. [1996]. The swimmer consists of a $1mm^3$ magnet attached to a copper wire formed into a helical shape. The robot is propelled by external magnetic fields which exert a torque on the magnet. Rotating the magnetic field thus induces rotation of the magnet and consequently of the whole robot which is then propelled forward (Fig. 1.4(a)).

Recently, artificial bacterial flagella (ABF) were introduced by Zhang et al. [2009a]. The tail of the ABF is a helical structure made from InGaAs/GaAs/Cr layers while the rectangular head is electroplated nickel. In a homogeneous rotating magnetic field, the head will tend to align itself with the magnetic field thereby inducing a rotation on the tail which then propels the ABF forward. The ABF has been characterized [Zhang et al., 2009b] and successful micromanipulation has been demonstrated by Zhang et al. [2010] (Fig. 1.4(b)).

In addition to such bio-inspired solutions, the more classical approach of translating and rotating a magnetic body using external magnetic fields has also been investigated. A magnetic levitation system has been presented by Elbuken et al. [2009]. It consists of seven electromagnets connected by a pole piece that are used to levitate permanent magnet structures in space. The structures have a microgripper attached to them that is actuated thermally by focusing laser light onto it. Successful levitation and micromanipulation with commercial NdFeB magnets as well as Co-Ni-Mn-P film structures has been reported (Fig. 1.5(a)).

A magnetic microrobot that has been assembled from multiple thin electroplated nickel parts has been studied by Yesin et al. [2006]. Forward propul-

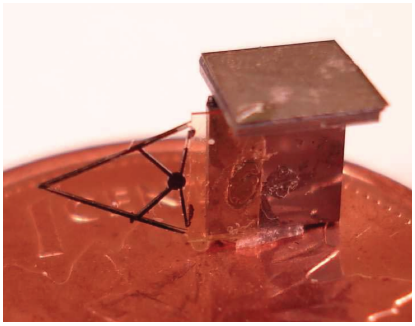

(a) Levitating microrobotic system from Elbuken et al. [2009]

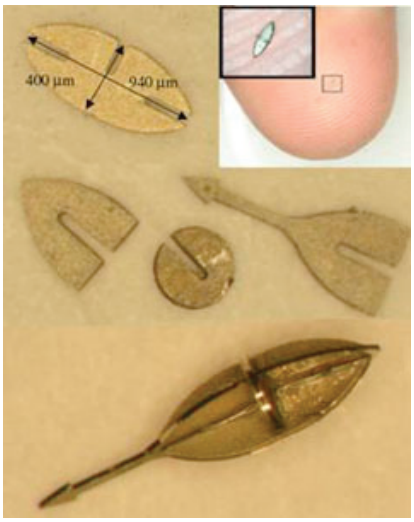

(b) A magnetic microtobot assembled from muiltiple thin nickel parts studied by Yesin et al. [2006]

Figure 1.5: A classic microrobotic propulsion method is to apply magnetic fields.

sion was achieved by applying a magnetic field gradient through a pair of Maxwell coils. For rotation of the robot, a magnetic torque is generated using the magnetic field of a Helmholtz coil pair. The microrobot was successfully moved wirelessly through a maze. The magnetic and hydrodynamic properties of the microrobot have been measured [Kummer et al., 2007], and a system comprising eight electromagnets for 5-DOF[2] wireless micromanipulation has been recently demonstrated [Kummer et al., 2010] (Fig. 1.5(b)).

A third class of actuation methods, beyond bio-inspired and classical, are novel engineering approaches that involve ingenious interactions between the individual parts of the microrobot and/or the microrobot and its environment, such as the pivoting stick-slip microrobot described by Pawashe et al. [2009]. It is composed of a NdFeB magnet of size $250 \times 130 \times 10\mu m^3$ and actuated by three pairs of electromagnets. Forward actuation is achieved by imposing a time-varying magnetic torque on the microrobot which pivots it over a surface in a stick-slip way (Fig. 1.6(a)).

Another propulsion method was developed by Vollmers et al. [2008]. The microrobot consists of two nickel masses connected by a gold spring. An applied magnetic field magnetizes the nickel bodies and, thus, creates an attractive force between them. It is reported that an oscillating magnetic field excites the microrobot to resonance and impact induces propulsion, hence the name Wireless Resonant Magnetic Micro Actuator (WRMMA) (Fig. 1.6(b)).

[2]Degree Of Freedom

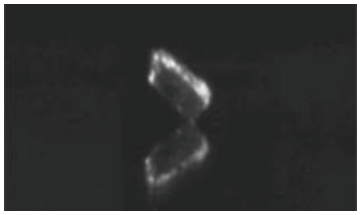

(a) Pivoting stick-slip microrobot introduced in Pawashe et al. [2009].

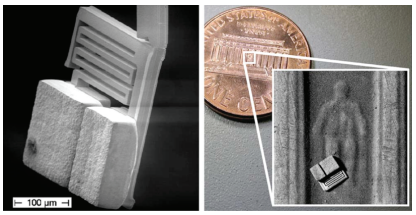

(b) The wireless resonant magnetic microactuator by Vollmers et al. [2008].

Figure 1.6: Untethered Magnetic Microrobots

1.3 Objective and Scope

As detailed in the previous section, there is a growing body of experimental research in the area of untethered magnetic microrobots. Yet, their theoretical understanding is often limited. Consider for example microrobots made from soft-magnetic material such as nickel. When placed in an external magnetic field, the nickel body will become magnetized. But at the same time, its magnetization will interact with the external field. This nonlinear interaction is responsible for the magnetic forces and torques exerted on the body and is well understood as detailed by Judy and Muller [1997] and Abbott et al. [2007a].

Still, during computation of the magnetization, one must distinguish between linear and saturated behavior, and iterative solving of transcendental equations is necessary. This current method allows, to some extent, the analysis of the magnetization. However, it does not allow for a closed form expression, and it is especially unsuitable for fast computation necessary for real-time control, especially if transition from the linear to the saturation region may occur.

In addition to this nonlinear interaction, several microrobots described above consist of multiple soft-magnetic bodies placed close to each other and placed in an applied field. Thus, in addition to the magnetization induced by the applied field, there may also be interaction between the individual parts of the microrobot, with the resulting behavior is not understood and perhaps even counter-intuitive. Consider, for example, the assembled microrobot presented by Yesin et al. [2006]. The torques and forces exerted on its individual parts are well understood. Yet, when assembled, the standard method of analysis, assuming that the body is an ellipsoid [Abbott et al., 2007a], fails as will be shown in Chapter 3. This thesis will provide two contributions here.

First, we will reformulate the standard method for computing the magnetization, and by taking advantage of the resulting structure, propose a method for faster computation. This reformulation uses the Lagrange multiplier technique, and makes it possible to compute the magnetization as a polynomial root solving problem, rather than the iterative approach employed in the standard method. This is particularly interesting for fast com-

putation, e.g. for real-time control systems. Also, the advantage of our method is that it allows for the treatment of the linear and saturated magnetization region with a single continuous formula where the standard results are the limiting cases.

Second, using the proposed method for magnetization, we derive the resulting torque expression, and show that the standard results are obtained as its limiting cases. Then, we investigate superposition of shapes and give phenomenological arguments that, in most of cases, interaction can be neglected. We argue that configurations may exist where one or just few shapes dominate the total torque on assembled structures.

In the case of the WRMMA [Vollmers et al., 2008], the situation is more complex. In addition to the nonlinear interactions between both magnetic bodies and the applied magnetic field, now one has to deal with friction between the bodies and the substrate and eventual impact between the bodies.

Here the two contributions of this thesis are as follows. First, we apply results and methods from non-smooth multibody dynamics to analyze the motion resulting from all these interactions. Our numerical results allow for insight into the motion mechanism and the study of parameter influences, the former being impossible with current experimental techniques. The latter, while possible, being difficult due to coupling effects. Here, the second contribution is a linearized analytical model that allows for the identification of characteristic parameters and non-dimensional quantities that translate into design and actuation guidelines.

In general, this thesis provides the reader with practical knowledge on how a particular magnetic device will behave in magnetic fields and field gradients. A rigorous treatment of the physics involved, e.g., in the magnetization of the material (i.e., micromagnetism), is beyond the scope of this thesis. Rather, from an engineering perspective, we provide methods and results that help build intuition and guide the design of complex untethered soft-magnetic microrobots.

1.4 Outline

The thesis is organized as follows.

In Chapter 2, we review the physical background for this thesis, that is, Maxwell's equations which describe the propagation of electromagnetic waves. We review the models for magnetic dipoles and give a brief introduction to magnetic materials. Then, we present the standard method for calculating the magnetization of a soft-magnetic body in an externally applied field. Next, we propose a method based on Lagrangian analysis that, both, speeds up and simplifies the computation. We conclude the chapter by analyzing our method and demonstrate that it yields the exact same results as the standard method.

Microrobots assembled from planar components are investigated in Chapter 3. First, using our results from the previous chapter, we derive expressions for the magnetic torque and force acting on a sample with known magnetization. Then, we employ these expressions to analytically investigate linear superposition neglecting the interaction between the individual components. We conclude the chapter by applying our findings to analyze the force and torque acting on the assembled microrobot.

Chapter 4 briefly reviews non-smooth multi-body dynamics in the context of microrobotics. Then, as an application example, the presented method is applied to analyze the dynamics of the WRMMA. The numerical results provide insight into its motion mechanism for the first time. Also they justify simplifications in the derivation of an analytical model. This allows us to identify non-dimensional characteristic parameters of the system that can be used for its design and actuation.

Finally, Chapter 5 summarizes the thesis and highlights the contributions.

1.5 References

Abbott, J. J., Ergeneman, O., Kummer, M. P., Hirt, A. M., and Nelson, B. J. (2007a). A continuous model for magnetization torque on axially symmetric bodies. In *Joint MMM/Intermag Conf.*

Abbott, J. J., Nagy, Z., Beyeler, F., and Nelson, B. J. (2007b). Robotics in the small, part I: Microrobotics. *IEEE Robot. Automat. Mag.*, 14(2).

Akiyama, T. and Shono, K. (1993). Controlled stepwise motion in polysilicon microstructures. *J. Microelectromech. Syst.*, 2(3):106 –110.

Batra, R. C., Porfiri, M., and Spinello, D. (2007). Review of modeling electrostatically actuated microelectromechanical systems. *Smart Materials and Structures*, 16(6):R23.

Berg, H. C. (1973). Bacteria Swim by Rotating their Flagellar Filaments. *Nature*, 245:380–382.

Breguet, J.-M., Johansson, S., Driesen, W., and Simu, U. (2006). A review on actuation principals for few cubic millimeter sized mobile micro-robots. In *Proc. of the 10th Int. Conf. on New Actuators (Actuator 2006)*, pages 374–381.

Caprari, G., Estier, T., and Siegwart, R. (2002). Fascination of down scaling alice the sugar cube robot. *Journal of Micromechatronics*, 1:177–189(13).

Chuang, W.-C., Lee, H.-L., Chang, P.-Z., and Hu, Y.-C. (2010). Review on the modeling of electrostatic mems. *Sensors*, 10(6):6149–6171.

Cohn, M. B., Boehringer, K. F., Noworolski, J. M., Singh, A., Keller, C. G., Goldberg, K. Y., and Howe, R. T. (1998). Microassembly technologies for MEMS. In *Society of Photo-Optical Instrumentation Engineers (SPIE) Conference*, volume 3511, pages 2–16.

Dario, P., Valleggi, R., Carrozza, M. C., Montesi, M. C., and Cocco, M. (1992). Microactuators for microrobots: a critical survey. *J. of Micromechanics and Microengineering*, 2(3):141.

Donald, B., Levey, C., McGray, C., Paprotny, I., and Rus, D. (2006). An untethered, electrostatic, globally controllable MEMS micro-robot. *J. Microelectromech. Syst.*, 15(1):1 – 15.

Donald, B., Levey, C., McGray, C., Rus, D., and Sinclair, M. (2003). Power delivery and locomotion of untethered microactuators. *J. Microelectromech. Syst.*, 12(6):947 – 959.

Donald, B., Levey, C., and Paprotny, I. (2008). Planar microassembly by parallel actuation of mems microrobots. *J. Microelectromech. Syst.*, 17(4):789 –808.

Elbuken, C., Khamesee, M., and Yavuz, M. (2009). Design and implementation of a micromanipulation system using a magnetically levitated mems robot. *Mechatronics, IEEE/ASME Transactions on*, 14(4):434 –445.

Flynn, A. M., Brooks, R. A., III, W. M. W., and Barrett, D. S. (1989). Intelligence for miniature robots. *Sensors and Actuators*, 20(1-2):187 – 196.

Fujita, H. (1995). Recent progress of microactuators and micromotors. *Microsystem Technologies*, 1:93–97.

Gauthier, M. and Regnier, S., editors (2010). *Robotic Micro-Assembly*. Wiley-IEEE Press, Haboken, NJ.

Gillies, G. T., Ritter, R. C., Broaddus, W. C., Grady, M. S., Howard III, M. A., and McNeil, R. G. (1994). Magnetic manipulation instrumentation for medical physics research. *Review of Scientific Instruments*, 65(3):533–562.

Honda, T., Arai, K., and Ishiyama, K. (1996). Micro swimming mechanisms propelled by external magnetic fields. *IEEE Trans. on Magnetics*, 32(5):5085 –5087.

Judy, J. W. and Muller, R. S. (1997). Magnetically actuated, addressable microstructures. *J. Microelectromech. Syst.*, 6(3):249–256.

Kummer, M., Abbott, J. J., Kratochvil, B. E., Borer, R., Sengul, A., and Nelson, B. J. (2010). Octomag: An electromagnetic system for 5-DOF wireless micromanipulation. In *Proc. IEEE Int. Conf. Robot. Automat.*

Kummer, M. P., Abbott, J. J., Vollmers, K., and Nelson, B. J. (2007). Measuring the magnetic and hydrodynamic properties of assembled-MEMS microrobots. In *Proc. IEEE Int. Conf. Robot. Automat.*, pages 1122–1127.

Linderman, R. J. and Bright, V. M. (2001). Nanometer precision positioning robots utilizing optimized scratch drive actuators. *Sensors and Actuators A: Physical*, 91(3):292 – 300.

Liu, D. K.-C., Friend, J., and Yeo, L. (2010). A brief review of actuation at the micro-scale using electrostatics, electromagnetics and piezoelectric ultrasonics. *Acoustical Science and Technology*, 31(2):115–123.

Madden, J., Vandesteeg, N., Anquetil, P., Madden, P., Takshi, A., Pytel, R., Lafontaine, S., Wieringa, P., and Hunter, I. (2004). Artificial muscle technology: physical principles and naval prospects. *Oceanic Engineering, IEEE Journal of*, 29(3):706 – 728.

Nelson, B. J., Kaliakatsos, I. K., and Abbott, J. J. (2010). Microrobots for minimally invasive medicine. *Annual Review of Biomedical Engineering*, 12:55–85.

Pawashe, C., Floyd, S., and Sitti, M. (2009). Modeling and Experimental Characterization of an Untethered Magnetic Micro-Robot. *Int. J. Robotics Research*, 28(8):1077–1094.

Purcell, E. M. (1977). Life at low Reynolds number. *American Journal of Physics*, 45(1):3–11.

Vollmers, K., Frutiger, D. R., Kratochvil, B. E., and Nelson, B. J. (2008). Wireless resonant magnetic microactuator for untethered mobile microrobots. *Applied Physics Letters*, 92(14):144103–3.

Yesin, K. B., Vollmers, K., and Nelson, B. J. (2006). Modeling and control of untethered biomicrorobots in a fluidic environment using electromagnetic fields. *Int. J. Robot. Res.*, 25(5-6):527–536.

Zhang, L., Abbott, J. J., Dong, L. X., Kratochvil, B. E., Bell, D. J., and Nelson, B. J. (2009a). Artificial bacterial flagella: Fabrication and magnetic control. *Applied Physics Letters*, 94(6).

Zhang, L., Abbott, J. J., Dong, L. X., Peyer, K. E., Kratochvil, B. E., Zhang, H. X., Bergeles, C., and Nelson, B. J. (2009b). Characterizing the swimming properties of artificial bacterial flagella. *Nano Letters*, 9(10):3663–3667.

Zhang, L., Peyer, K. E., and Nelson, B. J. (2010). Artificial bacterial flagella for micromanipulation. *Lab on a Chip*, 10:2203–2215.

Oh no! Not the magnet!

Bender - bla Futurama

CHAPTER 2

Magnetostatics

After introducing Maxwell's equations to describe electric and magnetic fields, the basic magnetic entity, the magnetic dipole is described. Then, the constitutive relationships for magnetic materials are given, and a criterion is derived to determine whether the magnetization of a soft-magnetic sample is dominated by its shape or its material properties. We review the standard method of computing this magnetization, and then, based on Lagrangian analysis, propose a method that is both simpler and faster than the standard method while still yielding the exact same results.

2.1 Introduction

Observations on magnetism[1] can be traced back to the Greek philosopher Thales in the 6th century B.C. Yet, it was not until the 17th century A.D. that the english physicist William Gilbert has published the first systematic experiments on magnetism. In Gilbert [1600], he concludes that the earth is magnetic and that this is the reason that a compass needle points towards the north.

Around two hundred years later, in 1820, the Danish physicist Oersted discovered the connection between electrical current and magnetic field by observing that a compass needle is also deflected by a current carrying wire. This observation inspired French physicist Ampère to develop and present a description of the way in which an electrical current produces a magnetic field. He also demonstrated that two current carrying wires can repel or attract each other depending on the direction of the current in them. His work is considered to be the foundation of modern electromagnetism.

With the advent of quantum mechanics in the early 20th century, magnetic effects are explained from the atomic structure of material. Protons and neutrons located in the positively charged nucleus and are surrounded by

[1] this introduction follows loosely the Wikipedia entry on magnetism

(a) W. Gilbert (1544–1603)

(b) H.C. Oersted (1777–1851)

(c) A.M. Ampère (1775–1835)

electrons carrying negative charges. As these electrons move, they produce a magnetic field in space (see also Maxwell's equation (2.2)). The state of the electrons is described by four quantum numbers, the last one being the magnetic spin, which can only have the values $1/2$ or $-1/2$, and may be loosely interpreted as the direction of the magnetic field they produce.

Due to the Pauli exclusion principle, two electrons cannot have the same four quantum numbers. Thus, there is only room for two electrons in each spatial orbital, and they must have opposing magnetic spin. If this is the case, the electrons are said to be paired, their magnetic fields cancel, and no net magnetic field exists. The material is said to be diamagnetic. However, in materials with unpaired electrons, a net magnetic field is produced and an applied external magnetic field will generate reaction in the material. These materials are called para- or ferromagnetic. They will be further examined in Section 2.4.2.

2.2 Maxwell's Equations

In Maxwell [1865], the Scottish mathematician and physicist James C. Maxwell published a synthesis of previously unrelated observations, experiments and equations of electricity, magnetism and even optics in a consistent theory. He demonstrates that electric and magnetic fields travel through space in the form of waves at the constant speed of light. In differential form, his equations, *Maxwell's equations*, are given by

$$\text{Faraday's Law of Induction} \qquad \nabla \times \mathbf{E} = -\frac{\partial \mathbf{B}}{\partial t} \tag{2.1}$$

$$\text{Ampère's Law} \qquad \nabla \times \mathbf{H} = \mathbf{J} + \frac{\partial \mathbf{D}}{\partial t} \tag{2.2}$$

$$\text{Gauss's Law} \qquad \nabla \cdot \mathbf{D} = \rho \tag{2.3}$$

$$\text{Gauss's Law for Magnetics} \qquad \nabla \cdot \mathbf{B} = 0 \tag{2.4}$$

where $\mathbf{H}(\mathbf{r}, t)$ (in A/m) and $\mathbf{E}(\mathbf{r}, t)$ (in V/m) are the magnetic and electric field respectively, $\mathbf{D}(\mathbf{r}, t)$ (in C/m^2) and $\mathbf{B}(\mathbf{r}, t)$ (in T) are the electric[2] and magnetic flux density, and $\rho(\mathbf{r}, t)$ (in C/m^3) and $\mathbf{J}(\mathbf{r}, t)$ (in A/m^2) are the free

[2] $\mathbf{D}$ is also referred to as the *electric displacement*

electric charge and free current density respectively, $\mathbf{r} \in \mathbb{R}^3$ is the position vector and t is time. The dell operator in cartesian coordinates is defined as $\nabla = \left[\frac{\partial}{\partial x}, \frac{\partial}{\partial y}, \frac{\partial}{\partial z}\right]^{\mathrm{T}}$.

The interpretation of (2.1)–(2.4) is as follows:

(2.1) A time-varying magnetic field is the origin of a curl of the electric field

(2.2) A current density and a time-varying electric flux density cause a curl of the magnetic field

(2.3) A charge density is the source of the electric flux density

(2.4) The magnetic induction is source-free, i.e., magnetic monopoles don't exist.

In this thesis, we consider the special case of magnetostatics, i.e., no electric charges ($\rho = 0$), no electric fields ($\mathbf{E} = 0$) and static (or low frequency) fields ($\frac{\mathrm{d}}{\mathrm{d}t}(\,\cdot\,) = 0$). Then, Maxwell's equations reduce to

$$\nabla \times \mathbf{H} = \mathbf{J}, \tag{2.5}$$

$$\nabla \cdot \mathbf{B} = 0, \tag{2.6}$$

and $\mathbf{J} = \mathbf{0}$ if there are no currents in the region of interest. The equivalent integral form is

$$\oint_{\partial S} \mathbf{H}\,\mathrm{d}\mathbf{l} = \oint_{S} \mathbf{J}\,\mathrm{d}\mathbf{S}, \text{ and} \tag{2.7}$$

$$\oint_{S} \mathbf{B}\,\mathrm{d}\mathbf{S} = 0 \tag{2.8}$$

where $\mathrm{d}\mathbf{S}$ is the surface normal vector, and ∂S is the boundary of a closed surface S. (2.8) states that the net flux of $\mathbf{B}$ through S is zero. In other words the *number of field lines entering* any given volume in space is equal to the *number of field lines leaving* that volume or, equivalently, no magnetic monopoles exist.

Note, however, that this is not a consequence of Maxwell's equation, but rather an experimental fact, that no magnetic monopoles have been observed. It is straightforward to include magnetic monopoles in Maxwell's equation and, thus making the equations more symmetrical. The basic magnetic unit, or entity, is the magnetic dipole, and its modeling is the subject of section 2.3.

The constitutive relationship between $\mathbf{B}$ and $\mathbf{H}$, i.e., $\mathbf{B}(\mathbf{H})$, of a material allows for the simultaneous solution of the system defined by (2.5) and (2.6). In addition, it is one way of classifying magnetic materials, as will be shown in Section 2.4.

2.2.1 Continuity and Boundary Conditions

Equations (2.5) and (2.6) together with the constitutive relation are valid inside one material or one computational domain. If the magnetic field transitions from one material to another, e.g., from air into nickel, the equations

for both domains need to be fulfilled simultaneously at their boundary. They can be derived from integral forms by choosing the integration domains such that the boundary is enclosed.

The result, in the absence of surface currents (which is true for all our applications), is found to be

$$H_{1,t} = H_{2,t} \tag{2.9}$$
$$B_{1,n} = B_{2,n} \tag{2.10}$$

where $H_{i,t}$ and $B_{i,n}$ designate the tangential and normal component of the magnetic field and flux density in the domain i respectively. In brief, these conditions require conservation of the tangential component of $\mathbf{H}$ and the normal component of $\mathbf{B}$. At the outer boundaries of the computational domain, these conditions reduce to $H_t = 0$ and $B_n = 0$.

2.3 The Magnetic Dipole

As mentioned above, no magnetic monopoles have been observed experimentally, and this fact is expressed by Maxwell's equation (2.4). The magnetic dipole is the most elementary unit in magnetism and can be modeled using Ampère's Law as a current loop, i.e., an electric charge that is moving on a loop thereby creating a magnetic field. Or, in analogy to the electric dipole, by introducing positive and negative magnetic charges always occurring pairwise.

We now give the descriptions for the field of a magnetic dipole $\mathbf{\Gamma}$ (in Am^2) at a point $\mathbf{P}$ in space relative to the dipole, and discuss their validity. The strength of the dipole, $||\mathbf{\Gamma}||$, is the magnetic moment.

2.3.1 Current Loop

$$||\mathbf{H}(\mathbf{\Gamma}, \mathbf{P})|| = \frac{||\mathbf{\Gamma}||}{c2\pi \left(r^2 + ||\mathbf{P}||^2\right)^{3/2}} \tag{2.11}$$

In this model, the magnetic moment $||\mathbf{\Gamma}|| = \pi i r^2$ is created by a current loop of radius r that carries the current i. The dipole points in the direction defined by the right hand rule and $c = 1$ for the on-axis magnetic field. To estimate the field magnitude radially from the center of the current loop, using $c = 2$ in (2.11) will yield the correct result [Kummer et al., 2007].

The current loop model is valid along the dipole axis and along an axis extending radially from the dipole center.

2.3.2 Magnetic Charge

In order to predict the magnetic field at any desired location in space, the charge-dipole model is more suitable [Furlani, 2001]. This dipole is created by one positive and one negative magnetic (surface) charge $\pm Q_m$ (in Am)

separated by a distance $\mathbf{d}$. The dipole moment is then $\mathbf{\Gamma} = Q_m\mathbf{d}$, and its field given by

$$\mathbf{H}(\mathbf{\Gamma}, \mathbf{P}) = \frac{Q_m}{4\pi}\left(-\frac{\mathbf{P}_1}{||\mathbf{P}_1||^3} + \frac{\mathbf{P}_2}{||\mathbf{P}_2||^3}\right) \tag{2.12}$$

with $\mathbf{P}_1 = (1/2)\mathbf{d} + \mathbf{P}$ and $\mathbf{P}_2 = -(1/2)\mathbf{d} + \mathbf{P}$. For $||\mathbf{d}|| \ll ||\mathbf{P}||$, this expression reduces to

$$\mathbf{H}(\mathbf{\Gamma}, \mathbf{P}) = \frac{1}{4\pi||\mathbf{P}||^3}\left(\frac{3(\mathbf{\Gamma}\cdot\mathbf{P})\mathbf{P}}{||\mathbf{P}||^2} - \mathbf{\Gamma}\right) \tag{2.13}$$

and is called the point-dipole model as it is equivalent to the case of $||\mathbf{d}|| \to 0$.

2.4 Magnetic Materials

In a magnetic material (as well as in vacuum) $\mathbf{B}$ and $\mathbf{H}$ are related by the constitutive law

$$\mathbf{B} = \boldsymbol{\mu}(\mathbf{H})\mathbf{H} \tag{2.14}$$

where $\boldsymbol{\mu}(\mathbf{H})$ is the magnetic permeability tensor. It is generally anisotropic and nonlinear. In this thesis, we consider isotropic materials and we now investigate two separate regions of the the permeability, linear material behavior, and saturated behavior.

2.4.1 Linear Material Behavior

In linear isotropic magnetic materials $\boldsymbol{\mu}(\mathbf{H})$ reduces to a scalar

$$\begin{aligned} \mathbf{B} &= \mu \cdot \mathbf{H} && (2.15)\\ &= \mu_0\mu_r \cdot \mathbf{H} && (2.16) \end{aligned}$$

where $\mu_0 = 4\pi \times 10^{-7}\mathrm{Tm/A}$ is the permeability of free space (scalar) and $\mu_r > 0$ (dimensionless) is the relative permeability.

The latter can be used to classify magnetic materials as diamagnetic ($\mu_r < 1$), paramagnetic ($\mu_r = 1...10$) and ferromagnetic ($\mu_r \gg 10$). It is a measure of how well the material concentrates the flux lines, e.g., the higher μ_r the more flux lines go through it for the same magnetic field $\mathbf{H}$. For $\mu_r > 1$ this flux density increases, while for $\mu_r < 1$ it decreases. Phenomenologically, this means that diamagnetic materials (e.g. water) are repelled by a magnet, while para- and ferromagnetic materials (e.g. iron) are attracted towards it.

Typically, an effect is only seen for ferromagnetic materials (large μ_r); this is why they are commonly referred to as "magnetic materials". Examples are iron, nickel, cobalt and their alloys. A special case is vacuum or air with $\mu_r = 1$ in which no formal distinction is usually made between the magnetic flux density $\mathbf{B}$ and the magnetic field $\mathbf{H}$, and the terms are used interchangeably.

2.4.2 Non-Linear Effect: Saturation

The linear relationship (2.16) between $\mathbf{B}$ and $\mathbf{H}$ is a simplification and only holds for sufficiently small magnetic fields. In fact, the permeability, rather than the ratio of $\mathbf{B}$ and $\mathbf{H}$, has to be interpreted as a differential quantity

$$\mu = \frac{\partial \mathbf{B}}{\partial \mathbf{H}}. \tag{2.17}$$

To understand what happens in magnetic materials, we need to look further into their atomic structure. As has been discussed in section 2.1, para-and ferromagnetic materials have unpaired electrons and have a comparatively large reaction to externally applied fields.

Paramagnetic materials have no net field as the magnetic dipoles are oriented randomly. When an external field is applied, these dipoles tend to align in parallel with the field. When the external field is turned off, a random orientation is obtained, again without net field.

In ferromagnetic materials, the same effect occurs. Yet, in addition, the dipoles tend to spontaneously align themselves even without an external field. Two nearby dipoles will tend to align in the same direction to reduce their exchange energy (quantum-mechanical effect), while at longer distances (many thousands of atoms) the dipoles are anti-aligned (classical dipole behavior). Because of the latter effect, generally the dipoles in the whole material are not aligned, even at equilibrium. Rather, they are organized in domains, the so-called Weiss domains, and there is little or no net field produced by such a material.

When a ferromagnetic material is first placed in a magnetic field, the flux density will increase proportionally to the field strength in the material following (2.16). In the material, the domain walls move. In addition, the domains reorient parallel to the magnetic field and a net field is generated. With increasing field strength, more domains align with the field, and the permeability decreases until all domains are oriented. The material is said to be saturated, and a further increase of the field strength has no effect on the flux. In other words, the permeability has decreased from its initial value μ_r to 1.

The phenomenon that the ferromagnetic material undergoes when placed in an external magnetic field is called *magnetization*. Mathematically, it can be described as a vector field $\mathbf{M}(\mathbf{r}, t)$ (in A/m), and the constitutive relationship $\mathbf{B}(\mathbf{H})$ is written as

$$\mathbf{B} = \mu_0 \left(\mathbf{H} + \mathbf{M}\right), \tag{2.18}$$

$$= \mu_0 \mathbf{H} + \mu_0 \mathbf{M}. \tag{2.19}$$

The behavior of the ferromagnetic materials when the external field is turned off or an opposed external field is applied, i.e., their demagnetizing behavior, leads to their further classification:

Hard Magnetic materials need high external fields to reduce the magnetization and are thus difficult to demagnetize. This fact is also described by designating hard magnetic materials as having a high *coercivity*. The magnetization of a hard magnetic material, or permanent magnet, is independent of $\mathbf{H}$ and (2.19) can be used to define two characteristic terms. For a vanishing magnetic field ($\mathbf{H} = 0$), we find the remanent flux density $\mathbf{B_r} = \mu_0\mathbf{M}$. And for a vanishing flux density ($\mathbf{B} = 0$), the coercive field is defined as $\mathbf{H_c} = -\mathbf{M}$.

Soft Magnetic materials, on the other hand, show a low coercivity and are consequently easier to demagnetize. For linear behavior and negligible coercivity, their magnetization depends on $\mathbf{H}$ as

$$\mathbf{M} = \chi\mathbf{H}, \tag{2.20}$$

where χ is the susceptibility. Inserting this relationship in (2.19), we have

$$\begin{aligned}\mathbf{B} &= \mu_0\mathbf{H} + \mu_0\chi\mathbf{H} && (2.21)\\ &= \mu_0(1+\chi)\mathbf{H} && (2.22)\\ &= \mu_0\mu_r\mathbf{H}. && (2.23)\end{aligned}$$

Thus, the susceptibility is related to the permeability as $\chi = \mu_r - 1$, and can also be used to characterize materials as diamagnetic ($\chi < 0$), non-magnetic ($\chi = 0$) or para- and ferromagnetic ($\chi > 0$).

The magnetization behavior of ferromagnetic materials is conveniently represented in $\mathbf{B}(\mathbf{H})$ or $\mathbf{M}(\mathbf{H})$ diagrams. See Figure 2.1 for a typical $\mathbf{B}(\mathbf{H})$ diagram, along with its characteristic points. Note that both magnetic field and flux density are considered to be internal to the material.

2.5 Shape Effect and Magnetization

We have seen in Section 2.4.2 that a soft magnetic material, when placed in a magnetic field, will be magnetized. For relatively low fields, the magnetization grows with the internal field following (2.20). For larger fields, the material saturates and the magnetization reaches its maximal value, the saturation magnetization m_s.

To relate the magnetization of a sample to an applied or external field $\mathbf{H}$, the anisotropy or demagnetizing effects that oppose the magnetization process need to be considered. This thesis only considers shape anisotropy, i.e., the fact that different directions of a sample magnetize differently. Another form of anisotropy would be crystalline anisotropy where the crystal structure of the sample has preferred magnetic directions.

To determine the magnetization of a sample analytically, we must make the assumption that the sample is uniformly magnetized, thus $\mathbf{M}$, $\mathbf{B}$ and $\mathbf{H}$ are uniform throughout the sample. This assumption only holds true for

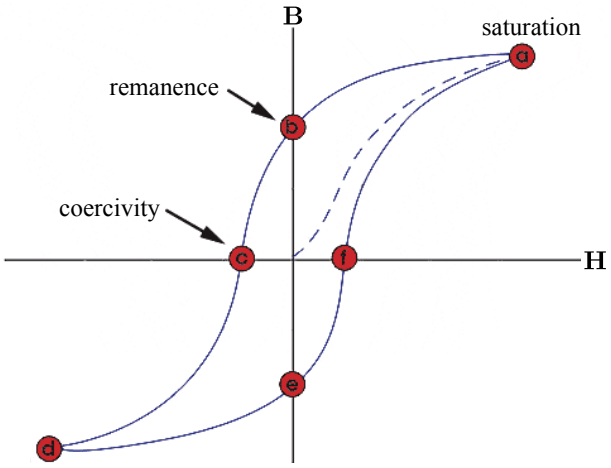

Figure 2.1: A typical magnetization curve showing the constitutive relationship between **B** and **H**, and some characteristic points along the graph. Points (a) and (d) represent saturation state, (b) and (e) the remanence, and (c) and (f) the coercivity of the sample. (source: http://www.ndt-ed.org)

ellipsoids. Then, the task of determining the magnetization is to find its magnitude and direction.

2.5.1 Low Applied Fields

For the low applied field region, we can distinguish two cases—no hysteresis/coercivity, or a small coercivity. For the former, the magnetic field $\mathbf{H_i}$ inside the material can be written as

$$\mathbf{H_i} = \mathbf{H} + \mathbf{H_d}, \tag{2.24}$$

where $\mathbf{H_d}$ is the demagnetizing field of the sample. It is related to the magnetization through the diagonal demagnetization tensor $\mathbf{N}$ as

$$\mathbf{H_d} = -\mathbf{N}\mathbf{M}, \tag{2.25}$$

where the entries of $\mathbf{N}$ are the strictly positive, non-dimensional demagnetization factors. For a cartesian coordinate system, we have

$$\mathbf{N} = \operatorname{diag}\left(n_x, n_y, n_z\right), \tag{2.26}$$

and $\operatorname{tr}(\mathbf{N}) = n_x + n_y + n_z = 1$. Section 2.8 discusses the computation of $\mathbf{N}$.

The demagnetizing factors characterize how well a direction of the sample can be magnetized. The smaller the value, the easier this is. Consequently, the direction of the sample with the smallest demagnetizing factor is the magnetic easy axis of the sample, and the direction with the largest demagnetizing factor is the magnetic hard axis. In this work, unless otherwise specified,we will always rotate the body coordinate frame such that

$n_x \leq n_y \leq n_z$, i.e., the x-axis will be the easy axis of the sample.

Now, we can use (2.20) and (2.25) in (2.24) to find

$$\chi \mathbf{M} = \mathbf{H} - \mathbf{N}\mathbf{M}. \tag{2.27}$$

For this, note that (2.20) is expressed in the internal field. Solving (2.27) for $\mathbf{M}$ yields

$$\mathbf{M} = \mathcal{X}_a \mathbf{H}, \tag{2.28}$$

where $\mathcal{X}_a$ is the apparent (or external) susceptibility tensor given by

$$\mathcal{X}_a = (\mathbf{I} + \chi \mathbf{N})^{-1} \chi \tag{2.29}$$

with $\mathbf{I}$ denoting the unity tensor. Note, that (2.28) considers only the case for negligible coercivity, i.e., the internal field is perfectly reduced to zero by the demagnetizing fields. However, if the material has a certain coercivity $\mathbf{H_c}$, Judy and Muller [1997] provide the expression for the magnetization as

$$\mathbf{M} = \mathbf{N}^{-1}(\mathbf{H} + \mathbf{H_c}) \tag{2.30}$$

$$= \mathbf{N}^{-1}\mathbf{H} + \mathbf{N}^{-1}\mathbf{H_c} \tag{2.31}$$

for the case of shape dominance see Section 2.5.2.

In summary, for sufficiently low applied fields, if coercivity can be neglected, the magnetization is calculated as (2.28). Small coercivities can be taken into account using (2.30).

2.5.2 Shape or Material Dominance?

Consider one component χ_a of the apparent susceptibility (2.27) and observe its limit for $\chi \to \infty$ as

$$\chi_a = \frac{\chi}{1 + n_i \chi} \xrightarrow{\chi \to \infty} \frac{1}{n_i} =: \chi_{a,\max}. \qquad i = x, y, z \tag{2.32}$$

We see that for high susceptibilities, typical for ferromagnetic materials, the apparent susceptibility cannot exceed a maximal value $\chi_{a,\max}$, which is determined by its shape. Hence, for a known material χ and shape with $n_{\min} = \min(n_x, n_y, n_z)$, the ratio

$$z_\chi = \frac{\chi_a}{\chi_{a,\max}} = \frac{n_{\min}\chi}{1 + n_{\min}\chi} \in (0, 1) \tag{2.33}$$

describes the dominating effect of the sample as

$$z_\chi \to \begin{cases} 0, & \text{material dominance} \\ 1, & \text{shape dominance} \end{cases}. \tag{2.34}$$

Figure 2.2 shows z_χ as a function of $n_{\min}$ for different susceptibilities.

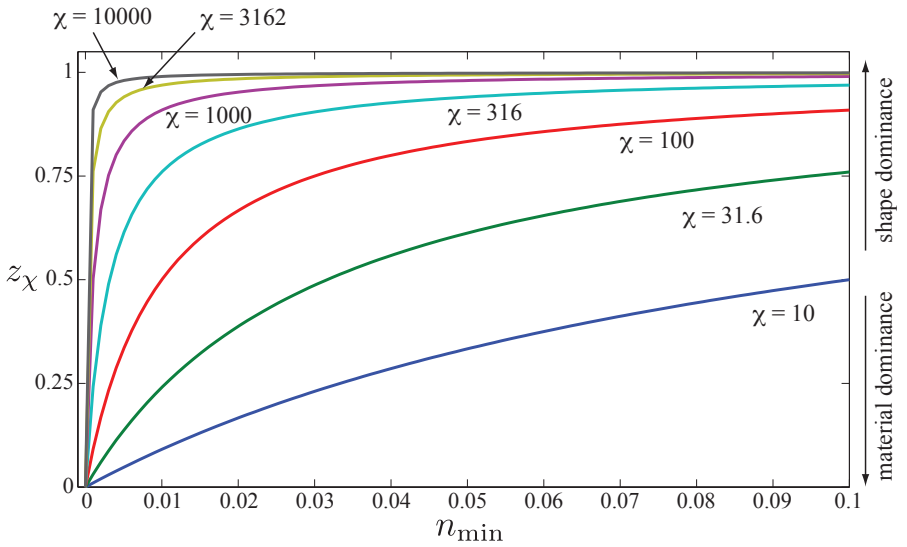

Figure 2.2: The ratio $z\chi$ describes if the magnetic behavior of a sample is dominated by its material properties ($z\chi \to 0$) or by its shape ($z\chi \to 1$)

Another definition of an effective or apparent quantity is the effective permeability μ_{eff} relating the internal flux $\mathbf{B_i}$ to the applied field $\mathbf{H}$ as

$$\mathbf{B_i} = \mu_0 \mu_{\text{eff}} \mathbf{H}. \tag{2.35}$$

A derivation is given by Brugger and Paul [2010], resulting in

$$\mu_{\text{eff}} = \frac{\mu_r}{1 + n_{\min}(\mu_r - 1)} \quad \xrightarrow{\mu_r \to \infty} \quad \frac{1}{n_{\min}} =: \mu_{\text{eff,max}}. \tag{2.36}$$

As in the case of the apparent susceptibility, the limit for high permeabilities is $1/n_{\min}$ which necessary for consistency, since $\mu_r = \chi + 1$. As z_χ, the ratio z_μ allows also to determine if the behavior of a sample is shape or geometry dominated:

$$z_\mu := \frac{\mu_{\text{eff}}}{\mu_{\text{eff,max}}} = \frac{n_{\min}\mu_r}{1 + n_{\min}(\mu_r - 1)} \to \begin{cases} 0, & \text{material dominance} \\ 1, & \text{shape dominance} \end{cases} \tag{2.37}$$

Now, for the thin structures considered in this work, we usually have $n_z \approx 0.9$, thus $n_x + n_y = 1 - n_z \approx 0.1$, and thus $n_{\min} < 0.1$. With typical values for ferromagnetic materials of $\chi \gg 100$, we see that $z_\mu \approx 1$ for all the cases considered in this work. Consequently, (2.28) simplifies to

$$\mathbf{M} = \mathbf{N}^{-1}\mathbf{H}, \tag{2.38}$$

and comparing this to (2.30) shows that coercivity effects are accounted for by a simple summation, and, thus, magnetization in the low field region is always described as

$$\mathbf{M} = \mathbf{N}^{-1}(\mathbf{H} + \mathbf{H_c}) \tag{2.39}$$

with $\mathbf{H_c} \neq \mathbf{0}$ if coercivity is considered, and $\mathbf{H_c} = \mathbf{0}$ if it can be neglected.

2.5.3 Saturating Fields

In the saturation region the magnitude of $\mathbf{M}$ remains constant at its saturated magnetization value m_s, $||\mathbf{M}|| = m_s$, and $\mathbf{M}$ rotates to minimize the magnetic energy density (in $\mathrm{J/m^3}$)

$$e_1 = \frac{1}{2}\mu_0 \mathbf{M}^{\mathrm{T}} \mathbf{N} \mathbf{M} - \mu_0 \mathbf{H}^{\mathrm{T}} \mathbf{M}. \tag{2.40}$$

The first term in (2.40) is the demagnetizing energy due to shape anisotropy, which tends to align $\mathbf{M}$ with the magnetic easy axis of the piece. The second term is minimized when $\mathbf{M}$ is aligned with $\mathbf{H}$.

2.5.4 Summary and Limitations of the Current Method

In summary, the computation of the magnetization is performed by computing $\mathbf{M}$ according to (2.39) and then checking if $||\mathbf{M}|| \leq m_s$. If so, the result can be used, otherwise the minimization of (2.40) must be performed. Following the work by Abbott et al. [2007], it will be shown in Section 2.6 for the simplified problem of axially symmetric bodies, that this minimization requires an iterative solution of a transcendental equation and a good initial value.

This approach is not practical for real-time computation as it is an unstructured minimization problem. While the linear solution can be found with minimal computation, the minimization step may significantly increase computation. In Section 2.9, we first show that in our case of shape-dominant pieces, the problem can be formulated as a single minimization step. This allows us to exploit its properties and reformulate the problem as an equivalent polynomial root solving problem, yielding faster overall computation times.

Remark 2.1. *If it is known in advance that the magnetization stays within the linear region, direct computation according to* (2.39) *is of course the fastest method. We are interested in situations where this cannot be assumed and transitions from the linear to the saturation region are possible.*

2.6 Continuous Analytical Model of the Magnetization of on an Ellipsoid

Abbott et al. [2007] presented a magnetization model for ellipsoids that continuously combined the linear and saturation regions. We briefly review it here, before proposing a numerical method that does not require explicit case distinction.

For a soft-magnetic body with axial symmetry (e.g. prolate and oblate ellipsoids), the radial demagnetizing factors are equal, n_r, and the apparent susceptibility tensor is given by

$$\mathcal{X}_a = \mathbf{N}^{-1} = \mathrm{diag}\left(\frac{1}{n_a}, \frac{1}{n_r}, \frac{1}{n_r}\right), \tag{2.41}$$

assuming shape dominance, and denoting the axial demagnetizing factor by n_a. Because of axial symmetry, $\mathbf{H}$, $\mathbf{M}$ and the axis of symmetry are coplanar, and the problem is essentially a 2-D problem. Assuming that $\mathbf{H}$ is applied at an angle θ to this axis of symmetry, i.e., $\mathbf{H} = h\,[\cos\theta, \sin\theta]^{\mathrm{T}}$, and neglecting coercivity, the magnetization in the linear region is found from

$$\mathbf{M} = \mathbf{N}^{-1}\mathbf{H} = h\left[\frac{\cos\theta}{n_a}, \frac{\sin\theta}{n_r}\right]^{\mathrm{T}}, \tag{2.42}$$

and the direction of the magnetization, i.e., the angle ϕ, is given by

$$\phi = \tan^{-1}\left(\frac{n_a}{n_r}\tan\theta\right). \tag{2.43}$$

If the computation of $||\mathbf{M}||$ according to (2.42) yields $||\mathbf{M}|| \leq m_s$, then $\mathbf{M}$ and ϕ are accurate. Yet, if it yields $||\mathbf{M}|| > m_s$, this means that the material is saturated, and energy minimization has to be performed. Setting $||\mathbf{M}|| = m_s$, the magnetic energy density as a function of ϕ is given by

$$e = \frac{1}{2}\mu_0(n_r - n_a)m_s^2\sin^2\phi - \mu_0 m_s||\mathbf{H}||\cos(\theta - \phi). \tag{2.44}$$

To minimize it, $\mathbf{M}$ will rotate such that ϕ satisfies the transcendental equation

$$(n_r - n_a)m_s\sin(2\phi) = 2||\mathbf{H}||\sin(\theta - \phi). \tag{2.45}$$

Furthermore Abbott et al. [2007] demonstrate that the model is continuous across the modeling boundaries, and that the magnetic field that just saturates the material can be derived as

$$||\mathbf{H}||_{\mathrm{sat}} = \frac{m_s n_a n_r}{\sqrt{n_a^2\sin^2\theta + n_r^2\cos^2\theta}}, \tag{2.46}$$

and depends on the applied field angle.

To summarize, this procedure allows for a continuous transition of the magnetization model from the linear to the saturated region. This is particularly important because it allows the model to be inverted so that for a given desired torque and force (which are a function of the magnetization, as will be shown later) the required applied magnetic field can be calculated.

On the other hand, as mentioned in Section 2.5.4, the model requires switching between two cases, and in addition, (2.45) needs to be solved iteratively with a good initial value for ϕ. Also, the extension to the 3D case increases the complexity of the computation. In Section (2.9), we propose a method that eliminates the necessity for these, and, at the same time, decreases the computation speed, a particularly desirable feature in model-based control schemes.

2.7 Analytical Function for the Magnetization Curve for Numerical Simulations

Describing the magnetization as a linear and a constant, saturated region is a necessary simplification for the analytical treatment of magnetization

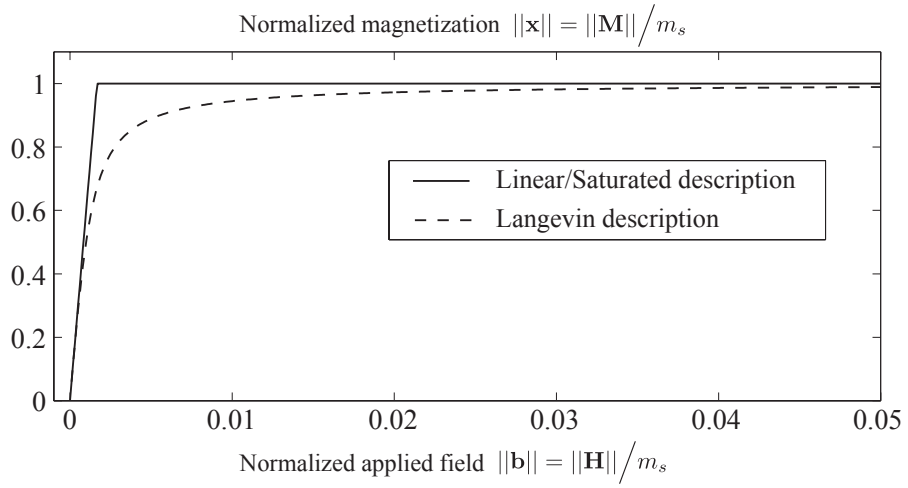

Figure 2.3: Comparison of the *linear/saturated* magnetization curve to the one using a Langevin function. The latter one is used in finite element calculations. Overall the correspondence is quite good, the largest discrepancy being oviously around the transition from the linear to the saturated region.

problems. For numerical computations using the finite element method, we can, for negligible hysteresis, describe the magnetization curve by a Langevin function as

$$||\mathbf{M}|| = m_s \left(\coth(\alpha||\mathbf{H}||) - \frac{1}{\alpha||\mathbf{H}||} \right) \tag{2.47}$$

where α is parameter fit to experimental data. The slope at the origin is the susceptibility χ of the material and is given by

$$\chi = \lim_{||\mathbf{H}||\to 0} ||\mathbf{M}|| = \frac{1}{3} m_s \alpha ||\mathbf{H}||. \tag{2.48}$$

Unless otherwise specified, the reference calculations will use $m_s = 5 \times 10^5 \mathrm{A/m}$ and $\chi = 10000$ (thus $\alpha = 3\chi/m_s = 0.04\mathrm{m/A}$) to ensure shape dominance. With **M**, we can build the **B**-**H** relationship typically required for finite element software using (2.19).

Note that, in fact, a magnetization curve that has a constant magnetization m_s over a large range of field values cannot be used in finite element software because of the zero slope. Rather, as for example in the Langevin approximation, the magnetization has to approach m_s asymptotically. The two different curves are shown in Fig. 2.3. We can clearly observe this discrepancy, which is a source of error when comparing finite element and analytical results, especially around the transition from linear to saturated region.

2.8 Demagnetizing Factors of Non-Ellipsoidal Shapes

The demagnetizing factors characterize how well a direction of the sample can be magnetized. They depend only on the aspect ratio of the shape and

can be calculated exactly for ellipsoids. Tabulated results for various aspect ratios are given by Osborn [1945].

When dealing with non-ellipsoidal shapes, say a cuboid, the typical assumption that is made is that an ellipsoid with the same aspect ratios, the so-called equivalent ellipsoid, will lead to the same demagnetizing effect. And hence, the tabulated values for such equivalent ellipsoids are widely used for various shapes.

However, as has been shown recently by Beleggia et al. [2006], this assumption may lead to significant errors and incorrect results. Therefore, the authors derive the exact mapping between the aspect ratios of shapes that can be described with two aspect ratios (plates, discs, cylinders, etc) and their magnetically equivalent ellipsoid. Note, however, that the assumption of uniform magnetization of the sample still holds.

Unless otherwise specified, we will employ the mappings proposed by Beleggia et al. [2006] to calculate demagnetizing factors.

2.9 Proposed Method to Calculate the Magnetization

This section is the first contribution of this dissertation. We begin by analyzing the structure of the minimization problem. For this, we recall that in the saturation region, the magnetization is found by minimizing the energy (2.40)

$$e = \frac{1}{2}\mu_0 \mathbf{M}^{\mathrm{T}} \mathbf{N} \mathbf{M} - \mu_0 \mathbf{H}^{\mathrm{T}} \mathbf{M} \tag{2.49}$$

and requiring that $||\mathbf{M}|| = m_s$. Thus, it is a constrained minimization problem, or, more specifically a quadratic program with a nonlinear constraint. Now, we observe that the unconstrained minimum of e_2, where

$$e_2 = \frac{1}{2}\mu_0 \mathbf{M}^{\mathrm{T}} \mathbf{N} \mathbf{M} - \mu_0 (\mathbf{H} + \mathbf{H_c})^{\mathrm{T}} \mathbf{M} \tag{2.50}$$

is $\mathbf{M} = \mathbf{N}^{-1}(\mathbf{H} + \mathbf{H_c})$, which is the same as the result (2.39) for the linear region. Thus, we can conclude that in both the linear and the saturated region, the magnetization can be found by minimizing an energy expression. It follows that both cases can be represented in a single minimization problem by changing the constraint from an equality to an inequality as

$$\min_{\mathbf{M} \in \mathbb{R}^3} \frac{1}{2}\mu_0 \mathbf{M}^{\mathrm{T}} \mathbf{N} \mathbf{M} - \mu_0 (\mathbf{H} + \mathbf{H_c})^{\mathrm{T}} \mathbf{M}, \tag{2.51}$$

$$\text{subject to } \mathbf{M}^{\mathrm{T}} \mathbf{M} - m_s^2 \leq 0 \tag{2.52}$$

which is a convex minimization problem since $\det(\mathbf{N}) > 0$, or more exactly a convex quadratically constrained quadratic problem [Boyd and Vandenberghe, 2004; Bryson and Ho, 1975]. It can be solved using a nonlinear minimization tool such as the MATLAB function `fmincon` and will converge to a global minimum.

In a real-time control system, the minimization has to be computed within a single control loop. Although a global minimization algorithm will converge, we can speed up the computation by analyzing the problem more closely. First, we non-dimensionalize the problem by dividing by μ_0 and defining $\mathbf{x} := \mathbf{M}/m_s$ as

$$\min_{\mathbf{x}\in\mathbb{R}^3} \frac{1}{2}\mathbf{x}^{\mathrm{T}}\mathbf{N}\mathbf{x} - \mathbf{b}^{\mathrm{T}}\mathbf{x}, \tag{2.53}$$

$$\text{subject to } \mathbf{x}^{\mathrm{T}}\mathbf{x} - 1 \leq 0 \tag{2.54}$$

with $\mathbf{b} := (\mathbf{H} + \mathbf{H_c})/m_s$, which for the relatively low coercivities considered here will be dominated by $\mathbf{H}$ for large fields ($\mathbf{b} \approx \mathbf{H}/m_s$) and, thus, in the saturation region. This means that the energy term is not altered for the saturation region while still yielding the correct result for the linear region.

Next, we introduce the Lagrangian of the problem by including the constraint in the energy term as

$$L(\mathbf{x}, \lambda) = \frac{1}{2}\mathbf{x}^{\mathrm{T}}\mathbf{N}\mathbf{x} - \mathbf{b}^{\mathrm{T}}\mathbf{x} + \frac{1}{2}\lambda(\mathbf{x}^{\mathrm{T}}\mathbf{x} - 1), \tag{2.55}$$

where λ is called the Lagrange multiplier, and the factor $1/2$ is introduced for convenience later. Since we consider a convex problem, the necessary and sufficient conditions for the minimum are

$$\frac{\partial L}{\partial \mathbf{x}} = \mathbf{N}\mathbf{x} - \mathbf{b} + \lambda\mathbf{x} = \mathbf{0} \tag{2.56}$$

and

$$\frac{\partial L}{\partial \lambda} = \frac{1}{2}\left(\mathbf{x}^{\mathrm{T}}\mathbf{x} - 1\right) \leq 0 \tag{2.57}$$

with

$$\lambda \begin{cases} \geq 0, & \mathbf{x}^{\mathrm{T}}\mathbf{x} - 1 = 0, \\ = 0, & \mathbf{x}^{\mathrm{T}}\mathbf{x} - 1 < 0. \end{cases} \tag{2.58}$$

Evaluating (2.56), we find the solution to the minimization problem to be

$$\mathbf{x} = (\mathbf{N} + \lambda\mathbf{I})^{-1}\,\mathbf{b}. \tag{2.59}$$

Inserting (2.59) in (2.57) for $\lambda > 0$ yields

$$\mathbf{b}^{T}\,(\mathbf{N} + \lambda\mathbf{I})^{-2}\,\mathbf{b} - 1 = 0, \tag{2.60}$$

and it can be shown that $\lambda = \max\{0, \bar{\lambda}\}$ where $\bar{\lambda}$ is the largest real solution of the non-linear equation (2.60) [Boyd and Vandenberghe, 2004]. In general, (2.60) has to be solved with a non-linear solver. However, in our case $\mathbf{b} \in \mathbb{R}^3$ and $\mathbf{N} \in \mathbb{R}^{3\times3}$ is always diagonal, thus (2.60) takes a comparatively simple form, and we can further analyze it by expanding it in cartesian coordinates with $\mathbf{b} = (b_x, b_y, b_z)^{\mathrm{T}}$ and $\mathbf{N} = \operatorname{diag}\left(n_x, n_y, n_z\right)$ as

$$\frac{b_x^2}{(n_x + \lambda)^2} + \frac{b_y^2}{(n_y + \lambda)^2} + \frac{b_z^2}{(n_z + \lambda)^2} - 1 = 0. \tag{2.61}$$

Rationalizing (2.61), we find that solving it is equivalent to solving for the roots of a sixth-order polynomial in λ:

$$\lambda^6 + c_5\lambda^5 + \cdots + c_1\lambda + c_0 = 0, \tag{2.62}$$

where the coefficients c_j are algebraic functions of b_x, b_y, b_z, n_x, n_y, and n_z that can be derived analytically and stored in a function as follows.

First, we define the matrices $\mathbf{N}_y := \text{diag}\left(n_y, n_z, n_x\right)$ and $\mathbf{N}_z := \text{diag}\left(n_z, n_x, n_y\right)$ by permutation of the elements of $\mathbf{N} =: \mathbf{N}_x$, and the shorthand notation $\Delta = \det(\mathbf{N})$. Then, by rewriting (2.61) as a single fraction, grouping favorably and comparing the coefficients of the λ^j to those in (2.62), we find for the c_j

$$c_5 = 2 \tag{2.63}$$

$$c_4 = -||\mathbf{b}||^2 + \text{tr}\left(\mathbf{N}_x^2 + 4\mathbf{N}_x\mathbf{N}_y\right) \tag{2.64}$$

$$c_3 = -2\Big(\mathbf{b}^T(\mathbf{N}_y + \mathbf{N}_z)\mathbf{b} - \text{tr}\left(\mathbf{N}_x^2(\mathbf{N}_y + \mathbf{N}_z)\right) - 4\Delta\Big) \tag{2.65}$$

$$c_2 = -\mathbf{b}^T(\mathbf{N}_y^2 + \mathbf{N}_z^2 + 4\mathbf{N}_y\mathbf{N}_z)\mathbf{b} + \text{tr}\left(\mathbf{N}_y^2\mathbf{N}_z^2\right) + 4\Delta \tag{2.66}$$

$$c_1 = -2\Big(\mathbf{b}^T(\mathbf{N}_y\mathbf{N}_z(\mathbf{N}_y + \mathbf{N}_z))\mathbf{b} - \Delta\text{tr}\left(\mathbf{N}_x\mathbf{N}_y\right)\Big) \tag{2.67}$$

$$c_0 = -\mathbf{b}^T(\mathbf{N}_y^2\mathbf{N}_z^2)\mathbf{b} + \Delta^2 \tag{2.68}$$

where tr $(\,\cdot\,)$ designates the matrix trace function.

Now, we can use a root solver, such as the `roots` function of MATLAB, that uses the c_j's as inputs, to compute $\bar{\lambda}$, which now is the largest real root of (2.62). This algorithm considers the result from linear algebra that the polynomial equation (2.62) is the characteristic equation of its companion square matrix

$$\mathbf{C} = \begin{pmatrix} 0 & 0 & 0 & 0 & 0 & -c_0 \\ 1 & 0 & 0 & 0 & 0 & -c_1 \\ 0 & 1 & 0 & 0 & 0 & -c_2 \\ 0 & 0 & 1 & 0 & 0 & -c_3 \\ 0 & 0 & 0 & 1 & 0 & -c_4 \\ 0 & 0 & 0 & 0 & 1 & -c_5 \end{pmatrix}, \tag{2.69}$$

since $\det(\lambda\mathbf{I} - \mathbf{C}) = 0$ will yield (2.62). Thus, the roots of (2.62) can be calculated as the eigenvalues of $\mathbf{C}$.

The computation of $\bar{\lambda}$ (and consequently of $\mathbf{M}$) using the eigenvalues of $\mathbf{C}$ is faster compared to a global minimization algorithm. Thus, we have converted the global minimization problem into a structured polynomial root-solving problem and eliminated the necessity for a good initial value. Note also, that for a given shape, thus a given $\mathbf{N}$, most entries of the coefficients c_j can be precomputed, and hence the computation times can be decreased further, as only the pre-and post-multiplication with $\mathbf{b}$ need to be performed at run-time.

2.9.1 Interpretation of the Lagrange Multiplier

First, note that we find the saturating field by solving (2.60) for the "just saturation" case characterized by $\mathbf{b} = ||\mathbf{b}||_{\text{sat}}\mathbf{e}_\text{b}$ and $\lambda = 0$, as

$$||\mathbf{b}||_{\text{sat}} = \frac{1}{\sqrt{\mathbf{e}_\text{b}^\text{T}\mathbf{N}^{-2}\mathbf{e}_\text{b}}}. \tag{2.70}$$

We observe that the saturating field is dependent on the direction $\mathbf{e}_\text{b}$ of the applied field. As will be shown in Section 2.10, this is the general expression for the saturating field derived by Abbott et al. [2007].

Now, for an interpretation of λ, consider the special case of an axial field by setting $b_x \neq 0$, and $b_y = b_z = 0$. Then, (2.61) can be solved directly yielding

$$\bar{\lambda}_x = b_x - n_x. \tag{2.71}$$

We see that $\bar{\lambda}_x < 0$ for sufficiently low applied fields b_x and increases linearly with b_x. Saturation is reached when $\bar{\lambda}_x = 0$, i.e., when $b_x = b_{x,\text{sat}} = n_x$. After saturation $\bar{\lambda}_x$ keeps increasing with b_x, and we have $\bar{\lambda}_x \approx b_x$ for $b_x \gg n_x$. This means that for low fields the shape has an influence (since n_i cannot be neglected) while for large fields the shape has no influence on the magnetization.

Thus, the Lagrange multiplier is non-dimensional, and phenomenologically represents the saturation state of the x direction, i.e., the higher λ_x, the more *the x-axis is saturated*. In general, λ represents the general magnetization state of the sample, and we will show in the next section how the applied field can be used to estimate boundaries for λ and, thus, for the magnetization.

In the following, we will drop the explicit distinction between $\bar{\lambda}$ and λ and just use λ designating a non-negative real number.

2.9.2 Boundaries of the Lagrange Multiplier

We recall the following result from linear algebra without proof.
Let $\mathbf{Q} \in \mathbb{R}^{n\times n}$ be a symmetric positive definite matrix, i.e, $\mathbf{x}^T\mathbf{Q}\mathbf{x} > 0$ for all $\mathbf{x} \in \mathbb{R}^n$ and let $\sigma_{max} = \sigma_1 \geq \sigma_2 \geq \cdots \geq \sigma_n = \sigma_{min}$ be its eigenvalues. Then, it holds that

$$\sigma_1||\mathbf{x}||^2 \geq \mathbf{x}^\text{T}\mathbf{Q}\mathbf{x} \geq \sigma_n||\mathbf{x}||^2, \quad \forall \mathbf{x} \in \mathbb{R}^n. \tag{2.72}$$

Thus, the eigenvalues determine the boundaries of the quadratic form $\mathbf{Q}(\mathbf{x}) = \mathbf{x}^\text{T}\mathbf{Q}\mathbf{x}$.

Now, we note that the constraint (2.60) is an equality for a quadratic form

$$\mathbf{b}^\text{T}\left(\mathbf{N} + \lambda\mathbf{I}\right)^{-2}\mathbf{b} = 1 \tag{2.73}$$

with $\mathbf{Q} = \left(\mathbf{N} + \lambda\mathbf{I}\right)^{-2}$ being a diagonal positive definite matrix (since $n_i > 0$ and $\lambda \geq 0$) with eigenvalues $\sigma_i = 1/(n_i + \lambda)^2$. In particular we have

$$\sigma_\text{max} = \frac{1}{(n_\text{min} + \lambda)^2}, \tag{2.74}$$

and

$$\sigma_{\min} = \frac{1}{(n_{\max} + \lambda)^2}, \tag{2.75}$$

for all $\lambda \geq 0$. Applying the inequality (2.72) to (2.73) yields

$$\sigma_{\max} ||\mathbf{b}||^2 \geq \mathbf{b}^{\mathrm{T}} \left(\mathbf{N} + \lambda \mathbf{I}\right)^{-2} \mathbf{b} \geq \sigma_{\min} ||\mathbf{b}||^2 \tag{2.76}$$

or, equivalently

$$\sigma_{\max} ||\mathbf{b}||^2 \geq 1 \geq \sigma_{\min} ||\mathbf{b}||^2, \tag{2.77}$$

and with (2.74) and (2.75) we can derive, after some manipulation, the boundaries on λ as

$$||\mathbf{b}|| - n_{\max} \leq \lambda \leq ||\mathbf{b}|| - n_{\min}, \tag{2.78}$$

or

$$\lambda \in \Big(||\mathbf{b}|| - n_{\max}, ||\mathbf{b}|| - n_{\min} \Big). \tag{2.79}$$

Or, more exactly, since λ is non-negative,

$$\lambda \in \Big(\max\left(0, ||\mathbf{b}|| - n_{\max}\right), \max\left(0, ||\mathbf{b}|| - n_{\min}\right) \Big). \tag{2.80}$$

In other words, $||\mathbf{b}||$ defines three intervals for λ as

$$\lambda \in \begin{cases} 0, & ||\mathbf{b}|| < n_{\min} \\ \left(0, ||\mathbf{b}|| - n_{\min}\right), & n_{\min} \leq ||\mathbf{b}|| < n_{\max} \\ \left(||\mathbf{b}|| - n_{\max}, ||\mathbf{b}|| - n_{\min}\right), & ||\mathbf{b}|| > n_{\max} \end{cases} \tag{2.81}$$

where the first interval corresponds to the linear case and the last one to the fully saturated case. In the middle interval, both, linear and saturated behavior are possible depending on the direction of $\mathbf{b}$.

In summary, we have derived boundaries on the Lagrange multiplier which will allow to determine boundaries on quantities depending on λ, in particular the magnetic torque as will be shown in Chapter 3.

2.9.3 Approximate Direct Computation of λ

To avoid the root solving procedure alltogether, to further decrease the computation speed, or just to get an estimate on the magnetization, we need to approximate λ. For this, we have to approximate the constraint (2.60)

$$\mathbf{b}^T \left(\mathbf{N} + \lambda \mathbf{I}\right)^{-2} \mathbf{b} - 1 = 0 \tag{2.82}$$

to solve for λ for the general case with $\mathbf{b} = ||\mathbf{b}|| \mathbf{e}_{\mathrm{b}}$.

First, note that for sufficiently large values of $||\mathbf{b}||$, without any approximation, λ must increase at some point such that $\lambda \gg n_i$ and, thus, dominates the denominator. Solving (2.82) in this limit of large $||\mathbf{b}||$ yields

$$\lambda = ||\mathbf{b}||, \text{ for } ||\mathbf{b}|| \gg n_{\max}, \tag{2.83}$$

and, thus, allows for the investigation of this limit case without any approximation of λ. Note that, for this limit case, this result is also obtained from the last boundary (2.81) as it reduces to $\lambda \in (||\mathbf{b}||, ||\mathbf{b}||)$, thus $\lambda = ||\mathbf{b}||$.

To derive an approximation we observe that the diagonal entries of $(\mathbf{N} - \lambda\mathbf{I})^{-2}$ are

$$\frac{1}{(n_i + \lambda)^2}, \tag{2.84}$$

and a linear approximation using Taylor expansion around $\lambda = 0$ yields

$$\frac{1}{(n_i + \lambda)^2} \approx n_i^{-2} - 2\lambda n_i^{-3}, \tag{2.85}$$

or in matrix form

$$(\mathbf{N} - \lambda\mathbf{I})^{-2} \approx \mathbf{N}^{-2} - 2\lambda\mathbf{N}^{-3}. \tag{2.86}$$

Now, we can solve (2.82) for λ to find

$$\lambda \approx \lambda_0(\mathbf{N}, \mathbf{b}) \coloneqq \frac{\mathbf{b}^{\mathrm{T}}\mathbf{N}^{-2}\mathbf{b} - 1}{2\mathbf{b}^{\mathrm{T}}\mathbf{N}^{-3}\mathbf{b}}, \tag{2.87}$$

or, in terms of the saturating field

$$\lambda_0(\mathbf{N}, \mathbf{b}) = \frac{1}{2\mathbf{e}_{\mathrm{b}}^{\mathrm{T}}\mathbf{N}^{-3}\mathbf{e}_{\mathrm{b}}} \cdot \left(\frac{1}{||\mathbf{b}||^2_{\mathrm{sat}}} - \frac{1}{||\mathbf{b}||^2} \right) \tag{2.88}$$

This approximation is valid near $\lambda = 0$, that is, at the transition from linear to saturated behavior. Figure 2.4 shows a typical λ vs. applied field plot for a random direction $\mathbf{e}_{\mathrm{b}}$ and a random $\mathbf{N}$, together with the Taylor approximation λ_0 and the boundaries (2.80). We clearly see the linear dependence of λ with b for $\lambda > 0$, and also that the Taylor approximation is only valid very close to the transition from $\lambda = 0$ to $\lambda > 0$.

To derive an approximation λ_β for larger λ, and thus larger $||\mathbf{b}||$, we make the assumption that λ has an affine relationship with $||\mathbf{b}||$ as

$$\lambda \approx \lambda_\beta(\mathbf{N}, \mathbf{b}) \coloneqq \alpha + \beta||\mathbf{b}|| \tag{2.89}$$

with $\alpha, \beta \in \mathbb{R}$, and $\alpha = \alpha(\mathbf{e}_{\mathrm{b}}, \mathbf{N})$ and $\beta = \beta(\mathbf{e}_{\mathrm{b}}, \mathbf{N})$, that is, the coefficients do not depend on the applied field magnitude, only its direction and the shape. This is motivated by the form of the boundaries (2.78) and by the affine form of the curve for λ in Fig. 2.4. To determine α and β we require for λ_β the identical transition behavior as λ_0 for $||\mathbf{b}|| = ||\mathbf{b}||_{\mathrm{bsat}}$, specifically, the same value

$$\lambda_\beta(||\mathbf{b}||_{\mathrm{bsat}}) = \lambda_0(||\mathbf{b}||_{\mathrm{bsat}}) \tag{2.90}$$

and the same slope

$$\frac{\partial\lambda_\beta(||\mathbf{b}||_{\mathrm{bsat}})}{\partial||\mathbf{b}||} = \frac{\partial\lambda_0(||\mathbf{b}||_{\mathrm{bsat}})}{\partial||\mathbf{b}||}. \tag{2.91}$$

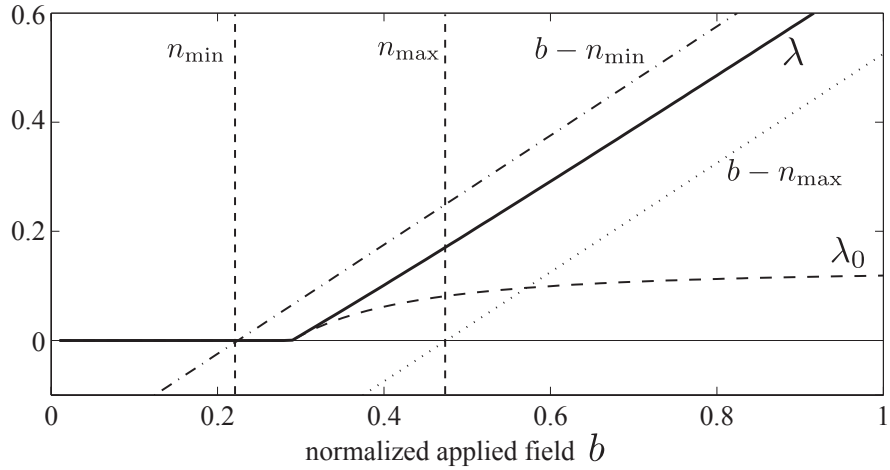

Figure 2.4: A typical plot of λ vs. applied field for a random direction $\mathbf{e}_b$ and a random $\mathbf{N}$, together with the Taylor approximation λ_0 and the boundaries (2.80).

We find

$$\beta = \frac{\left(\sqrt{\mathbf{e}_b^T \mathbf{N}^{-2} \mathbf{e}_b}\right)^3}{\mathbf{e}_b^T \mathbf{N}^{-3} \mathbf{e}_b} \tag{2.92}$$

and

$$\alpha = -\frac{\beta}{\sqrt{\mathbf{e}_b^T \mathbf{N}^{-2} \mathbf{e}_b}}. \tag{2.93}$$

Inserting these in (2.89) yields the approximation

$$\lambda_\beta = \frac{\sqrt{\mathbf{e}_b^T \mathbf{N}^{-2} \mathbf{e}_b}}{\mathbf{e}_b^T \mathbf{N}^{-3} \mathbf{e}_b} \left(||\mathbf{b}|| \sqrt{\mathbf{e}_b^T \mathbf{N}^{-2} \mathbf{e}_b} - 1 \right) \tag{2.94}$$

or, in terms of the saturating field

$$\lambda_\beta = \frac{1}{||\mathbf{b}||_{sat} \mathbf{e}_b^T \mathbf{N}^{-3} \mathbf{e}_b} \left(\frac{||\mathbf{b}||}{||\mathbf{b}||_{sat}} - 1 \right). \tag{2.95}$$

This approximation yields the same transition from linear to saturation as the Taylor approximation λ_0 and is only to be used if a positive value is computed. Furthermore, using this approximation no root solving or numerical minimization is necessary to compute the magnetization of a sample given the applied field angle and magnitude, which decreases the computation time considerably.

While λ_β gives the correct transition at $||\mathbf{b}|| = ||\mathbf{b}||_{sat}$, and, as we will see, also for larger $||\mathbf{b}||$, it may introduce errors for situations close to the uniaxial

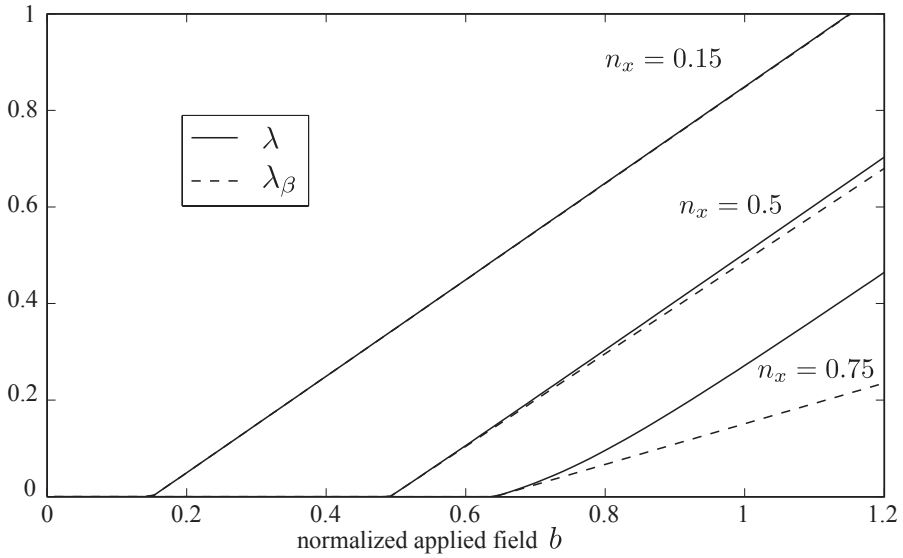

Figure 2.5: The approximation λ_β for λ shows the correct transition at $\lambda = 0$. However, for large demagnetizing factors and fields applied in the corresponding direction, large errors may occur.

case. For this, consider w.l.o.g[3] $\mathbf{e}_\mathrm{b} = (1, 0, 0)^\mathrm{T}$, that is, a field applied in the x direction. Then, with $||\mathbf{b}|| = b$, and $b_\mathrm{sat} = n_x$, (2.95) yields

$$\lambda_\beta = n_x \left(b - n_x\right), \tag{2.96}$$

thus, a value that is scaled by n_x compared to the expected value (2.70). The relative error of the approximation in this case is

$$\left|\frac{\lambda_\beta - \lambda_x}{\lambda_x}\right| = \left|\frac{n_x(b - n_x) - (b - n_x)}{b - n_x}\right| = |n_x - 1|\,. \tag{2.97}$$

Since $0 < n_x \leq 1$, the error is small and can be neglected for n_x close to 0, but can considerable for larger n_x. This is shown in Fig. 2.5 for $n_x = 0.15, 0.5$ and 0.75 and $\mathbf{e}_\mathrm{b} = (.99, .01, 0)^\mathrm{T}$. Clearly, the approximation is very good for $n_x = 0.15$, good for $n_x = 0.5$ and poor for $n_x = 0.75$. Of course, if it is known that the field is uniaxial, one can directly use the correct value (2.70) for λ which also corresponds to one of its limit values.

2.10 The Planar Case

The planar (2D) case with the demagnetizing factors n_x and n_y, and $\mathbf{b} = b\left(\cos\theta, \sin\theta, 0\right)^\mathrm{T}$ is instructive, and will be used extensively in the next chapter. In addition, this case is studied in Abbott et al. [2007], which will be used as a validation of the proposed method and will demonstrate that our results

[3] without loss of generality

from the previous section reduce to standard results for magnetization computation.

First, the saturation field (2.70) reduces to

$$b_{\text{sat}} = \frac{n_x n_y}{\sqrt{n_y^2 \cos^2\theta + n_x^2 \sin^2\theta}}, \tag{2.98}$$

which is the result (2.46) derived in Abbott et al. [2007]. We can rewrite it with respect to n_x as

$$\frac{b_{\text{sat}}}{n_x} = \frac{n_y/n_x}{\sqrt{\frac{n_y^2}{n_x^2}\cos^2\theta + \sin^2\theta}} \tag{2.99}$$

and observe its evolution for $\theta \in (0^\circ, 90^\circ)$ and different n_y/n_x ratios as shown in Fig. 2.6. Because of the quadratic trigonometric terms and $n_y/n_x > 1$, the cos-term dominates the saturating field, and we see that for angles up to approximately 50°, we have $b_{\text{sat}}/n_x \approx 1$, meaning the saturating field is approximately equal to the smallest demagnetizing factor, and is independent of the angle θ and the actual n_y/n_x ratio and thus shape. On the other hand, for $\theta \approx 90^\circ$, we have, as expected, $b_{\text{sat}}/n_x \approx n_y/n_x$ (or $b_{\text{sat}} \approx n_y$). Thus, only for the range of angles $\theta \in (60^\circ, 80^\circ)$, the actual shape ratio n_y/n_x plays a significant role in determining the saturation field (depending on the required accuracy).

Next, using λ we can observe the continuous evolution of the direction and the magnitude of the magnetization. The non-dimensional magnetization is given by (2.59)

$$\mathbf{x} = (\mathbf{N} + \lambda \mathbf{I})^{-1}\,\mathbf{b} \tag{2.100}$$

and with $\mathbf{x} = \left(x_1, x_2\right)^{\mathrm{T}}$, we have

$$\left(x_1, x_2\right)^{\mathrm{T}} = b\left(\frac{\cos\theta}{n_x + \lambda}, \frac{\sin\theta}{n_y + \lambda}\right)^{\mathrm{T}}. \tag{2.101}$$

Thus, the magnitude $||\mathbf{x}||$ is found as

$$||\mathbf{x}|| = b\sqrt{\left(\frac{\cos\theta}{n_x + \lambda}\right)^2 + \left(\frac{\sin\theta}{n_y + \lambda}\right)^2}, \tag{2.102}$$

and recalling that $\lambda \approx b$ for sufficiently large b, we have

$$||\mathbf{x}|| \propto b, \text{ for } \lambda \to 0 \tag{2.103}$$

$$||\mathbf{x}|| = 1, \text{ for } \lambda \to \infty, \tag{2.104}$$

in other words, we find what we expect; for low fields, the magnetization is linear with the applied field, while for large fields, the magnetization saturates.

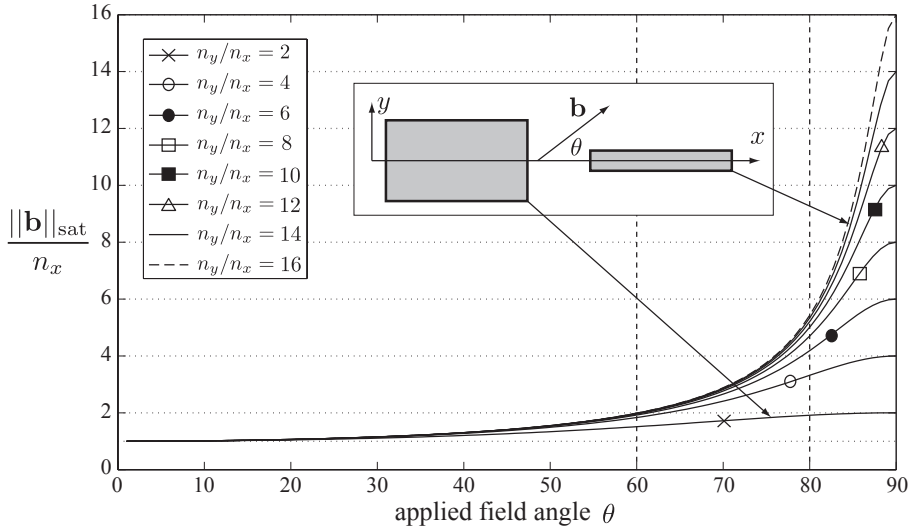

Figure 2.6: Saturation field as a function of the applied field direction θ for the planar case for various n_y/n_x ratios. This plot can be used to estimate the saturating field for a vast range of shapes, as schematically indicated by the inset. Note, however, that depending on the required accuracy, the ratio n_y/n_x is only needed for $\theta \in (60^\circ, 80^\circ)$. For $\theta < 60^\circ$, we have $b_{\text{sat}} \approx n_x$, while for $\theta > 80^\circ$, $b_{\text{sat}} \approx n_y$ is a good approximation.

The angle ϕ between the x-axis and $\mathbf{x}$ is found from $\tan\phi = x_2/x_1$ as

$$\tan\phi = \frac{n_x + \lambda}{n_y + \lambda}\tan\theta \Longleftrightarrow \phi = \arctan\left(\frac{n_x + \lambda}{n_y + \lambda}\tan\theta\right). \tag{2.105}$$

Inspecting the limit cases $\lambda \to 0$ and $\lambda \to \infty$ shows

$$\phi = \arctan\left(\frac{n_x}{n_y}\tan\theta\right), \text{for } \lambda \to 0 \tag{2.106}$$

$$\phi = \theta, \text{ for } \lambda \to \infty \tag{2.107}$$

and (2.106) is the same as (2.43) given by Abbott et al. [2007], while (2.107) is the standard assumption that for high fields the direction of the magnetization approaches the direction of the applied field.

For verification, we compare the magnetization as computed exactly by λ and approximated by λ_β for the prolate ellipsoid studied experimentally by Abbott et al. [2007] (see inset Fig. 2.7(a)). The ellipsoid was machined from HyMu80, an almost ideal soft-magnetic material with saturation magnetization $m_s = 6.163 \times 10^5$A/m, and with length 4.90mm (in x dir.) and width 2.54mm (in y and z dir.), resulting in $n_x = 0.18$ and $n_y = 0.41$.

The results are shown in Figure 2.7(a). Our results are identical to those by Abbott et al. [2007] (not shown) because of the equivalent model, and we can observe an excellent prediction of the experimental data by our model

using λ. When the approximation λ_β is used, the transition from linear to saturated behavior is well captured as expected. For higher fields, an overestimate of the magnetization is seen, stemming from the approximation of the constraint. As shown in Fig. 2.7(b), the maximal relative error of the magnitude of the magnetization due this approximation stays below 10%.

The evolution of the magnetization angle θ with respect to the applied field angle θ is shown in Figure 2.7(c). Together with Fig. 2.7(a), we can observe the model behavior. The applied field is divided in three regions by n_x and n_y. For $b < n_x$, thus $\lambda = 0$, we have linear behavior and for $b > n_y$ ($\lambda > 0$) we have full saturation of the ellipsoid. In between, transition occurs depending on the direction of the applied field. Until saturation is reached, the magnitude of the magnetization grows linearly with the applied field magnitude and the angle stays constant. After saturation, the direction of the magnetization approaches the direction of the applied field as $\theta - \phi \to 0$, while the magnitude of the magnetization remains constant.

Thus, the limit cases of our model result in classic magnetization results. Our description captures these limits accurately and allows, in addition, to the semi-analytical observation of the evolution of the magnetization of the sample.

Remark 2.2. *Note that in the planar case, the polynomial equation* (2.62) *for the constraint is reduced from the sixth to the fourth order, and allows for a closed form solution using, for example, Ferrari's method. Since the resulting expressions are rather complex and do not allow for further insight, for example on the θ dependence of λ, this approach is not pursued.*

2.11 Computation Time

As mentioned in Section (2.5.4), linear solutions are the fastest to solve. However, for situations where it is not known if the linear case applies, i.e., when the magnitude of the field varies for purposes of manipulation, the classic minimization step required induces large computation times. Here, our method provides constant fast computation times.

A comparison of the computation times of the four methods, a) classic switching between linear/saturation, b) combined minimization, c) polynomial solution and d) approximation of λ is given in Fig. 2.8. For a) the linear solution is used to initialize the minimization if necessary. For b), the initial vector is always the zero vector.

The times were determined by MATLAB's `tic/toc` algorithm on a MacBookPro2009, for calculating the magnetization $\mathbf{x}$ for a given $\mathbf{N}$, 20 random directions $\mathbf{e}_b$, and increasing field strength b. Clearly, for sufficiently low fields, thus in the linear region, the classic method is the fastest, about 40 to 50 times faster than the polynomial solution. For saturation solutions the polynomial solution yields about the same increase in speed compared to the classic method. Note, however, that overall, our method provides fast com-

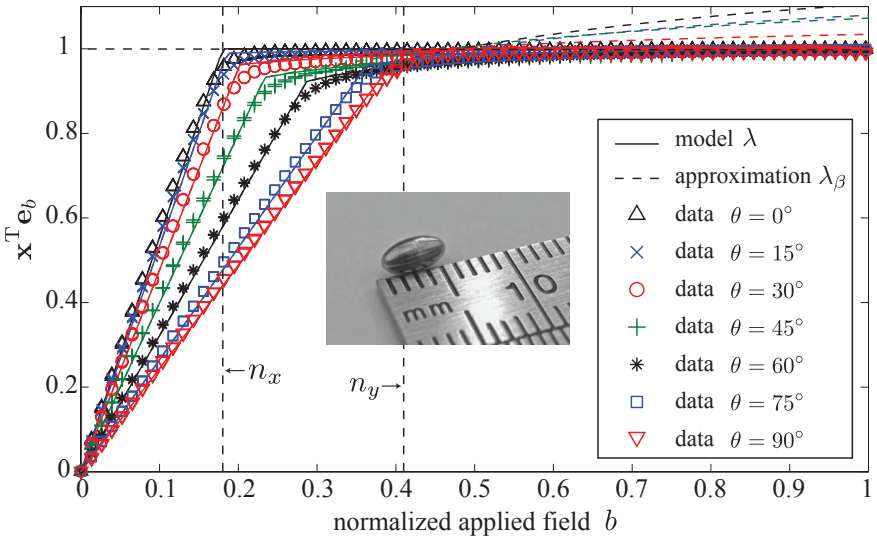

(a) Magnetization in the direction of the applied field $\mathbf{x}^T\mathbf{e}_b$. Excellent correspondence between the model and the data is observed. The approximation overpredicts for larger fields.

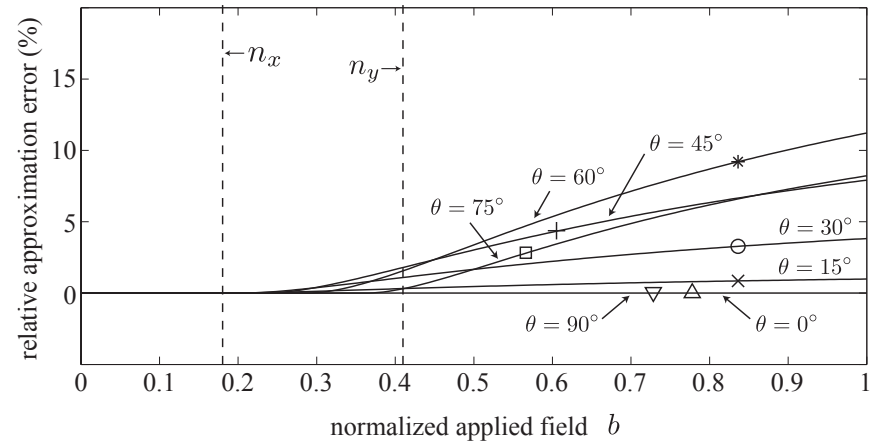

(b) The maximal relative error for the approximation of the magnetization for this case is about 10%.

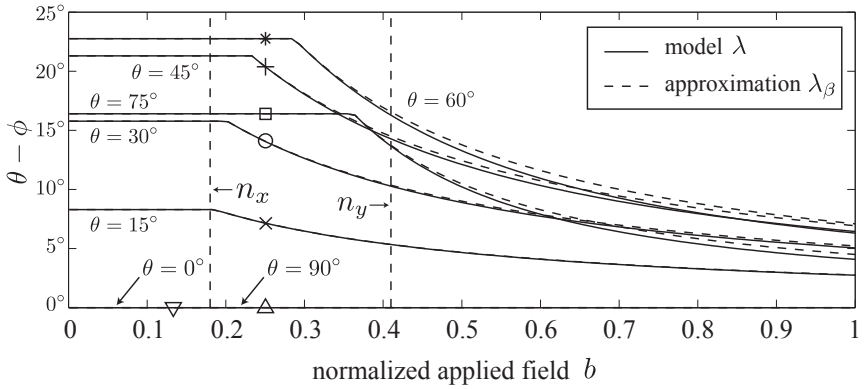

(c) Before saturation the angle stays constant. When saturation is reached the magnetization starts to tend toward the direction of the applied field as $\theta - \phi \to 0$.

Figure 2.7: (a) Experimental verification of the proposed method for the ellipsoid studied by Abbott et al. [2007] with $n_x = 0.18$, $n_y = 0.41$, and $m_s = 6.163 \times 10^5$A/m. (b) Relative error of the magnetization due to the approximation λ_β. (c) Magnetization angle θ with respect to the applied field angle ϕ. The markers for the angle θ in (b) and (c) correspond to those in (a)

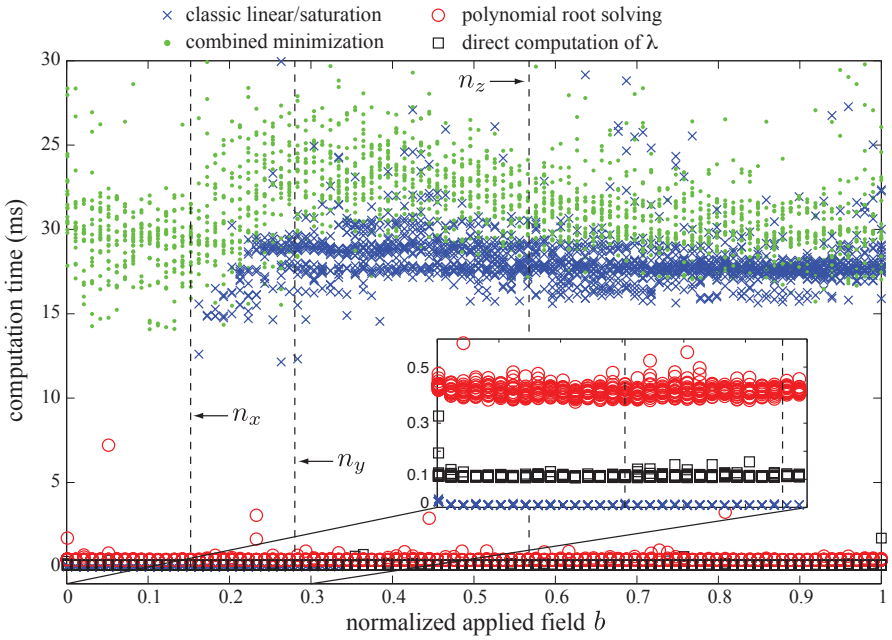

Figure 2.8: Computation times for determining the magnetization on a shape with random **N** and 20 random field directions. The classic method (crosses) is superior in the linear region, but has increased computation times in the saturation region. The proposed method (circle) yields constant low computation times across the saturation borders.

putation times, which remain constant over the saturation limits and, thus, should be the method of choice when dealing with uncertain magnetizations.

2.12 The Inverse Problem

The advantage of using a description involving λ is that it describes the magnetization state of a sample incorporating both direction and magnitude of the applied field into a single variable. Thus, the same magnetization state is achievable with different combinations of field strength and direction.

This makes the inverse problem, where a specific magnetization state is desired, complex, and closed-form solutions may not exist as can easily be seen by considering inverting the approximation (2.94). It is more advantageous to solve the problem numerically. For this, one must consider that λ is bounded by (2.80), and in the case of $\lambda > 0$ it also must fulfill the constraint (2.60).

2.13 Summary and Contributions

This chapter has introduced the necessary background to calculate the magnetization of a soft-magnetic body when placed in an externally applied mag-

netic field. The contributions of this chapter are as follows.

We have generalized the model presented by Abbott et al. [2007] by combining the linear and saturated region into a single constrained minimization step, even including coercivity. In addition, capitalizing on the structure of the minimization problem we have reformulated it as a root-solving problem that enables fast computation of the magnetization required in real-time control systems, such as for model-based controllers.

Furthermore, we have investigated the optimization problem analytically by introducing a Lagrange multiplier λ that enforces the constraint. We have derived its boundaries and proposed an interpretation. We have demonstrated that calculating the magnetization using λ yields results identical to the standard method. The advantage of our method is that the standard results are obtained as limit cases, and the transition between these limits can be investigated semi-analytically.

Next, we have analytically approximated λ. For the transition region, we found an approximation of λ based on a Taylor series expansion of the constraint. Motivated by these results, we have extended the approximation to an affine function yielding the same transition behavior as the Taylor approximation, while approximating λ over all applied field magnitudes and angles.

In brief, these results allow for the analytical computation of the magnetization for a given arbitrary field $\mathbf{b}$, without the need for numerical minimization procedures. In addition, we can treat the linear and the saturated case without having to explicitly distinguish the two cases but rather by limit considerations.

Since the magnetic force and torque depend on the magnetization, the same simplifications in their treatment are achieved, i.e. fast computation and analytical combination of linear and saturation region, and no need for minimization.

2.14 References

Abbott, J. J., Ergeneman, O., Kummer, M. P., Hirt, A. M., and Nelson, B. J. (2007). Modeling magnetic torque and force for controlled manipulation of soft-magnetic bodies. *IEEE Trans. on Robotics*, 23(6):1247–1252.

Beleggia, M., De Graef, M., and Millev, Y. T. (2006). The equivalent ellipsoid of a magnetized body. *J. Physics D*, 39(5):891–899.

Boyd, S. and Vandenberghe, L. (2004). *Convex Optimization*. Cambridge University Press.

Brugger, S. and Paul, O. (2010). Magnetic field amplification by slender cuboid-shaped magnetic concentrators with a single gap. *Sensors and Actuators A: Physical*, 157(1):135 – 139.

Bryson, A. E. and Ho, Y. C. (1975). *Applied Optimal Control: Optimization, Estimation, and Control*. Wiley, New York.

Furlani, E. P. (2001). *Permanent Magnet and Electromechanical Devices*. Academic Press, San Diego, CA.

Gilbert, W. (1600). *De Magnete, Magneticisque Corporibus, et de Magno Magnete Tellure (On the Magnet and Magnetic Bodies, and on That Great Magnet the Earth)*. Peter Short, London, 1st, latin edition.

Judy, J. W. and Muller, R. S. (1997). Magnetically actuated, addressable microstructures. *J. Microelectromech. Syst.*, 6(3):249–256.

Kummer, M. P., Abbott, J. J., Vollmers, K., and Nelson, B. J. (2007). Measuring the magnetic and hydrodynamic properties of assembled-MEMS microrobots. In *Proc. IEEE Int. Conf. Robot. Automat.*, pages 1122–1127.

Maxwell, J. C. (1865). A dynamical theory of the elctromagnetic field. *Philosophical Trans. of the Royal Society of London*, 155:459–512.

Osborn, J. A. (1945). Demagnetizing factors of the general ellipsoid. *Physical Review*, 67(11-12):351.

CHAPTER 3

Magnetic Force and Torque on Assembled-MEMS Microrobots

Using the description of the magnetization introduced in the previous chapter, we give the resulting expressions of the magnetic torque exerted on planar shapes placed in an applied magnetic field. We analyze the torque resulting in a general non-dimensional torque curve. We then investigate situations involving multiple planar shapes and give arguments that in most cases their magnetic interaction can be neglected. Using our torque description, we analyze torque ratios of specific configurations and conclude that dominant shapes exist allowing for further simplification of the computation. We conclude the chapter by applying our findings to the ophthalmic microrobot presented in Yesin et al. [2006] and Kummer et al. [2010].

3.1 Introduction

Fabricating truly 3D mechanical structures at the microscale is challenging. With current MEMS fabrication methods, mechanical parts are built using 2D (planar) geometries with desired thickness. Three-dimensional structures can be obtained by bending or assembling these planar parts (Fig. 3.1), and it has been demonstrated that very complex structures can be built with such methods [Iwase and Shimoyama, 2005; Syms et al., 2003; Yang et al., 2005].

Assembled-MEMS microrobots have the potential to provide increased functionality over simpler geometries, as MEMS sensors and actuators can be incorporated onto the body of the microrobot. A microrobot that is assembled from electroplated nickel components has been developed recently by Yesin et al. [2006], and 2-DOF magnetic control (1-DOF rotation, 1-DOF

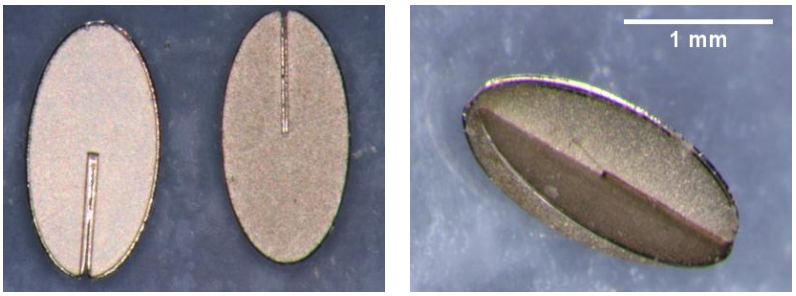

(a) Individual nickel parts (b) Assembled microrobot

Figure 3.1: [

Relatively simple 2D parts can be assembled into complex 3D structures]Relatively simple 2D parts can be assembled into complex 3D structures. The parts shown have dimensions 2.0 mm $\times$ 1.0 mm $\times$ 42 µm, and can be further miniaturized.

translation) was demonstrated in a planar fluid-filled maze.

Models of soft-magnetic MEMS microactuators with simple planar geometries, e.g. cantilevers, have been developed by Judy and Muller [1997]. However, there is no prior work on modeling the magnetic properties of assembled structures, which is needed for precise control of our proposed untethered devices. Consider, for example, the microrobot in Fig. 3.1. In the standard approach, the complex, assembled shape is simplified to a single ellipsoid having the same overall dimensions. This results in an ellipsoid with a circular cross section perpendicular to its long axis because of the equal dimensions of the microrobot. Because of this symmetry, equal demagnetizing factors are found for these directions, and, hence, no torque around the long axis is predicted. However, experimentally, a torque can be measured. Consequently, there is a clear need to modify the current models. Finite element methods (FEM) can be used to model magnetic behavior of arbitrary assemblies but are impractical in real-time control of magnetic devices because of long computation times.

The contributions of this chapter are as follows. We first derive a general non-dimensional torque curve using our description of the magnetization introduced in the previous chapter. We demonstrate that, as expected, it reproduces standard results as limit cases. In addition, we can analyze the torque by applying the properties of the Lagrange multiplier. From our results a $\sin(2\theta)$ behavior for the torque follows naturally for both low and high fields without further assumptions.

Also, we predict that for a field applied at an angle $\theta < 45°$, for example, the torque will always increase with the magnitude of the applied field and asymptotically reach its limit value. For larger angles, the torque may decrease after saturation, or continue increasing to a maximum value and then decrease asymptotically to its limit. This has been previously observed

but without the ability to predict the limit at 45°. Furthermore, knowing the boundaries of the involved Lagrange multiplier allows us to identify not only maximal torques, but also minimal torques on shapes, allowing for design optimization.

We then investigate the superposition of shapes and give phenomenological arguments that, in most cases superposition can be neglected. We argue that configurations may exist where one or only a few shapes dominate the total torque on assembled structures. Finally, we propose that assembled devices should be modeled as the superposition of simple geometries, and verify this experimentally and numerically with a microrobot assembled from electroplated nickel parts, showing that we can predict the torque along the long axis of the microrobot.

3.2 Single Soft-Magnetic Body

The magnetic force $\mathbf{F}$ and torque $\mathbf{T}$ acting on a body inside an arbitrary, closed surface S and placed in a magnetic field can be computed as

$$\mathbf{F} = \oint_S \boldsymbol{\sigma}_{\boldsymbol{M}} \cdot \mathbf{n} \, \mathrm{d}S, \tag{3.1}$$

$$\mathbf{T} = \oint_S \mathbf{r} \times (\boldsymbol{\sigma}_{\boldsymbol{M}} \cdot \mathbf{n}) \, \mathrm{d}S, \tag{3.2}$$

where $\mathbf{n}$ is an outwards normal vector on the surface S, $\mathbf{r}$ is the position of the body, and $\boldsymbol{\sigma}_{\boldsymbol{M}}$ is the Maxwell stress tensor given by

$$\boldsymbol{\sigma}_{\boldsymbol{M}} = \mathbf{H} \otimes \mathbf{B} - \frac{1}{2} (\mathbf{H} \cdot \mathbf{B}) \, \mathbf{I} \tag{3.3}$$

with $\otimes$ representing the dyadic product[1] and $\mathbf{I}$ the unity tensor. The constitutive relationship $\mathbf{B}(\mathbf{H})$ must be chosen in the material that is crossed by S.

Equations (3.1) and (3.2) are commonly used in finite element software to compute magnetic forces and torques on bodies. Yet, analytical evaluation is not practical. Instead, one assumes that the body with volume V is magnetized by $\mathbf{H}$ to the magnetization $\mathbf{M}$, and behaves, consequently, as a dipole with dipole moment $\boldsymbol{\Gamma} = \mathbf{M}V$. Then, it is possible to apply the force and torque expressions on dipoles given by

$$\mathbf{F} = \mu_0 \int_V (\mathbf{M} \cdot \nabla)\mathbf{H} \, \mathrm{d}\nu \approx \mu_0 V (\mathbf{M} \cdot \nabla)\mathbf{H} \tag{3.4}$$

$$\mathbf{T} = \mu_0 \int_V (\mathbf{M} \times \mathbf{H}) \, \mathrm{d}\nu \approx \mu_0 V \mathbf{M} \times \mathbf{H} \tag{3.5}$$

For completeness, note that the force and torque expression can also be expressed with the magnetic flux density $\mathbf{B}$, since in air $\mathbf{B} = \mu_0 \mathbf{H}$. In general, $\mathbf{M}$ and $\mathbf{H}$ vary over the body, hence the integral expressions. The simplifying

[1] The dyadic product $\mathbb{P} = \mathbf{u} \otimes \mathbf{v}$ of a column vector $\mathbf{u}$ and a row vector $\mathbf{v}$ is a tensor of rank two. The entries are given by $\mathbb{P}_{ij} = u_i v_j$ (using Einstein's summation convention)

expressions consider only **H** at the center of mass of the body, which is an adequate assumption when the body is small compared to spatial changes in the applied field, and assuming uniform magnetization **M**.

Equation (3.4) is a compact notation for a complex operation. However, using the constraint provided by Maxwell's equation (2.5) (with $\mathbf{J} = 0$), we can express (3.4) in a more intuitive form

$$\mathbf{F} = \mu_0 V \left[\mathbf{M} \cdot \frac{\partial \mathbf{H}}{\partial x}, \quad \mathbf{M} \cdot \frac{\partial \mathbf{H}}{\partial y}, \quad \mathbf{M} \cdot \frac{\partial \mathbf{H}}{\partial z} \right]^T . \tag{3.6}$$

Comparing (3.5) and (3.6), we observe that the magnetic force depends on the spatial gradient of the magnetic field, while the magnetic field depends on its magnitude and direction. However, since in the case of soft-magnetic materials the magnetization also depends on the strength and the direction of the magnetic field, the force depends on the spatial gradient, the strength, and the direction of the magnetic field **H**, making its understanding complex and unintuitive.

However, as argued by Abbott et al. [2007], because we can always apply higher forces by generating higher gradients, we can limit our investigation to the magnetic torque. In the force expression, the field is decoupled from the field gradient. Hence, knowledge of the field allows prediction of the magnetization as discussed in the previous section. Then, the field gradient allows for the computation of the force.

Remark 3.1. *As a reference for later discussions, note that for a permanent magnet* **M** *is fixed, i.e., independent of* **H**. *Then, the magnitude of the torque* (3.5) *follows a* $\sin\theta$ *behavior where* θ *is the angle between* **M** *and* **H**, *since* $||\mathbf{T}|| = \mu_0 V ||\mathbf{M}|| ||\mathbf{H}|| \sin\theta$.

3.2.1 Assumptions for the Investigation

For the analytical treatment, we set the body coordinate frame such that the x-axis is aligned with the longest axis of the body, and the z-axis with the shortest; the y-axis is oriented such that a right-handed coordinate frame is obtained. It follows from this convention that the demagnetizing factors fulfill $n_x \leq n_y \leq n_z$.

Demagnetizing Factors

Beleggia et al. [2006] state that any uniformly magnetized body can be related to a magnetically equivalent ellipsoid that has the same three demagnetizing factors n_i. They derive the exact relationships for the equivalent ellipsoids of shapes with up to two non-dimensional parameters, in particular for rectangular and elliptical plates.

Because of this equivalence, the quantities (magnetization, torque, etc.) that only involve the demagnetizing factors will remain constant and independent of the actual shape. Therefore, we will give our results in the general way, and use results where available to validate them. We use thin plates to

illustrate configurations. Whenever it is instructive, we will give typical values for a thin plate as $n_z = 0.85, n_y = 0.1, n_x = 0.05$.

Applied Field

We will assume that the applied field $\mathbf{H}$ is in one of the principal planes of the body. Without loss of generality, we set

$$\mathbf{H} = \left(h_x, h_y, 0\right)^{\mathrm{T}} = h\left(\cos\theta, \sin\theta, 0\right)^{\mathrm{T}} \tag{3.7}$$

for the planar case, where h is the magnitude of the applied field and θ the angle between $\mathbf{H}$ and the x-axis. Similarly, for the coercivity of the sample, we assume

$$\mathbf{H_c} = \left(h_{cx}, h_{cy}, 0\right)^{\mathrm{T}} = h_c\left(\cos\theta_c, \sin\theta_c, 0\right)^{\mathrm{T}} \tag{3.8}$$

where h_c is the magnitude of the coercivity and θ_c the angle between $\mathbf{H_c}$ and the x-axis. For applied fields in other planes, the results are obtained by cyclic permutation of the indices x, y and z. We recall that in non-dimensional form (see Section 2.9), we have

$$\mathbf{b} = (\mathbf{H} + \mathbf{H_c})/m_s, \tag{3.9}$$

and that we are considering the case of shape dominant magnetization (see Section (2.5.2)).

3.2.2 Classical torque analysis

Abbott et al. [2007] analyze the torque expression on ellipsoids using their continuous magnetization model (see Section 2.6). They derive the conditions on the applied field angle and field strength to obtain the maximal possible torque on the ellipsoid. They find that for an applied field strength $||\mathbf{H}||$, the optimal field angle θ_{opt} is given by

$$\theta_{\text{opt}} = \begin{cases} 45^\circ, & ||\mathbf{H}|| \leq ||\mathbf{H}||_{\text{low}} \\ \arctan\left(\frac{n_r}{n_a}\sqrt{\frac{||\mathbf{H}||^2 - m_s^2 n_a^2}{m_s^2 n_r^2 - ||\mathbf{H}||^2}}\right), & ||\mathbf{H}||_{\text{low}} \leq ||\mathbf{H}|| \leq ||\mathbf{H}||_{\text{high}} \\ \arcsin\left(\frac{(n_r - n_a)m_s}{2||\mathbf{H}||}\right) + 45^\circ, & ||\mathbf{H}||_{\text{high}} \leq ||\mathbf{H}|| \end{cases} \tag{3.10}$$

where n_a and n_r are the axial and radial demagnetizing factors (see section 2.6), and the limit field $||\mathbf{H}||_{\text{low}}$ and $||\mathbf{H}||_{\text{high}}$ are given by

$$||\mathbf{H}||_{\text{low}} = \frac{m_s n_a n_r \sqrt{2}}{\sqrt{n_a^2 + n_r^2}} \tag{3.11}$$

$$||\mathbf{H}||_{\text{high}} = m_s\sqrt{\frac{n_a^2 + n_r^2}{2}} \tag{3.12}$$

Furthermore, they find that the torque on a soft-magnetic body has an upper limit, independent of the applied field strength, given by

$$||\mathbf{T}||_{\text{max}} = \frac{\mu_0 V(n_r - n_a)m_s^2}{2} \tag{3.13}$$

3.2.3 Torque Analysis using Lagrange multiplier

Based on Section 2.9, the non-dimensional magnetization $\mathbf{x} = \mathbf{M}/m_s$ can be expressed as (2.59)

$$\mathbf{x} = (\mathbf{N} + \lambda \mathbf{I})^{-1} \mathbf{b}. \tag{3.14}$$

With $\mathbf{b} = b\,\mathbf{e}_\mathrm{b} + b_c \mathbf{e}_\mathrm{bc}$, non-dimensionalizing the torque expression (3.5) yields

$$\boldsymbol{\tau} = \frac{\mathbf{T}}{\mu_0 V m_s^2} = b^2 (\mathbf{N} + \lambda \mathbf{I})^{-1} \left(\mathbf{e}_\mathrm{b} + \frac{b_c}{b} \mathbf{e}_\mathrm{bc} \right) \times \mathbf{e}_\mathrm{b}. \tag{3.15}$$

This expression is now equivalent for any body described by $\mathbf{N}$. Because of the vanishing z-component of $\mathbf{H}$ in (3.7) the resulting cross product has only an entry in the z-direction. For $b_c = 0$, it is given by

$$\tau_z = \frac{1}{2} \frac{n_y - n_x}{(n_x + \lambda)(n_y + \lambda)} b^2 \sin(2\theta) \tag{3.16}$$

For $\lambda = 0$, we obtain the standard result for the linear region, that is, a quadratic behavior in the applied field strength b and a $\sin(2\theta)$ behavior which has a maximum at $\theta = 45°$. Furthermore, for a symmetric shape in the $x - y$ plane no torque is obtained, since in that case $n_x = n_y$ (assuming uniform magnetization). For $\lambda > 0$, the shape of the curve is more complex since $\lambda = \lambda(b, \theta)$.

Furthermore, we observe that the maximal torque that can be exerted on the body in the limit of large $\lambda \approx b$ is given by

$$\tau_{z,\max} = \frac{1}{2}(n_y - n_x), \tag{3.17}$$

then λ dominates the denominator of (3.16) and approaches b. Note that (3.17) is the non-dimensional form of the maximal torque (3.13) derived by Abbott et al. [2007].

We can further analyze the torque curve as follows. The ratio τ_R of the torque τ_z to its maximal value is found as

$$\tau_R := \frac{\tau_z}{\tau_{z,\max}} = \frac{b^2 \sin(2\theta)}{(n_x + \lambda)(n_y + \lambda)}. \tag{3.18}$$

We see that in the limit of large fields, when $\lambda \approx b$, τ_R approaches $\sin(2\theta)$ asymptotically. This shows that the maximal torque in the large field limit is again obtained for $\theta = 45°$, which is again a standard result (see (3.10)). However, it follows naturally from our description, without typical assumptions, e.g. that $\mathbf{M}$ and $\mathbf{H}$ are parallel[2]. Furthermore, the total differential $\mathrm{d}\tau_R$ shows the evolution of the torque after saturation has been reached ($\lambda > 0$). Assuming $\lambda \approx b$ we have

$$\mathrm{d}\tau_R = \frac{\partial \tau_R}{\partial b} \mathrm{d}b + \frac{\partial \tau_R}{\partial \theta} \mathrm{d}\theta. \tag{3.19}$$

[2]These assumptions are also not made by Abbott et al. [2007]. Rather, the optimal angle for the maximal torque is calculated by inverting the magnetization model.

We then find

$$\mathrm{d}\tau_R = \frac{b^2(n_x+n_y)+2bn_xn_y}{\left(b^2+b(n_x+n_y)+n_xn_y\right)^2}\sin(2\theta)\mathrm{d}b+ \tag{3.20}$$

$$+\frac{2b^2}{b^2+b(n_x+n_y)+n_xn_y}\cos(2\theta)\mathrm{d}\theta. \tag{3.21}$$

Now, the first term in the sum is always positive (for typical values for $\theta \in (0°, 90°)$). However, the second term changes sign at $\theta = 45°$. Thus, for angles $\theta \leq 45°$, the torque is monotonically increasing and reaches its limit without reaching a maximal value. For angles $\theta > 45°$, the second term eventually dominates, as its numerator has similar behavior and its denominator is smaller. Thus, for these angles the torque first may increase and reach a maximum, eventually even the absolute maximum value $\tau_R = 1$, and then decreases and approaches its limit. The fact that the curve may increase or decrease after saturation for certain angles has been also described qualitatively by Abbott et al. [2007] by observation of their numerical results. Yet, no predictions on when this is the case could be made, except in terms of the angle for the maximal torque (3.10). From our model we can conclude that increasing the field will always increase the torque as long as $\theta < 45°$.

Next, our description also allows for the derivation of the minimal torque on a structure, and, hence provides a design criteria. Of course, for $\theta = 0°$ or $\theta = 90°$ the torque vanishes. Yet, for θ different from these values, we note that the maximal possible value for λ is given by its upper boundary from (2.78) as

$$\lambda_{\max} = \max(0, b - n_{\min}) \tag{3.22}$$

$$= \max(0, b - n_x) \tag{3.23}$$

Substituting $\lambda_{\max}$ in (3.16) yields the minimal torque as

$$\tau_{z,\min} = \frac{1}{2}\frac{n_y - n_x}{(n_x+\lambda_{\max})(n_y+\lambda_{\max})}b^2\sin(2\theta) \tag{3.24}$$

$$= \begin{cases} \frac{1}{2}\frac{n_y-n_x}{n_xn_y}b^2\sin(2\theta), & \lambda_{\max} = 0 \\ \frac{1}{2}\frac{n_y-n_x}{b+n_y-n_x}b\sin(2\theta), & \lambda_{\max} = b - n_x. \end{cases} \tag{3.25}$$

and the ratio of the extremal values is

$$\frac{\tau_{z,\min}}{\tau_{z,\max}} = \min\left(\frac{b^2\sin(2\theta)}{n_xn_y}, \frac{b\sin(2\theta)}{b-n_x+n_y}\right) \tag{3.26}$$

which basically shows the range of the torque that can be applied to the sample for a given angle θ and field strength b.

Figure 3.18 illustrates these findings for $\theta = 15°$ and $75°$ and different n_y/n_x ratios representing the change of shape. The n_y/n_x ratio approximately represents the aspect ratio of the body, thus larger ratios represent thin long shapes in the $x-y$ plane, violating our assumption of $n_x <$

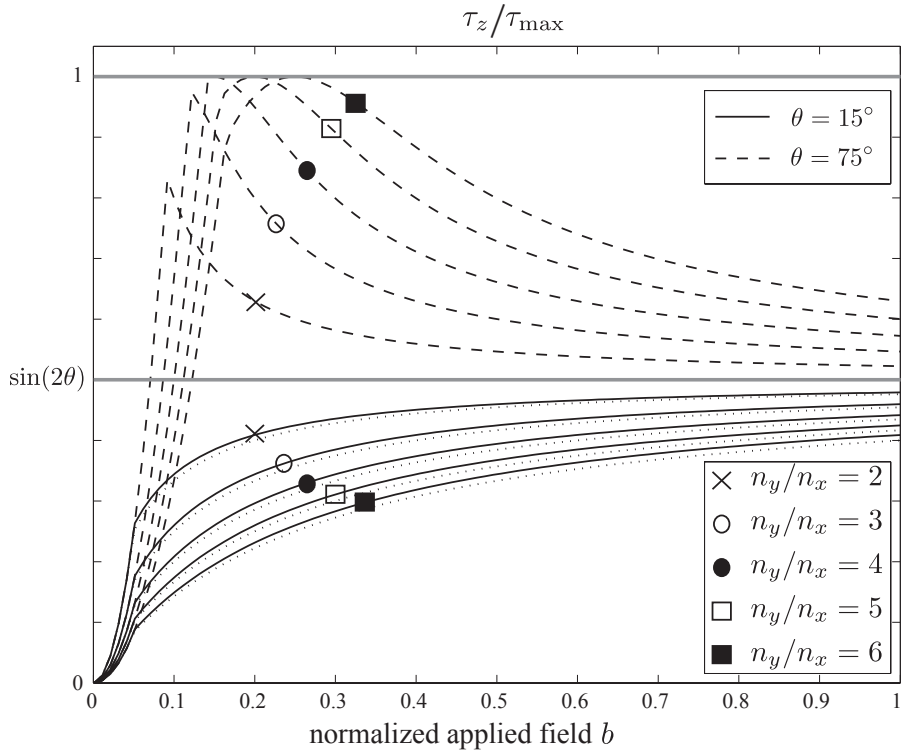

Figure 3.2: Torque ratio $\tau_z/\tau_{\max}$ vs. applied field strength for two applied field angles θ and different n_y/n_x ratios. We see the quadratic increase for sufficiently low fields, and the asymptotic beheavior towards $\sin(2\theta)$ for high fields. The influence of increasing n_y/n_x, thus shape, is to decrease the torque for small angles, while increasing it for larger angles. The dotted lines represent the minimal achievable torque for the given field/angle configuration.

$n_y < n_z$ for the sake of generality. Note, that the figure is completely non-dimensional, thus representing a general torque curve.

We also observe the asymptotic approach of the limit, in both cases $\sin(2\theta) = 1/2$. For $\theta = 15°$, the torque increases monotonically to this limit. For $\theta = 75°$, the torque decreases immediately after saturation for $n_y/n_x = 2$ and 3 without reaching the maximum. For $n_y/n_y \geq 4$ the torque further increases after saturation, reaches its maximal value, then decreases asymptotically towards its limit. The dotted lines represent the respective minimal values that were derived. They are identical for both angles.

As for the influence of shape, we observe that at small angles, larger aspect ratios decrease the torque while increasing it for large aspect ratios. However, this change is rather small for small angles, thus making the torque rather insensitive to even large changes in the aspect ratio. For large angles a change in the aspect ratio may lead to significant changes in the resulting torque. This, again, can be used as a design guideline for wireless magnetic

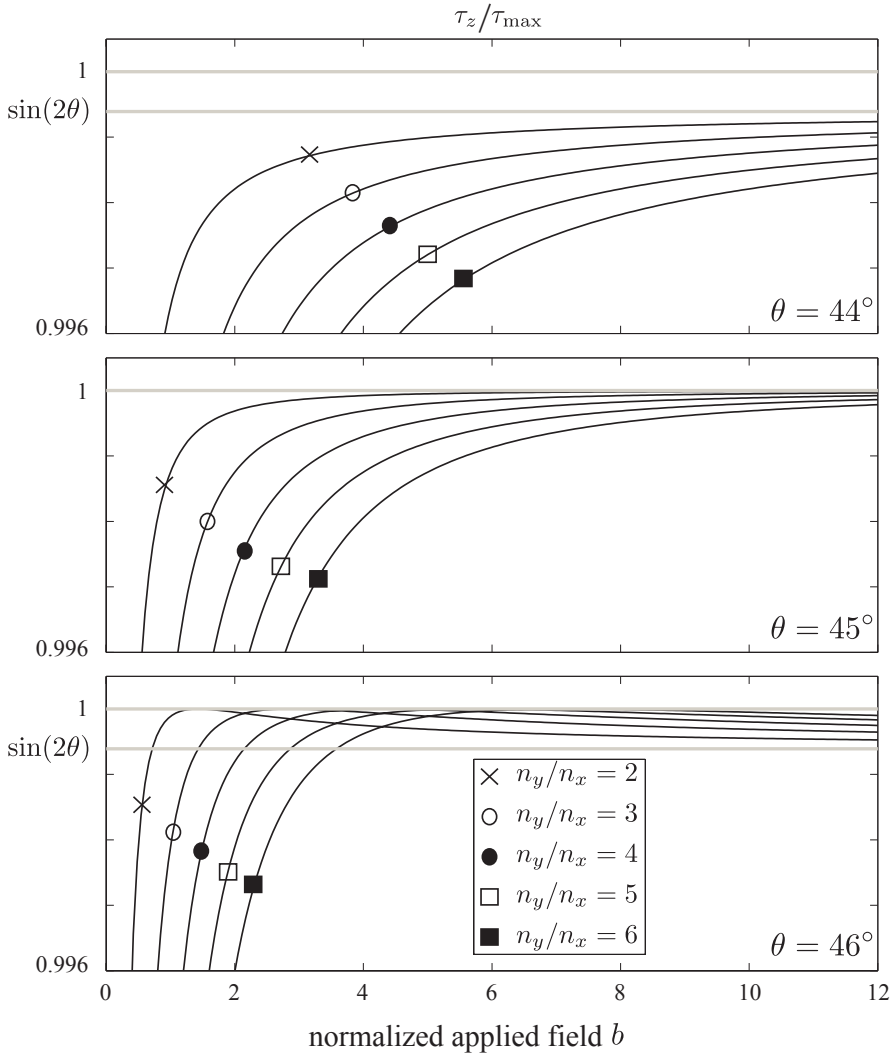

Figure 3.3: Numerical illustration that torques for $\theta < 45°$ are increasing monotonically to their limit, while for $\theta > 45°$ the torques may attain a maximum and decrease afterwards. For $\theta = 45°$ the limit and the maximum are identical and reached asymptotically.

manipulation systems.

Figure 3.3 shows torque curves for $\theta = 44°, 45°$ and $\theta = 46°$ for different aspect ratios. This illustrates numerically what we discussed above (see (3.21)): for $\theta = 44°$, the torque curve increases monotonically and approaches its limit asymptotically; for $\theta = 46°$, the maximum value is reached before decreasing to the limit; for $\theta = 45°$, the limit and the maximum are identical and reached asymptotically.

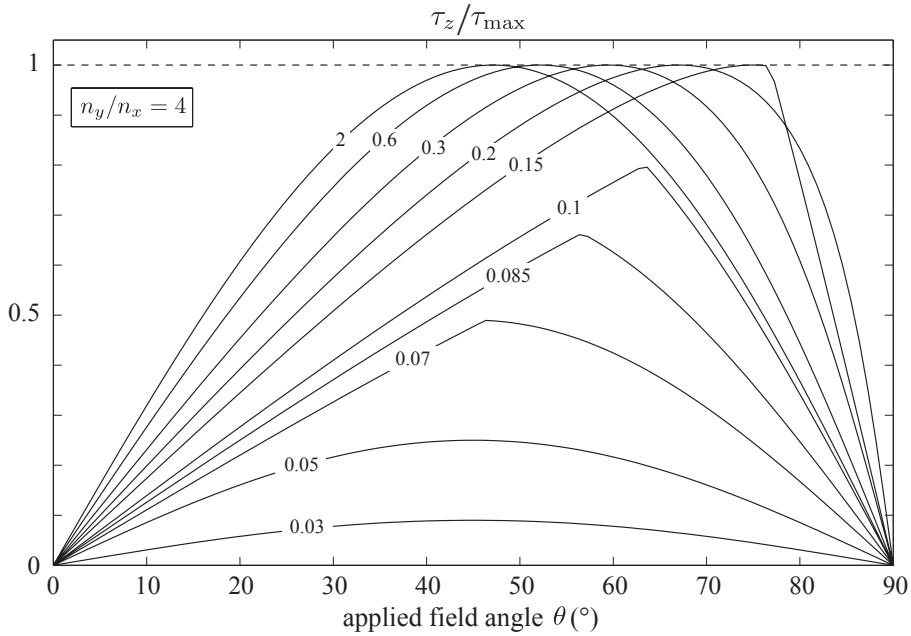

Figure 3.4: $\tau_z/\tau_{\max}$ as a function of the applied field angle θ for $n_x = 0.05$, and $n_y = 0.2$. The numbers in the curves signify the normalized field strength b. We identify a $\sin(2\theta)$ behavior for low and high fields with a maximum at 45°. In between, until about $b = 0.2$ torques curves approach a $\sin\theta$ behavior, indicating that the part behaves more like a permanent magnet with fixed magnetization.

Finally, Fig. 3.4 shows the torque vs. angle curves for $n_x = 0.05$ and $n_y/n_x = 4$ and different applied field magnitudes. We can identify the $\sin(2\theta)$ behavior at low and high fields. In the intermediate values, until approximately $b < n_y = 0.2$, thus until the piece is fully saturated, the curves approach a $\sin\theta$ behavior. This indicates that the part behaves more like a permanent magnet with fixed magnetization $\mathbf{M}$.

To summarize, using our description of the magnetization we derived a torque expression using λ. This is a generalization of the standard available results. The standard results can be obtained by observing the limits of our model. Thus, we can accurately predict the limit behavior of the torque, and, in addition, examine its evolution towards these limits. We show that the torque increases or decreases after saturation depending on the applied field angle, and that for small angles the torque is insensitive to even large changes in aspect ratio. Our magnetization description predicts the minimal torque on a magnetic body, thus characterizing and assessing designs for their suitability for specific tasks.

Remark 3.2. *Recall that in all our derivations uniform magnetization of the sample is assumed. Particularly for low fields and for shapes different from ellipsoids, this is wrong. The actual magnetization of the sample is a vector field, as introduced*

in Section 2.4.2, having a mean direction over the volume of the sample. Because of this, assuming uniformity overestimates the actual magnetization of the sample. Consequently, the torque is overestimated.

3.2.4 Finite Element Analysis

To verify our results, we perform numerical simulations using the commercial finite element software Maxwell3D-V13[3]. For this, the shapes are placed inside a large rectangular box under vacuum ($\mu_r = 1$). The dimension of the box is $5 \times 4 \times 3\text{mm}^3$. The magnetization is modeled using a Langevin curve (see Section 2.7) with the respective parameters being given for each case. The applied magnetic field represents the boundary conditions on the outer faces of the box.

For the simulations, Maxwell employs an adaptive mesher algorithm using tetrahedral mesh elements, and increases their number in critical regions by 30%. Typically 15-30000 tetrahedrons are generated until the simulation converges for an energy criteria. This criteria is either that the energy error is less then 0.01% or 0.001% set by observing manually the evolution, or the maximal number of iterations, set to 10 or 15, has been reached. The energy criteria employed by Maxwell in the magnetostatic case is to compute $\nabla \times \mathbf{H}$ in the entire domain and compare it zero, since Maxwell's equation (2.5) must hold with $\mathbf{J} = \mathbf{0}$.

3.3 Superposition of Soft-Magnetic Shapes

When two soft-magnetic shapes are placed close to each other in an applied magnetic field, the field produced by their magnetization may alter the effective applied field, and thus the resulting mutual magnetization will be different from the value calculated using the methods in Section 2.5 or 2.9. Three scenarios for the analysis can be identified:

1. We can neglect the interaction and compute the total torque by the sum of the individual torques.

2. One, or a few, shapes dominate the torque on the structure and the computation can be simplified by computing the magnetization/torque only on the the dominant structure.

3. Interaction of all parts must be considered.

No analytical methods exist to consider interacting parts. However, here we show that interactions only occur in very specific cases. We note that when the applied field is sufficiently high, saturation occurs and the susceptibility of the samples drops to zero. Thus, their mutual effect can be neglected. For intermediate and low applied fields, the magnetic field produced by the shapes due to their magnetization typically drops with the distance cubed or even with the fifth power (see Section 2.3). Thus, after a few, typically less

[3]www.ansoft.com

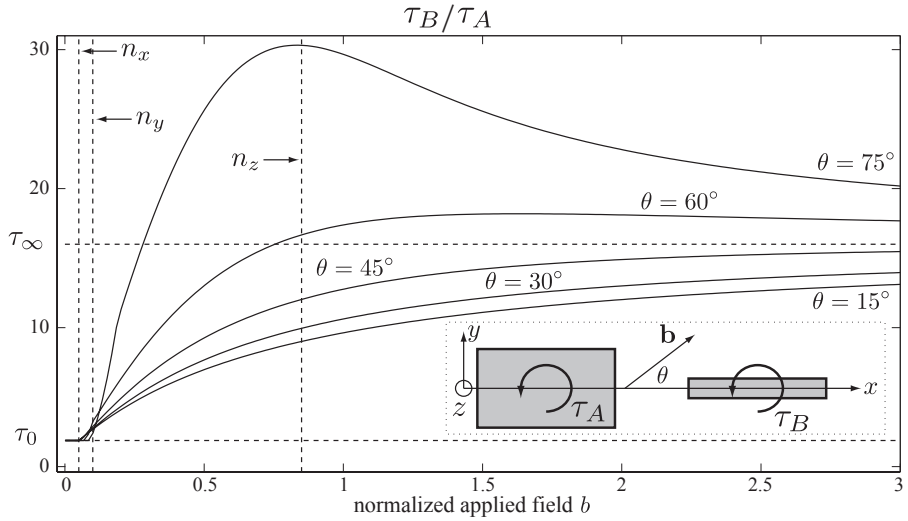

Figure 3.5: Torque ratio for two parallel shapes with $n_x = 0.05$, $n_y = 0.1$ and $n_z = 0.85$ rotated by 90° around their common x-axis. Clearly, the torque on the shape perpendicular to the applied field is larger, since $\tau_B/\tau_A > \tau_0 \approx 1.9$ (see text).

than 3 to 4 body lengths, their interaction can be neglected, as well.

From this, it is clear that interaction has to be considered only for moderate and low applied fields, when structures are displaced less than 3 or 4 body-lengths. The method of choice is typically finite element software. For other configurations we can either compute the sum of the individual torques, or consider an equivalent shape with the same overall geometry. This covers scenarios 1 and 3.

For scenario 2, we now turn to investigate configurations that may exhibit dominant structures.

3.3.1 The Effect of Orientation

Consider two identical shapes A and B with $n_x < n_y < n_z$. We are interested in the ratio of their torques τ_A and τ_B. Since, the torque depends on the magnetization, and the magnetization on the field strength and direction, the orientation of the shapes significantly influences the torque ratio. We will examine two special cases.

First, consider the shapes placed perpendicular to each other such that their x axis coincides, i.e., the $x-y$ plane of A is in the plane of the applied field, while the $x-y$ plane of B is perpendicular to it (see inset in Fig. 3.5).

Then, using (3.16), the ratio of the torques τ_B and τ_A is found as

$$\frac{\tau_B}{\tau_A} = \frac{n_z - n_x}{n_y - n_x} \cdot \frac{(n_x + \lambda_A)(n_y + \lambda_A)}{(n_x + \lambda_B)(n_y + \lambda_B)} \tag{3.27}$$

$$= \frac{n_z - n_x}{n_y - n_x} \cdot \frac{n_x n_y + \lambda_A(n_x + n_y) + \lambda_A^2}{n_x n_z + \lambda_B(n_x + n_z) + \lambda_B^2} \tag{3.28}$$

for $\theta \neq 0, 90^\circ$. We observe that in the limit of large fields ($\lambda_A \approx \lambda_B \gg 0$), we have

$$\frac{\tau_B}{\tau_A} = \frac{n_z - n_x}{n_y - n_x} =: \tau_\infty, \tag{3.29}$$

while in the linear limit ($\lambda_A = \lambda_B = 0$) the ratio of the torques simplifies to

$$\frac{\tau_B}{\tau_A} = \frac{n_z - n_x}{n_y - n_x} \cdot \frac{n_x n_y}{n_x n_z} = \frac{n_z - n_x}{n_y - n_x} \cdot \frac{n_y}{n_z} = \frac{n_y}{n_z}\tau_\infty =: \tau_0 \tag{3.30}$$

With typical values of $n_x = 0.05$, $n_y = 0.1$ and $n_z = 0.85$, we have $\tau_0 \approx 1.9$ and $\tau_\infty \approx 16$. This means that for both of these limit cases, the torque on the plate perpendicular to the applied field is significantly larger than the torque on the plate that lies parallel to the field. These results can be also derived classically.

However, our description allows further insight. For sufficiently low applied fields, λ_B will be zero, while λ_A is already positive. Thus, the torque ratio increases quadratically with λ_A. Increasing the field will further increase λ_A and, thus, increase the torque ratio. However it will also eventually turn λ_B positive and start increasing the denominator of (3.28), thus decreasing the torque ratio. This indicates the possibility of an optimal field strength/direction that results in the largest torque ratio between the two samples.

This is shown in Figure 3.5. Clearly, the plate perpendicular to the applied field has a larger torque, since $\tau_B/\tau_A > \tau_0 \approx 1.9$. We also observe how the torque ratio tends towards its high field limit τ_∞. But also, as predicted by our model, much higher values are possible before. We also recall, that for $\theta < 45^\circ$ we found that the torque on a single shape increases monotonically, while for $\theta > 45^\circ$, it may attain a maximum before decreasing to its limit.

To summarize, it is expected that such configurations will dominate the torques on combined structures. Also, as argued in the previous section, this shows that we need only consider the dominant shapes and can neglect the non-dominant ones to obtain a good estimate for the torque.

Now assume both shapes are perpendicular to applied field such that the field is applied in their $x - z$ plane, and B is rotated by 90° along their common y axis ('cross' configuration, see inset in Fig 3.6). In the frame of A, the field has an angle θ, while for B it is $-90^\circ + \theta$. Thus, the ratio of the sin terms in the torque (3.16) is $\sin(2\theta)/\sin(-180^\circ + 2\theta) = -1$, and the resulting torque ratio is

$$\frac{\tau_B}{\tau_A} = -\frac{n_x n_z + \lambda_A(n_x + n_z) + \lambda_A^2}{n_x n_z + \lambda_B(n_x + n_z) + \lambda_B^2}. \tag{3.31}$$

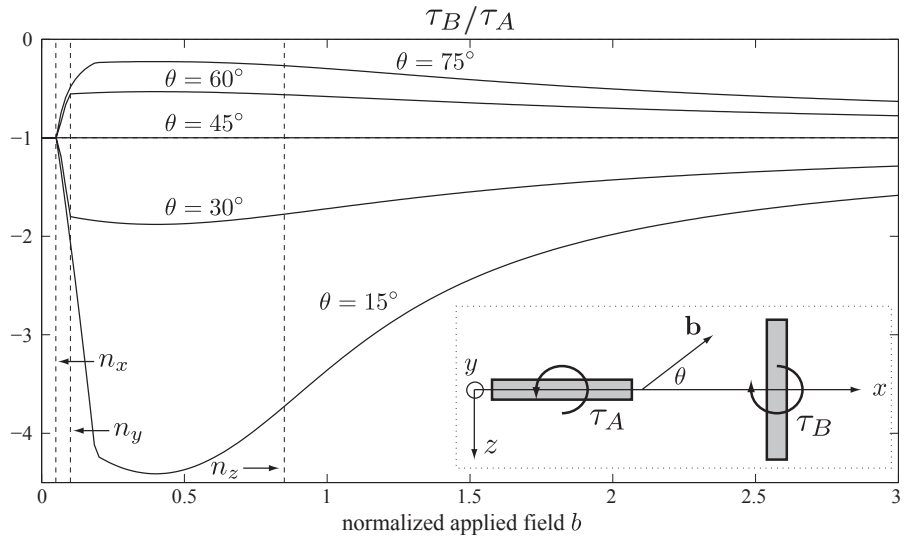

Figure 3.6: Torque ratio for the 'cross' configuration. For the low and high field limits and for $\theta = 45°$, the torque on both shapes is equal and opposed as $\tau_B/\tau_A = -1$. However, we observe dominance of shape B for angles $< 45°$ and A for angles $> 45°$.

We observe that $\tau_B/\tau_A = -1$ in both, the linear ($\lambda_A = \lambda_B = 0$) and the high field limit (both $\lambda \gg 0$), meaning that the torque is exactly opposed on both samples. In addition, it is also -1 when $\lambda_A = \lambda_B \neq 0$ which occurs for an applied field angle of 45° due to symmetry.

Again, these could have been derived with the classical description leading to the wrong conclusion that no net torque can be applied to the assembled structure, as the total torque would vanish for every case ($\tau_A + \tau_B = \tau_A - \tau_A = 0$). Yet, our description shows that for $\lambda_A \neq \lambda_B > 0$, a torque ratio different from -1, and hence a non-zero net torque on the assembled structure could be obtained.

The torque ratio is plotted in Fig 3.6. We observe that B is dominant for small θ, and it follows from symmetry that A will be dominant for θ close to 90°. Since their interaction is exactly opposed for $\theta = 45°$, we expect maximal effect of the interaction between 0° and 45° and examine this further using experiments.

3.3.2 The Effect of Material

The torque ratio (3.28) assumes both samples with the same aspect ratio and, thus, volume, made from the same material. If this is not the case, i.e., if the the samples have different saturation magnetizations $m_{s,A}$ and $m_{s,B}$ respec-

tively, (3.28) has to be modified accordingly as

$$\frac{\tau_B}{\tau_A} = \frac{m_{s,B}^2}{m_{s,A}^2} \cdot \frac{n_z - n_x}{n_y - n_x} \cdot \frac{n_x n_y + \lambda_A(n_x + n_y) + \lambda_A^2}{n_x n_z + \lambda_B(n_x + n_z) + \lambda_B^2} \tag{3.32}$$

and we see that we can scale the torque ratio significantly by choosing the appropriate materials. This also applies to the ratio (3.31).

3.3.3 Doubling one Dimension

For simplifying the computation in the case of superposition, we consider the case when the two shapes are placed in parallel, and, thus, no shape dominates the interaction. As an instructive example we compare the torque τ_S on a single shape S ('single') to the torque τ_D on a shape D ('double') that doubles the dimension in the shortest direction. Assuming the field applied in the $(x-z)$ plane, the ratio of the torques is given by

$$\frac{\tau_D}{\tau_S} = 2 \cdot \frac{n_{zD} - n_{xD}}{n_{zS} - n_{xS}} \cdot \frac{(n_{xS} + \lambda_S)(n_{zS} + \lambda_S)}{(n_{xD} + \lambda_D)(n_{zD} + \lambda_D)} \tag{3.33}$$

where the factor 2 accounts for the volume difference, and the subscripts S and D designate the variables for the single and the double shape, respectively. We can identify a lower limit for sufficiently low fields, thus $\lambda_S = \lambda_D = 0$, as

$$\left(\frac{\tau_D}{\tau_S}\right)_{\min} = 2 \cdot \frac{n_{zD} - n_{xD}}{n_{zS} - n_{xS}} \cdot \frac{n_{xS} n_{zS}}{n_{xD} n_{zD}} \tag{3.34}$$

and a limit for sufficiently high fields as

$$\left(\frac{\tau_D}{\tau_S}\right)_{\infty} = 2\frac{n_{zD} - n_{xD}}{n_{zS} - n_{xS}}. \tag{3.35}$$

There is no straightforward mapping between the demagnetizing factors n_{iS} and n_{iD}. To obtain an estimate, we use the procedures from Beleggia et al. [2006] to numerically compute n_{iS} for thin rectangular plates of sizes (L_x, L_y, L_z) and, similarly, for plates with double thickness $(L_x, L_y, 2L_z)$. We consider a total of 100 aspect ratios $L_y/L_x \in (0.1, 1)$ and 100 ratios $L_z/L_x \in (0.01, 0.1)$, resulting in a total of 10000 configurations. The results are shown in Fig 3.7, together with the fits for $n_{iD} = n_{iD}(n_{iS})$. Excellent fits are found using MATLAB's `fit` function with the polynomial models, a linear one for n_x and quadratic ones for both n_y and n_z as

$$n_{xD} = 1.525 n_{xS} + 0.0026 \qquad \text{RMSE} = 0.003 \tag{3.36}$$

$$n_{yD} = -0.797 n_{yS}^2 + 1.66 n_{yS} + 0.0022 \qquad \text{RMSE} = 0.002 \tag{3.37}$$

$$n_{zD} = 0.8495 n_{zS}^2 + 0.025 n_{zS} + 0.123 \qquad \text{RMSE} = 0.0003 \tag{3.38}$$

where RMSE designates the root mean square error of the fit.

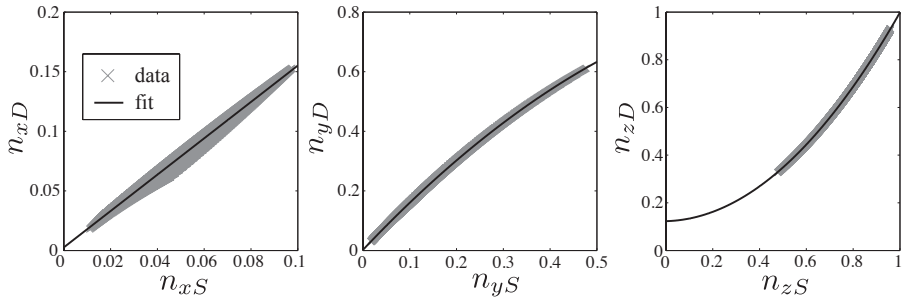

Figure 3.7: Numerical fit of the demagnetizing factors n_{iS} for thin rectangular plates of sizes (L_x, L_y, L_z) and with those for for plates with double thickness n_{iD}, thus size $(L_x, L_y, 2L_z)$.

With these relationships, the ratio (3.33) has been calculated for $n_{xS} = 0.05$ and $n_{zS} = 0.85$ and is shown in Figure 3.8, together with the minimal and limit values

$$\left(\frac{\tau_D}{\tau_S}\right)_{\min} = 1.207, \quad \text{and} \quad \left(\frac{\tau_D}{\tau_S}\right)_{\infty} = 1.705 \tag{3.39}$$

We can observe an interesting result: even though the high field limit value is 1.7, after saturation, the torque ratio is approximately 2, meaning that the torque on the plate with double thickness is twice the torque on the single plate. Conversely, in saturation, we can approximate the torque on two, parallel non-interacting plates with the torque on a single plate with double thickness, i.e. $\tau_D \approx 2\tau_S$. Before saturation, no such simplification is possible.

3.4 Verification

3.4.1 Ellipsoid

For the prolate ellipsoid introduced in Section 2.10 (Fig. 2.7(a)), we show the results for the torque from Abbott et al. [2007] in Fig. 3.9(a). As expected, the data is well predicted by the model. The sharp corners in the model, due to the sharp transition from linear to saturated behavior are smoothed by the data. In Fig. 3.9(b), we show the effect of calculating the torque using the approximation λ_β. We see that the transition from linear to the saturated behavior is well predicted. The approximation is also very good for small angles. However, for larger angles, especially those where the slope of the curve changes sign ($\theta = 55^\circ$ and 70°), the error can increase significantly with the applied field.

3.4.2 Planar Shapes

We now investigate the case with more extreme aspect ratios, i.e., thin planar shapes. Following Beleggia et al. [2006], an elliptical plate with aspect ratios $l_a = a_y/a_x$, and $l_t = t/(2a_x)$, where a_x and a_y are the semi-axes in x and y directions, respectively, and t is the thickness, has a magnetically equivalent

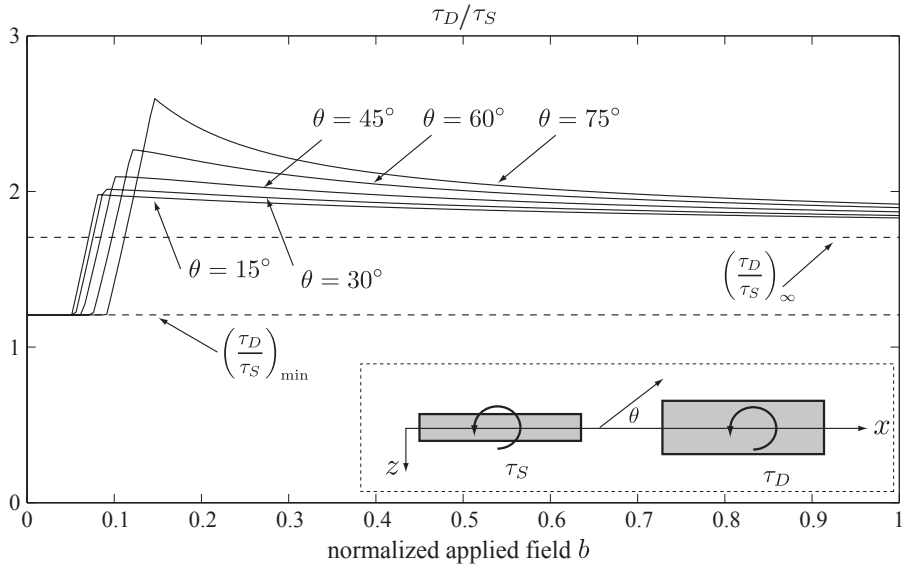

Figure 3.8: Torque ratio τ_D/τ_S relating the torque on a single plate to the torque on the same plate with double thickness. We see that in saturation the $2\tau_S$ is a good approximation of τ_D.

ellipsoid with aspect ratio $l_x = a'_z/a'_x$ and $l_y = a'_z/a'_y$ where a'_x, a'_y and a'_z are the semi-axes of the ellipsoid in the respective directions. They provide the numerical procedures to determine this equivalent ellipsoid. What is important, is that both shapes have the same demagnetizing factor, and, therefore, should theoretically show the same non-dimensional torque behavior.

To investigate this, we calculated using FEM the torque on a thin elliptical plate with $l_a = 0.5$ and $l_t = 0.025$. The corresponding ellipsoid has aspect ratios $l_x = 0.047$ and $l_y = 0.090$, resulting in demagnetizing factors $n_x = 0.027$, $n_y = 0.073$ and $n_z = 0.90$ for both cases. For the magnetization, we use a Langevin curve with $m_s = 5 \times 10^5$A/m and $\chi = 10000$ to enforce shape dominance.

The results are shown in Fig. 3.10 for $\theta = 15°$ and $75°$ together with the analytical results. We see that the analytical model generally predicts the behavior of the torque curves, especially for the small angle $\theta = 15°$, and for both angles when the field is applied in the $(x-z)$ plane of the piece (bottom figure).

When the field is applied in the $(x-y)$ plane of the shape (top figure), we observe the largest discrepancy in the transition from the intermediate to the fully saturated region (around n_y) for $\theta = 75°$. For the ellipsoid, we see a shift of the peak. The shift is due to the difference in the magnetization curves: the Langevin curve models a smaller magnetization and a larger transition region. For the elliptical plate, the peak disappears in the FE results and is smoothed. Besides to the difference in the magnetization, this is mostly due

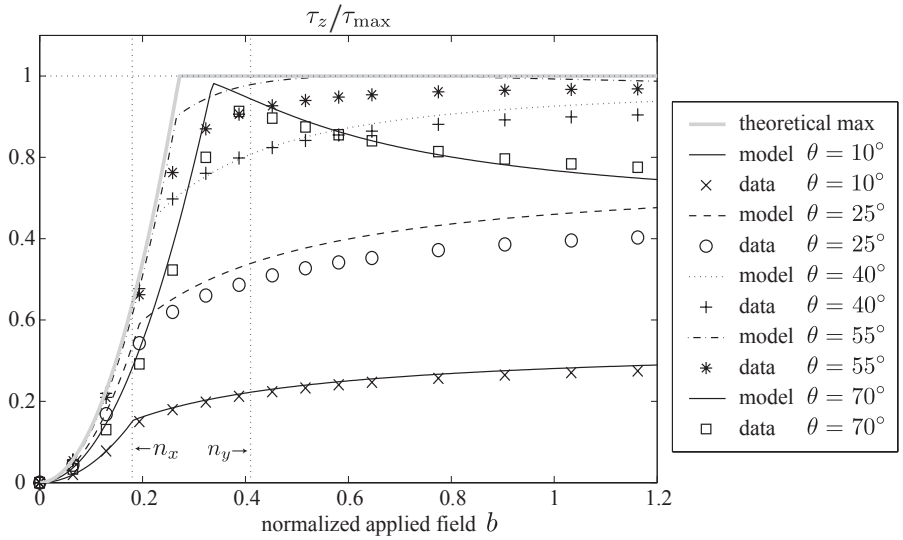

(a) As expected, the data is predicted very well by the model.

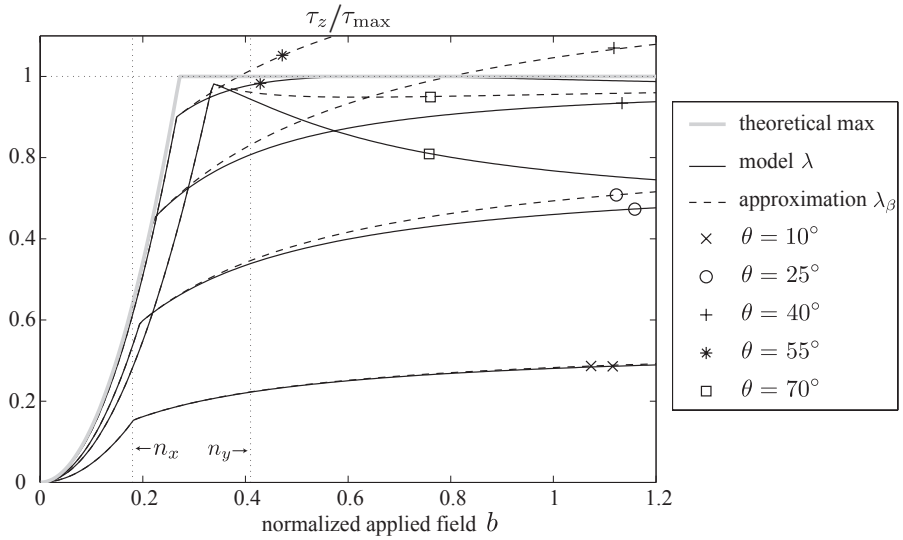

(b) Using approximation λ_β predicts the transition from the linear to the saturated behavior well. For small angles, the entire range is predicted well. For larger angles, the error may be significant as the slope at the transition is maintained.

Figure 3.9: (a) Torque results for a prolate ellipsoid with $n_x = 0.18$ and $n_y = 0.41$ from Abbott et al. [2007]. (b) Error on the torque due to the approximation λ_β.

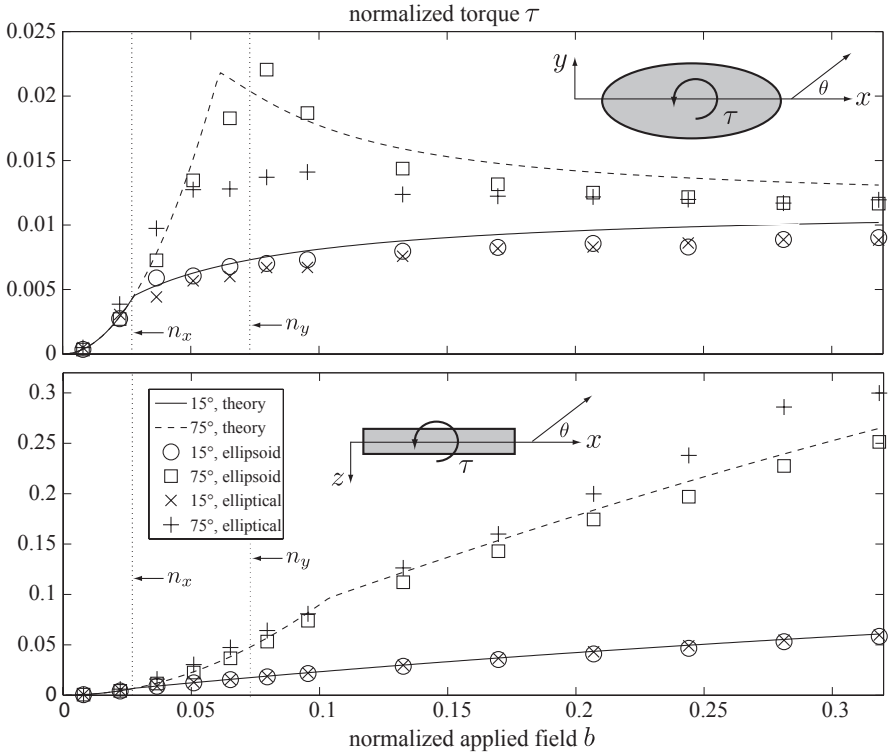

Figure 3.10: Theoretical torque curves (lines) compared to FEM results (markers) for an ellipsoid and an elliptical thin plate having the same demagnetizing factors $n_x = 0.027$, $n_y = 0.073$ and $n_z = 0.90$. See text for discussion.

to the assumption of uniform magnetization.

In general, the differences are within 10%, which is within acceptable limits for verification.

3.4.3 Superposition

Now we verify our previous argumentation on superposition. We have seen in Section 3.3.1 that configurations with dominant shapes may exist. To avoid this, and to ensure that both pieces contribute equally to the combined structure, we have to consider a parallel arrangement as shown in the inset of Fig. 3.11 for two thin elliptical plates with $l_a = 0.5$ and $l_t = 0.025$. Using FEM, we calculate the total torque on the structure, again for $\theta = 15°$ and $75°$. The distance d between the two plates varies from 0.5 to 8 times the thickness t of the plates.

The FE results for the torque, τ_{FEM}, for $\theta = 15°$ and $75°$ are shown in Fig. 3.11 normalized with the torque on a single plate τ_S. For both angles, we see that after saturation ($b > 0.025$ for $\theta = 15°$ and $b > 0.1$ for $\theta = 75°$) the ratio τ_{FEM}/τ_S is approximately 2, confirming that superposition can be used

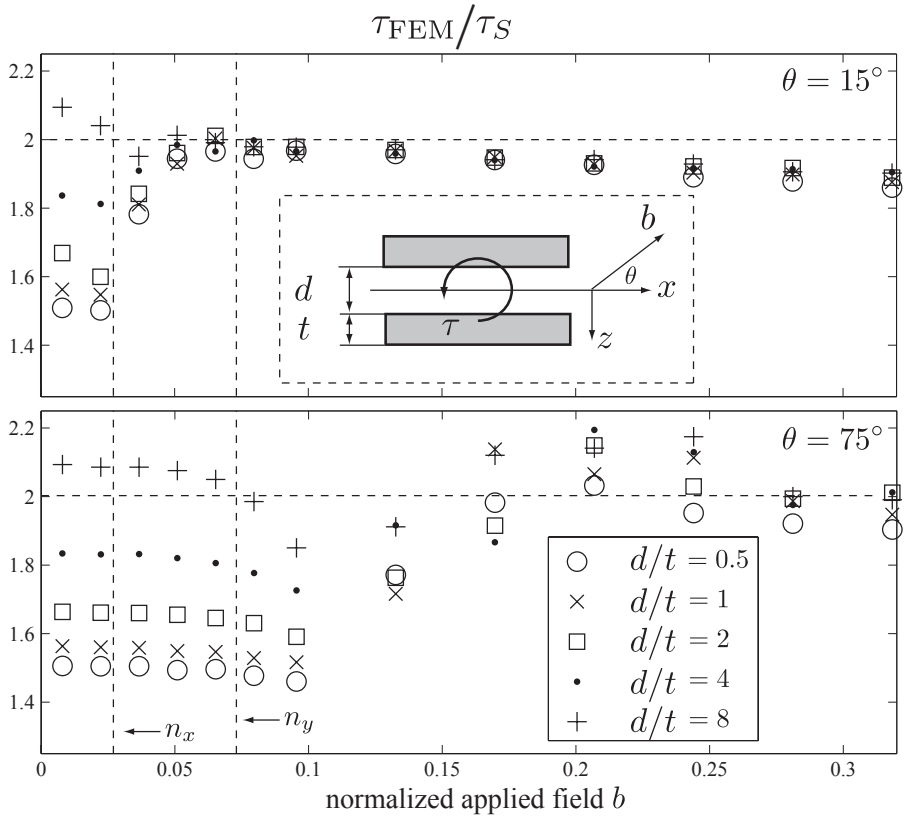

Figure 3.11: Torque on two parallel thin plates calculated by FEM, τ_{FEM}, normalized with the theoretical torque on a single plate, τ_S, as a function of the distance between the plates. Below saturation, interaction can be observed when the plates are closer than a few body-lengths. When they are farther, or when the applied field is higher than the saturation field, superposition holds as $\tau_{\mathrm{FEM}} \approx 2\tau_S$.

to approximate the total torque, i.e. $\tau_{\mathrm{FEM}} \approx 2\tau_S$. Note that the limits of saturation are given in terms of the individual piece, not the combined structure.

Before saturation, we observe that for $d/t = 0.5$, i.e., when the plates are very close, the torque ratio is about 1.5 and increases with increasing d/t up to > 1.8 for $d/t \geq 4$. Thus, also for low fields, superposition holds when the plates are sufficiently far away from each other, e.g., 3 to 4 body-lengths. This confirms our argumentation from Section 3.3.

3.4.4 Experimental: Microrobot

For the experimental investigation we consider the the microrobot assembled from elliptical nickel parts as shown in Fig. 3.1. The fabrication process is described in detail by Yesin et al. [2006].

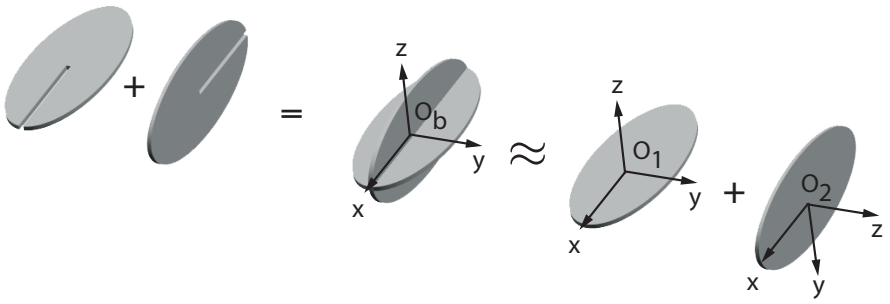

Figure 3.12: Microfabricated nickel parts (left) are assembled to form a microrobot (middle). Rather than using the actual complex shapes of the parts for the computation, we consider the microrobot as a superposition of simpler geometries (right). The frames of the individual parts are assigned with the x-axis along the longest dimension of the body and with the z-axis along the shortest dimension. The body frame coincides with part 1.

We are interested in the torque on the assembled structure and investigate two situations. In the first, the fields are applied in the xy-plane and the torque around the z-axis is measured. We expect the out-of plane part to be dominant as shown in Section 3.3.1. In the second, the fields are applied in the yz-plane and the torque around the x-axis is measured. This is the 'cross' configuration analyzed in Section 3.3.1.

We assign a body frame and the individual component frames as shown in Fig. 3.12. In our simplifying model, we consider two elliptical parts with semi axes 1mm, and 0.5mm and thickness 42µm, resulting in the demagnetizing factors $n_x = 0.02439$, $n_y = 0.06405$ and $n_z = 0.9115$.

Magnetization data was then collected for the individual shape with a MicroMag 3900 vibrating-sample magnetometer (VSM) from Princeton Measurements Corp. Figure 3.13 shows the magnetization along the x and y axes plotted against the applied field. Using the demagnetizing values for the specific directions and the definitions of internal and demagnetizing fields field (2.24) and (2.25), respectively, the magnetization curve is corrected for the shape and shown in Figure 3.14, where the magnetization is plotted against the internal field. Clearly, the shape effects have been corrected for, as both curves coincide, and we are left with intrinsic material properties. In particular, we find $m_s = 4.89 \times 10^5$ A/m for nickel.

For the reference FE analysis, these shape-corrected magnetization curves are fitted to a Langevin-type magnetization curve (see Section 2.7). We find $\alpha = 1.71 \times 10^{-4}$ m/A for nickel. This fit is also shown in Fig. 3.14. Note that, by using a Langevin function, hysteresis is neglected.

The magnetic torque was measured using a custom-built torque magnetometer developed by Bergmüller et al. [1994], which works by applying a

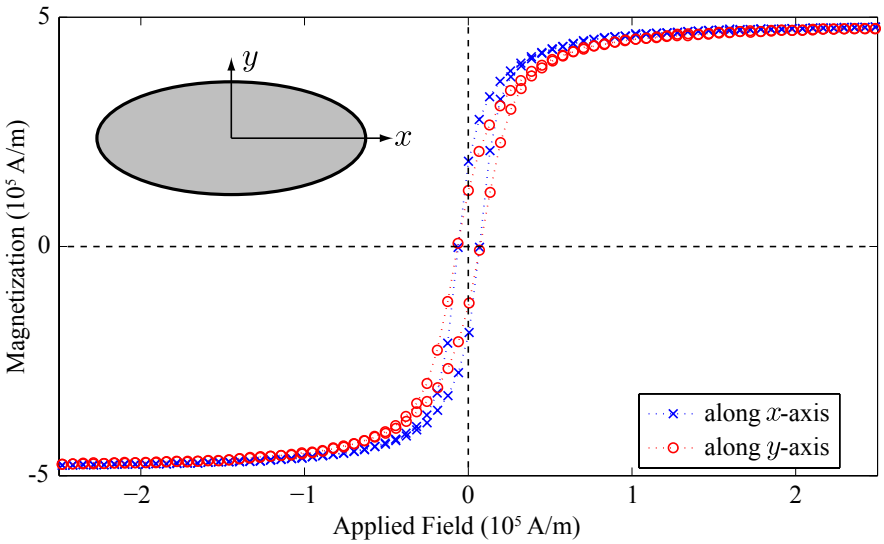

Figure 3.13: Original magnetization data for nickel taken along two axes.

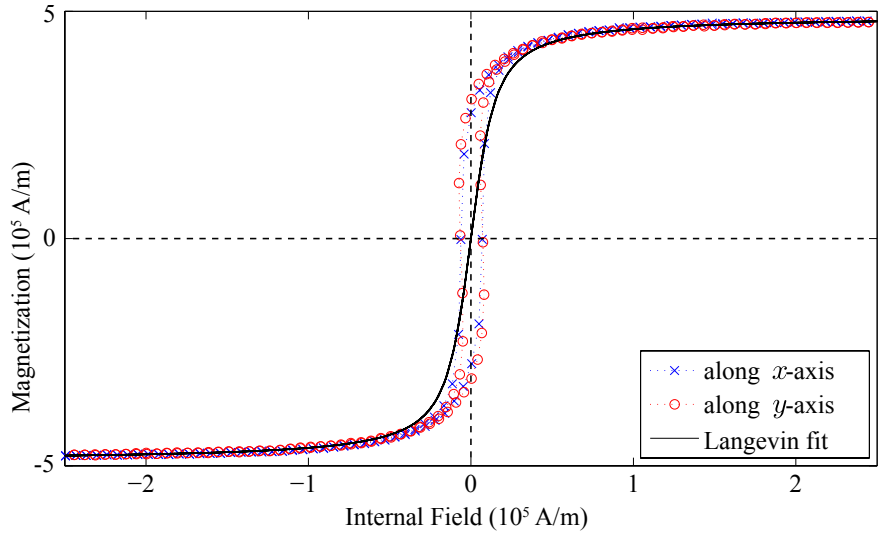

Figure 3.14: Magnetization data corrected for shape effects using known demagnetizing factors, and the best Langevin fit. This fit is used in FE calculations.

uniform field at a desired angle with respect to the microrobot. Before the torque on the microrobot was measured, the noise in the system was measured by measuring the torque signal of the sample holder. This signal was then subtracted from the torque measurement on the microrobot. It is not possible to know the precise orientation of the sample in the magnetometer. But since it is known that no torque is expected at 0° and 90°, the data is shifted by a few degrees to match these transitions. In the following, we use these corrected measurements.

The torque results are shown in Fig. 3.15, along with corresponding analytical and FE results. We see very good agreement between the experimental data and the FE results. Generally, we find good agreement between our model (the only available model) and the experimental data. The sharp corners in our model stemming from the transition to saturation are smoothed by the data and the FE results due to the smoother transition from the linear to the saturated region.

In Fig. 3.15(a) we can observe the effect of the dominant shape, considering only the torque on the plate perpendicular to the applied field plane (dashed curve). We see that, both, the assembled and the dominant shape model model predict almost the same torque, and we can conclude that the dominant shape is an adequate predictor for the torque on the entire structure. The assumption of larger magnetization resulting in a larger torque for the assembled model, is counteracted by considering only the dominant shape, thereby reducing the predicted torque.

Figure 3.15(b) shows the results for the 'cross' configuration. As expected, we observe that for very low fields the torque is zero from FEM results and our model (note that the field $b = 0.016$ corresponds to $B = 0.01$T and is below the rest field of the torque magnetometer, so no experimental data is available). This confirms our finding in Section 3.3.1 that for low fields the torque ratio in the cross configuration is -1 (see Fig. 3.6), and is due to the torques on the individual parts canceling each other out. So for these fields, the torque along the long axis of the microrobot vanishes as does the torque around the long axis of a body with axial symmetry. However, increasing the applied field leads to different magnetizations and, hence, different torques on the individual parts. Therefore, a net torque is exerted on the microrobot. This net torque vanishes at 0° and 45°, which is expected from the symmetry.

3.5 Summary and Contributions

The torque acting on a soft-magnetic sample has been analyzed based on the description introduced in Chapter 2. The results agree with the classical approach, and properly handle the continuous transition between the linear and saturated region. In addition to the increased computation speed stemming from the results of the previous chapter, we can predict minimal torques, the limit value for the torque, and that for fields applied at angles $< 45^\circ$, the torque will always increase, while for $> 45^\circ$, the torque attains a maximum and then decreases asymptotically to its limit.

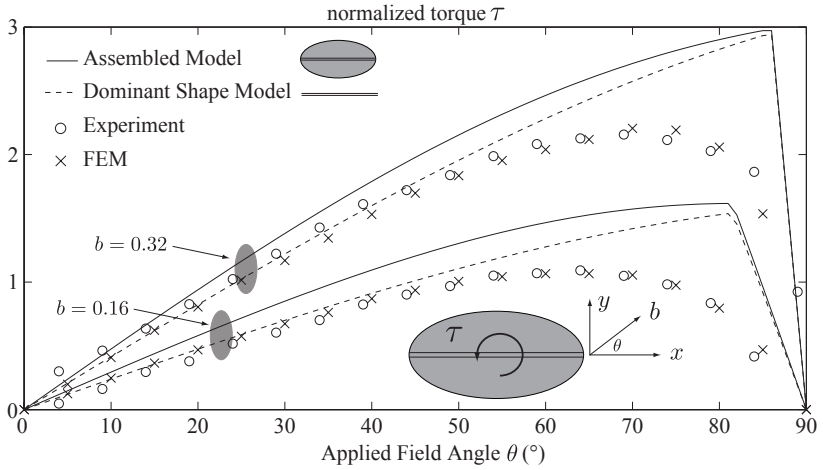

(a) Torque about z-axis versus applied field angle. The field is applied in the xy-plane. We see that the torque on the microrobot is essentially provided by the dominant shape perpendicular to the applied field plane.

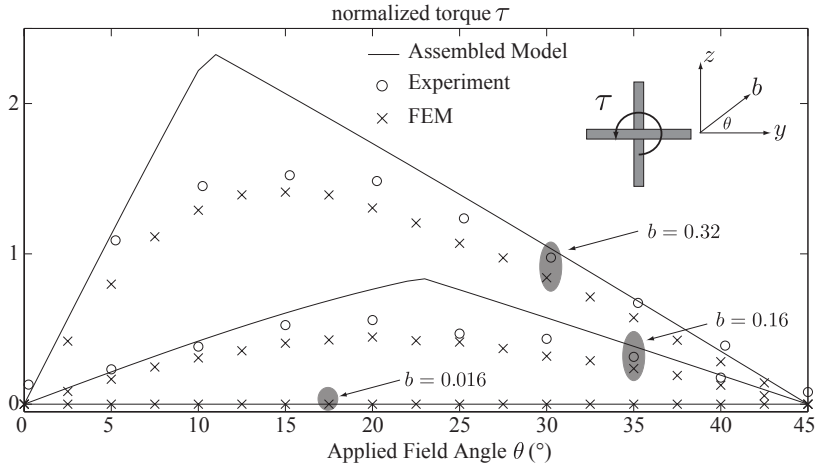

(b) Torque about x-axis versus applied field angle. The field is applied in the yz-plane. Note that the model and FEM predict zero torque for sufficiently low field magnitude.

Figure 3.15: Comparison of analytical model, FEM simulations, and experimental data for the torque on an assembled microrobot. Insets show the orientation of the applied field and the resulting torque. Good agreement is observed between the data, the FEM results and the assembled model assuming linear superposition. The plots are grouped according to the normalized applied field strength b.

Next, we analytically analyzed superposition of shapes and showed that mutual effects only occur for close shapes and fields below saturation. This provides a method to compute approximations of the forces and the torques acting on a soft-magnetic 3D assembled-MEMS device.

The results were then applied to the ophthalmic microrobot presented by Yesin et al. [2006]. We found very good agreement between analytical, FEM and experimental data. The model captures the behavior of the individual parts, as well as the behavior of the assembled microrobot, which was not possible with previous methods.

The proposed model captures the magnetic behavior of devices assembled from thin parts that are widely used in MEMS. In fact, most of the structures of interest fabricated by MEMS processes will be similar to the planar parts analyzed in this chapter. Therefore, this method can be used to model a variety of MEMS devices, both tethered and untethered.

Previous work does not allow for full 6-DOF control of magnetic devices due to the simplicity of the structures considered. For example, spherical bodies can be controlled with up to 3-DOF and axially symmetric bodies with up to 5-DOF Abbott et al. [2007]. Our model captures the characteristics of complex 3D structures and allows us, for the first time, to consider full 6-DOF control of untethered devices. This will provide major advances in the control of *in vivo* biomedical devices, as well as in wireless micromanipulation systems.

3.6 References

Abbott, J. J., Ergeneman, O., Kummer, M. P., Hirt, A. M., and Nelson, B. J. (2007). Modeling magnetic torque and force for controlled manipulation of soft-magnetic bodies. *IEEE Trans. on Robotics*, 23(6):1247–1252.

Beleggia, M., De Graef, M., and Millev, Y. T. (2006). The equivalent ellipsoid of a magnetized body. *J. Physics D*, 39(5):891–899.

Bergmüller, F., Bärlocher, C., Geyer, B., Grieder, M., Heller, F., and Zweifel, P. (1994). A torque magnetometer for measurements of the high-field anisotropy of rocks and crystals. *Measurement Science and Technology*, 5(12):1466–1470.

Iwase, E. and Shimoyama, I. (2005). Multistep sequential batch assembly of three-dimensional ferromagnetic microstructures with elastic hinges. *J. Microelectromech. Syst.*, 14(6):1265–1271.

Judy, J. W. and Muller, R. S. (1997). Magnetically actuated, addressable microstructures. *J. Microelectromech. Syst.*, 6(3):249–256.

Kummer, M., Abbott, J. J., Kratochvil, B. E., Borer, R., Sengul, A., and Nelson, B. J. (2010). Octomag: An electromagnetic system for 5-DOF wireless micromanipulation. In *Proc. IEEE Int. Conf. Robot. Automat.*

Syms, R. R. A., Yeatman, E. M., Bright, V. M., and Whitesides, G. M. (2003). Surface tension-powered self-assembly of microstructures—the state-of-the-art. *J. Microelectromech. Syst.*, 12(4):387–417.

Yang, G., Gaines, J. A., and Nelson, B. J. (2005). Optomechatronic design of microassembly systems for manufacturing hybrid microsystems. *IEEE Trans. Ind. Electron.*, 52(4):1013–1023.

Yesin, K. B., Vollmers, K., and Nelson, B. J. (2006). Modeling and control of untethered biomicrorobots in a fluidic environment using electromagnetic fields. *Int. J. Robot. Res.*, 25(5-6):527–536.

With magnetism, power of uncondensed steam, gravitation, radiant energy of electric waves, equilibrium and activity of atoms, all inscrutable to human eyes, man still cries, "I believe only what I can see"

anonymus

CHAPTER 4

Modeling the Motion of Microrobots using Non-Smooth Multi-Body Dynamics

In this chapter, we apply non-smooth multi-body dynamics to describe the motion of microrobots. After introducing the mathematical background, we apply the theory to the wireless resonant magnetic microactuator, in particular the MagMite microrobots, as an example. We first analyze the robot using a simplified analytical model, which allows us to derive characteristic and non-dimensional parameters that describe its dynamics. We then perform a numerical study to analyze the nonlinearities. We can predict several non-intuitive phenomena, such as switching of the direction of the velocity with changing excitation frequency, and show that both erratic and controlled motion occur under specific conditions. While consistent with the experimental observations, our numerical results indicate that previous speculations on the motion mechanism may be wrong. The presented method is readily applied to other microrobots as well.

4.1 Introduction

For effective propulsion at the microscale, methods that convert external energy directly into mechanical motion without any complex mechanisms, e.g., those involving cogs or electronic circuits, are more practical as they lower energy loss and fabrication complexity.

As an example, consider the wireless resonant magnetic microactuator (WRMMA) introduced by Vollmers et al. [2008] and shown in Fig. 4.1(a). The WRMMA consists of two nickel masses connected through a gold spring

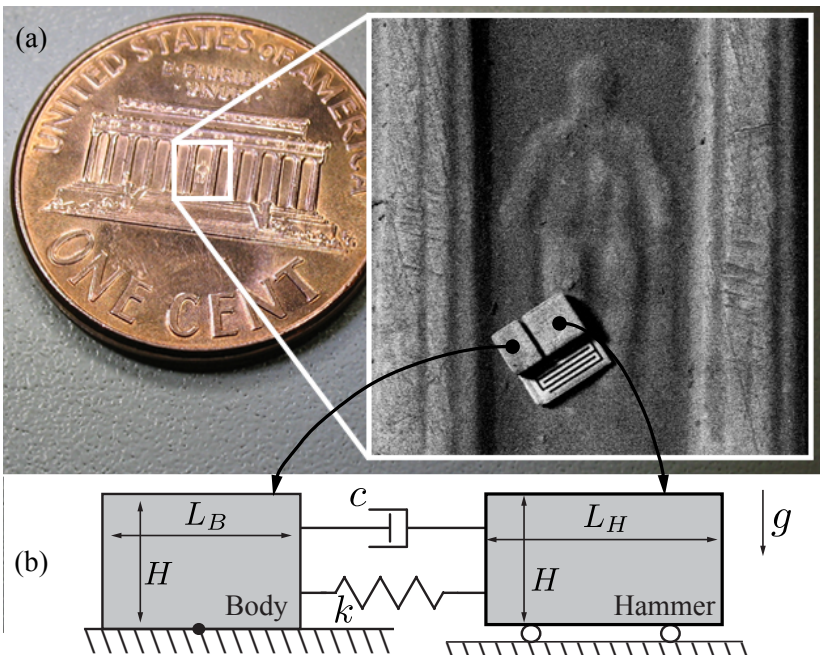

Figure 4.1: (a) Wireless resonant magnetic microactuator in size comparison with a US penny. (b) 1D Mechanical model of the WRMMA. Both body and hammer have height H and width W (not shown), L_B denotes the length of the body, and L_H the length of the hammer, and c, k, and g are the damping coefficient, the spring stiffness, and the gravitational acceleration respectively.

and has overall dimensions of roughly $300 \times 300 \times 50\mu m^3$. As shown in Fig. 4.1(b), one mass—the body—rests on a gold support structure which in turn has frictional contact with the substrate, whereas the other one—the hammer—is lifted above the ground and can move freely without friction.

Initially not magnetized, the nickel bodies become magnetized when an external magnetic field is applied. As a result, an attractive magnetic force arises between them. Then, time-variant magnetic fields are used to induce oscillatory motion and, it is assumed that, impact between the hammer and the body drives the robot forward. An additional electrostatic clamping force between the body and the substrate allows to control the vertical (reaction) force between the robot and the substrate.

Primary responses and driving behaviors have been experimentally characterized by Frutiger et al. [2010], and the overall performance was observed to be largely as intended by design: first, reliable turning behavior thanks to alignment with the external magnetic field, and second, controlled forward and backward motion thanks to rectification with a phase-shifted clamping force. Besides these primary behaviors several other modes of operation have been discovered, e.g, naturally driving backwards without the need for a clamping signal. Furthermore, phenomena such as changing the velocity

direction when increasing or decreasing the frequency, and also erratic behaviors, were observed.

Several impact actuators have been presented in literature (see for example the work by Zhao et al. [2004] and references therein), and analysis of their nonlinear behavior is also available. In general, the analysis is focused on the conditions necessary for impact, and it is implicitly assumed that impact is necessary for motion. However, Mita et al. [2003] observe experimentally that the actuator might drive backwards under certain conditions. Yet, the results of Zhao et al. [2004] do not predict this. In fact, most models do not address the influence of external parameters, such as friction or actuation schemes that are different from a harmonic force. However, in the case of the WRMMA, these parameters have significant influence on the driving performance. For example, with the electrostatic clamping force, an additional variable vertical force can be applied, resulting in a variable friction force or the robot can be fixed and released periodically.

The contribution of this chapter are a basic theoretical model and the numerical analysis necessary to design the WRMMA and predict its motion. The chapter is organized as follows. We first review the mathematical background of non-smooth multi-body dynamics with unilateral contact. This is necessary to model mechanical systems with impact and friction such as the WRMMA. Then, we describe the WRMMA and present a simplified analytical model of it. This model is used to derive its characteristic and non-dimensional parameters. Finally, we conduct numerical simulations to determine the motion mechanism of the WRMMA, and investigate the influence of the system parameters on the performance, e.g., the velocity of the WRMMA.

4.2 Non-Smooth Multi-Body Dynamics with Set-Valued Force Laws

We review the relevant parts of the mathematical framework of non-smooth multi-body dynamics with set-valued force laws. We follow closely the description by Leine and van de Wouw [2008] and Transeth et al. [2008]. The focus is laid on unilateral contacts with impact and friction. A complete review is beyond the scope of this thesis, and for a detailed introduction the reader is referred to standard textbooks [Glocker, 2001; Leine and Nijmeijer, 2004; Leine and van de Wouw, 2008] and research results [Moreau, 1988; Transeth et al., 2008].

4.2.1 Notation and Mathematical Preliminaries

Definition 4.1. ***(Normal Vector)*** *Let $C \subset \mathbb{R}^n$ be a convex set and $\mathbf{x} \in C$. A vector $\mathbf{y} \in \mathbb{R}^n$ is normal to $\mathbf{x}$ with respect to C if*

$$\mathbf{y}^T(\mathbf{x}^\star - \mathbf{x}) \leq 0, \quad \mathbf{x} \in C, \forall \mathbf{x}^\star \in C. \tag{4.1}$$

Definition 4.2. ***(Normal Cone)*** *Let $C \subset \mathbb{R}^n$ be a convex set and $\mathbf{x} \in C$. The set of vectors $\mathbf{y} \in \mathbb{R}^n$ that are normal to $\mathbf{x}$ form the normal cone $N_C(\mathbf{x})$ of C in $\mathbf{x}$*

$$N_C(\mathbf{x}) = \left\{ \mathbf{y} \mid \mathbf{y}^T(\mathbf{x}^\star - \mathbf{x}) \leq 0, \mathbf{x} \in C, \forall \mathbf{x}^\star \in C \right\}. \tag{4.2}$$

If $\mathbf{x}$ is in the interior of C then $N_C(\mathbf{x}) = 0$. If $\mathbf{x} \notin C$, then $N_C(\mathbf{x}) = \emptyset$.

Definition 4.3. ***(Proximal Point)*** *The proximal point of a closed convex set C to a point $\mathbf{z}$ is the closest point in C to $\mathbf{z}$*

$$prox_C(\mathbf{z}) = argmin_{\mathbf{x}^\star \in C} ||\mathbf{z} - \mathbf{x}^\star||, \quad \mathbf{z} \in \mathbb{R}^n. \tag{4.3}$$

The vector $\mathbf{z} - \text{prox}_C(\mathbf{z})$ is an element of the normal cone of C at the proximal point, i.e.,

$$\mathbf{x} = \text{prox}_C(\mathbf{z}) \iff \mathbf{z} - \mathbf{x} \in N_C(\mathbf{x}), \tag{4.4}$$

and by substituting $\mathbf{z} = \mathbf{x} - r\mathbf{y}$, and noting that $-\mathbf{y} \in N_C(\mathbf{x}) \Leftrightarrow -r\mathbf{y} \in N_C(\mathbf{x})$ for $r > 0$, we find

$$\mathbf{x} = \text{prox}_C(\mathbf{x} - r\mathbf{y}), r > 0 \iff -\mathbf{y} \in N_C(\mathbf{x}) \tag{4.5}$$

4.2.2 Multibody Dynamics

In what follows, we will assume a multibody system comprised of n rigid, i.e. non-deformable, and convex bodies. The position and orientation of such a system in space is described by a set of generalized coordinates $\mathbf{q} \in \mathbb{R}^{fn}$, where f is the number of degrees of freedom for each body, e.g. $f = 3$ for planar motion with three degrees of freedom x, y, θ.

Smooth Equations of Motion

The smooth, i.e., impact- and friction-free, Newton-Euler equations of motion for this system read

$$\mathbf{M}\ddot{\mathbf{q}} - \mathbf{h}(\mathbf{q}, \dot{\mathbf{q}}, t) = \mathbf{0}, \tag{4.6}$$

where $\mathbf{M} \in \mathbb{R}^{fn \times fn}$ is the mass matrix, t represents the time, $\dot{(\cdot)}$ denotes the differentiation with respect to t, i.e. $\dot{(\cdot)} = \frac{\mathrm{d}}{\mathrm{d}t}(\cdot)$, $\mathbf{h}$ is the vector of generalized smooth, noncontact forces, e.g., gravity, magnetic force, spring, damping forces, etc., and $\dot{\mathbf{q}} \in \mathbb{R}^{fn}$ and $\ddot{\mathbf{q}} \in \mathbb{R}^{fn}$ represent the generalized velocities and accelerations of the system.

Rigid Body Kinematics

We describe the position and orientation in space of a rigid body j by its generalized coordinates $\mathbf{q}_j$ as

$$\mathbf{q}_j = \begin{pmatrix} {}_I\mathbf{r}_G \\ \mathbf{p} \end{pmatrix} \in \mathbb{R}^7, \tag{4.7}$$

where ${}_I\mathbf{r}_G \in \mathbb{R}^3$ is the position of the center of the gravity of the rigid body with respect to the inertial frame $I = (O, \mathbf{e}_x^I, \mathbf{e}_y^I, \mathbf{e}_z^I)$, and $\mathbf{p} = (e_0, \mathbf{e})^{\mathrm{T}}$ with $e_0 \in \mathbb{R}$ and $\mathbf{e} = (e_1, e_2, e_3) \in \mathbb{R}^3$ is a unit quaternion describing its orientation.

It is constrained by $\mathbf{p}^{\mathrm{T}}\mathbf{p} = 1$. The transformation from a body-fixed frame B into the inertial frame is done through the rotation matrix $\mathbf{R}_B^I$, i.e., ${}_I\mathbf{r} = \mathbf{R}_B^I {}_B\mathbf{r}$, calculated from the unit quaternion as

$$\mathbf{R}_B^I = \left(2e_0^2 - 1\right)\mathbf{I} + 2\left(\mathbf{e}\mathbf{e}^{\mathrm{T}} + e_0\tilde{\mathbf{e}}\right), \tag{4.8}$$

where

$$\tilde{\mathbf{e}} = \begin{pmatrix} 0 & -e_3 & e_2 \\ e_3 & 0 & -e_1 \\ -e_2 & e_1 & 0 \end{pmatrix} \tag{4.9}$$

is the skew-symmetric form of $\mathbf{e}$. The rotation matrix can also be computed from $\mathbf{R}_B^I = \mathbf{H}\bar{\mathbf{H}}^{\mathrm{T}}$, with

$$\mathbf{H} = \begin{pmatrix} -\mathbf{e} & \tilde{\mathbf{e}} + e_0\mathbf{I} \end{pmatrix}, \tag{4.10}$$

and

$$\bar{\mathbf{H}} = \begin{pmatrix} -\mathbf{e} & -\tilde{\mathbf{e}} + e_0\mathbf{I} \end{pmatrix}. \tag{4.11}$$

In the planar case, $\mathbf{q}_j$ simplifies to

$$\mathbf{q}_j = \begin{pmatrix} {}_I\mathbf{r}_G \\ \theta \end{pmatrix} \in \mathbb{R}^3, \tag{4.12}$$

where now ${}_I\mathbf{r}_G \in \mathbb{R}^2$, and $\theta \in \mathbb{R}$ describes the orientation of the rigid body with respect to the global x-axis.

Of course, whether the generalized coordinates of a rigid body have the form (4.7) or (4.12) depends on the problem, and it is possible that only a subset has to be considered, e.g. if rotations can be neglected, $\mathbf{p}$ is not used in (4.7) and then $\mathbf{q}_j = {}_I\mathbf{r}_G \in \mathbb{R}^3$.

For a system consisting of m rigid bodies the individual $\mathbf{q}_j$ are collected in a vector $\mathbf{q} = \left(\mathbf{q}_1^{\mathrm{T}}, \mathbf{q}_2^{\mathrm{T}}, \ldots, \mathbf{q}_m^{\mathrm{T}}\right)^{\mathrm{T}}$.

Contact Kinematics

Consider the two convex bodies, say body 1 and body 2, shown in Fig. 4.2, and assume that the region where they are close to each other is sufficiently smooth. In each body-fixed point C_i on the surface of body i, we can define an outward normal $\mathbf{n_i}$ and a tangent plane T_i spanned by vectors $\mathbf{t}_i$ and $\mathbf{s}_i$.

Two points C_1 and C_2 on the surface of body 1 and body 2 respectively, are said to form a contact pair, if their normals oppose each other, i.e.,

$$\mathbf{n_1} = -\mathbf{n_2}. \tag{4.13}$$

To determine whether the bodies are in contact or not, we define the contact distance, or normal gap, g_N as

$$g_N = \left(\mathbf{r}_{OC_2} - \mathbf{r}_{OC_1}\right)^{\mathrm{T}} \mathbf{n}_1 = \left(\mathbf{r}_{OC_1} - \mathbf{r}_{OC_2}\right)^{\mathrm{T}} \mathbf{n}_2. \tag{4.14}$$

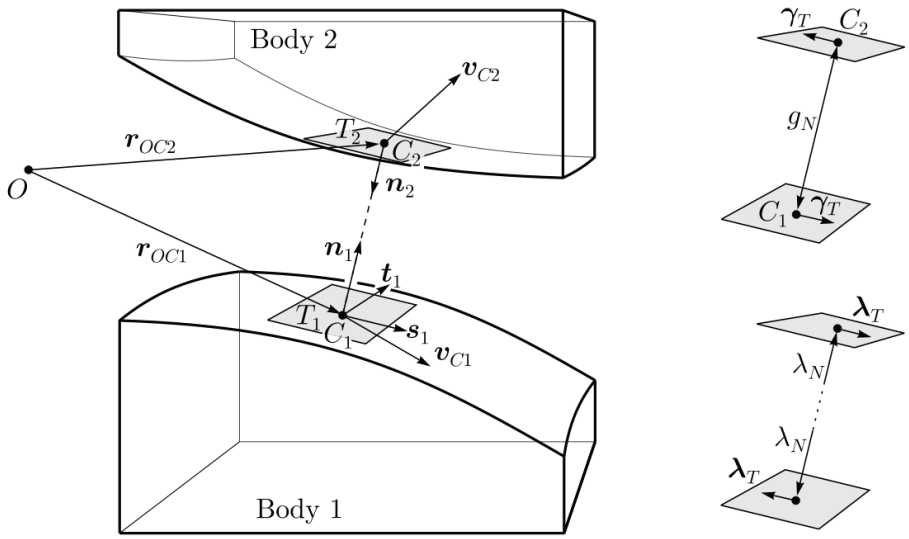

Figure 4.2: Contact kinematics, taken from Leine and van de Wouw [2008]

We say that the bodies are separated if $g_N > 0$, are in contact if $g_N = 0$, and penetrate each other if $g_N < 0$. The relative normal velocity γ_N of the bodies is defined as

$$\gamma_N = \left(\mathbf{v}_{C_2} - \mathbf{v}_{C_1}\right)^{\mathrm{T}} \mathbf{n}_1 \tag{4.15}$$

where the $\mathbf{v}_{C_i}$ are the absolute velocities of the points C_i. In addition, the components γ_{T_j} of the relative tangential velocity $\boldsymbol{\gamma}_T = \left(\gamma_{T_1}, \gamma_{T_2}\right)^{\mathrm{T}} \in T_1$ are given by

$$\gamma_{T_1} = \left(\mathbf{v}_{C_2} - \mathbf{v}_{C_1}\right)^{\mathrm{T}} \mathbf{t}_1, \quad \gamma_{T_2} \left(\mathbf{v}_{C_2} - \mathbf{v}_{C_1}\right)^{\mathrm{T}} \mathbf{s}_1, \tag{4.16}$$

and in case of contact, i.e., $g_N = 0$, $\boldsymbol{\gamma}_T$ is the relative sliding velocity.

4.2.3 Set-Valued Force Laws for Unilateral Contact with Impact and Friction

This section describes the set-valued force laws for Coulomb friction and normal contact on velocity level. Initially formulated as inclusions, the force laws are then reformulated using the proximal point function for the numerical implementation.

We will employ hard contact laws, that is, assume impenetrability of the bodies and idealize the contact area to a contact point thereby neglecting the local indentation of the bodies. In case of impact, this assumptions allow us to avoid unphysical penetration, additional parameters (e.g. spring-damper contact), and the resulting stiff ordinary differential equations (ODEs).

On the other hand, we model physical restitution behavior at the cost of a set-valued force law. In case of friction, a hard friction law allows to model sticktion effects which are not possible by employing a regularized (e.g. an arctan function) ODE. Again, a set-valued force law is required.

Signorini's Contact Law

In case of unilateral contact ($g_N = 0$), the contact force (not impulse) λ_N along the normal direction of the contact is nonnegative ($\lambda_N \geq 0$). However, when the contact is open $g_N > 0$, the contact force must vanish, i.e., $\lambda_N = 0$. This is known as Signorini's contact law and is formulated on displacement level as an inequality complementarity condition between g_N and λ_N as

$$g_N \geq 0, \quad \lambda_N \geq 0, \quad g_N \lambda_N = 0. \tag{4.17}$$

On velocity level, the relationship between the relative velocity γ_N and λ_N for a closed contact $g_N = 0$ can be expressed as an inclusion

$$-\gamma_N \in N_{C_N}(\lambda_N) \tag{4.18}$$

where $C_N = \{\lambda_N \mid \lambda_N \geq 0\} = \mathbb{R}^+$ is the convex set of admissible contact forces, and N_{C_N} is the normal cone to C_N.

Newton Impact Law

Signorini's contact law (4.18) does not cover impact. A Newton-type normal impact with restitution coefficient ε_N is modeled as

$$\gamma_N^+ = -\varepsilon_N \gamma_N^-, \quad g_N = 0, \quad 0 \leq \varepsilon \leq 1 \tag{4.19}$$

where γ_N^+ and γ_N^- are the post- and pre-impact velocities respectively. Impact is characterized by a sudden change in the relative velocity, accompanied by a normal contact impulse $\Lambda_N > 0$. In situations, where the contact does not participate in the impact, often in multi-contact situations, we have $\Lambda_N = 0$ and allow for higher postimpact velocities than prescribed by Newtons impact law, i.e., $\gamma_N^+ > -\varepsilon_N \gamma_N^-$. Thus, similarly to Signorini's contact law, Newton-type impact can be modeled as an inequality complementarity condition

$$\Lambda_N \geq 0, \quad \xi_N \geq 0, \quad \Lambda_N \xi_N = 0, \tag{4.20}$$

with $\xi_N = \gamma_N^+ + \varepsilon_N \gamma_N^-$, and can be expressed on velocity level as inclusion

$$-\xi_N \in N_{C_N}(\Lambda_N) \tag{4.21}$$

where $C_N = \mathbb{R}^+$ is the convex set of admissible normal impulses.

Coulomb Friction Force

The spatial Coulomb friction law is a constitutive law relating the normal and the tangential contact forces. It can be modeled as an inclusion on velocity level as

$$-\boldsymbol{\gamma}_T \in N_{C_T}(\boldsymbol{\lambda}_T) \tag{4.22}$$

where $\boldsymbol{\gamma}_T$ is the relative sliding velocity, N_{C_T} is the normal cone to the set C_T and

$$C_T = \{\boldsymbol{\lambda}_T \mid ||\boldsymbol{\lambda}_T|| \leq \mu \lambda_N\} \tag{4.23}$$

is the set of admissible friction forces for isotropic friction with $\mu > 0$ being the friction coefficient.

4.2.4 Non-Smooth Equations of Motion

We now formulate the non-smooth equations of motion with unilateral frictional contact. The main approach is to take the contact (impulsive and non-impulsive) forces as Lagrange multipliers into account and modify (4.6) accordingly.

In case of impact-free motion ($\Lambda_N = 0$), and denoting by $\mathcal{H} = \{i \mid g_{N_i} = 0\}$ the set of closed contacts, this yields

$$\mathbf{M}\dot{\mathbf{u}} - \mathbf{h}(\mathbf{q}, \mathbf{u}, t) = \sum_{i \in \mathcal{H}} \mathbf{w}_{N_i} \lambda_{N_i} + \mathbf{w}_{T_i} \boldsymbol{\lambda}_{T_i}. \tag{4.24}$$

For the general 3D motion of n bodies j, it holds that $\mathbf{F}(\mathbf{q})\mathbf{u} = \dot{\mathbf{q}}$ almost everywhere, with

$$\mathbf{F}(\mathbf{q}) = \begin{pmatrix} \mathbf{F}_{H1} & \mathbf{0}_{7\times6} & \cdots & \mathbf{0}_{7\times6} \\ \mathbf{0}_{7\times6} & \mathbf{F}_{H2} & \cdots & \vdots \\ \vdots & & \ddots & \mathbf{0}_{7\times6} \\ \mathbf{0}_{7\times6} & \cdots & \mathbf{0}_{7\times6} & \mathbf{F}_{Hn} \end{pmatrix} \tag{4.25}$$

and

$$\mathbf{F}_{Hj} = \begin{pmatrix} \mathbf{I}_{3\times3} & \mathbf{0}_{3\times3} \\ \mathbf{0}_{4\times3} & \frac{1}{2}\bar{\mathbf{H}}_j^T \end{pmatrix} \tag{4.26}$$

where $\bar{\mathbf{H}}$ is found from (4.11).

For the planar case considered in this thesis, we have $\mathbf{F}(\mathbf{q}) = \mathbf{I}$, thus in (4.24) we have $\mathbf{u} = \dot{\mathbf{q}}$ almost everywhere. And $\mathbf{w}_{N_i}$ and $\mathbf{w}_{T_i}$ designate the generalized force directions in normal and tangential directions respectively. For the planar case, they are found from

$$\mathbf{w}_{N_i} = \left(\frac{\partial g_{N_i}}{\partial \mathbf{q}}\right)^{\mathrm{T}}, \quad \text{and} \quad \mathbf{w}_{T_i} = \left(\frac{\partial \gamma_{T_i}}{\partial \dot{\mathbf{q}}}\right)^{\mathrm{T}}. \tag{4.27}$$

In case of impact, and more specifically during the time-instant of impact, the equations read

$$\mathbf{M}(\mathbf{u}^+ - \mathbf{u}^-) = \sum_{i \in \mathcal{H}} \mathbf{w}_{N_i} \Lambda_{N_i} + \mathbf{w}_{T_i} \boldsymbol{\Lambda}_{T_i}. \tag{4.28}$$

Since impact is usually associated with jumps in the velocity and are modeled to occur instantaneously, the time derivative of the velocity $\mathbf{u}(t)$ does not always exist. To account for this, an atomic measure $\mathrm{d}\eta$ is introduced and assumed that the differential measure $\mathrm{d}\mathbf{u}$ can be decomposed as

$$\mathrm{d}\mathbf{u} = \dot{\mathbf{u}}\mathrm{d}t + (\mathbf{u}^+ - \mathbf{u}^-)\mathrm{d}\eta, \tag{4.29}$$

where $\mathrm{d}t$ is the Lebesgue measure and $\int_{\{t_1\}} \mathrm{d}\eta = 1$. The latter property allows us to integrate over a singleton $\{t_1\}$, and thus take impact into account.

Consequently, the impact-free equation of motion (4.24) and the impact equation (4.28) can be combined into

$$\mathbf{M}\mathrm{d}\mathbf{u} - \mathbf{h}(\mathbf{q}, \mathbf{u}, t)\mathrm{d}t = \sum_{i \in \mathcal{H}} \mathbf{w}_{N_i}\mathrm{d}P_{N_i} + \mathbf{w}_{T_i}\mathrm{d}\mathbf{P}_{T_i} \tag{4.30}$$

with the contact impulse measures

$$\mathrm{d}P_{N_i} = \lambda_{N_i}\mathrm{d}t + \Lambda_{N_i}\mathrm{d}\eta, \text{ and} \tag{4.31}$$
$$\mathrm{d}\mathbf{P}_{T_i} = \boldsymbol{\lambda}_{T_i}\mathrm{d}t + \boldsymbol{\Lambda}_{N_i}\mathrm{d}\eta, \tag{4.32}$$

which satisfy the inclusions

$$-\mathrm{d}P_{N_i} \in N_{C_N}(\xi_N), \text{ and} \tag{4.33}$$
$$-\mathrm{d}\mathbf{P}_{T_i} \in N_{C_T}(\boldsymbol{\xi}_T) \tag{4.34}$$

with N_{C_N} and N_{C_T} being the normal cones of the admissible normal and tangential impulses respectively.

The equality of measures (4.30) describes the dynamics of a system composed of multiple bodies at velocity level with impact and friction and because of the atomic measure, it yields meaningful results even in case of velocity jumps. Its numerical integration is detailed in the next section.

4.2.5 Time Discretization

The algorithm for the numerical integration of the equality of measures (4.30) has been introduced in Moreau [1988] and uses a mid-point time stepping integration scheme. Given an initial state, the goal is find the state of the system at the next time instant.

The main idea behind the mid-point time stepping scheme is to divide the problem into two subproblems. First, during the first half integration step, the contact problem is solved, i.e., the closed contacts are determined, and the corresponding percussion measures are calculated. Then, the states of the system are moved accordingly during the second half integration step.

We now briefly review the relevant aspects of the algorithm. Assume an integration interval $I = [t_A, t_E]$ where t_A is the time at the beginning of integration and t_E at the end of it. Then, we set $\mathbf{q}_A = \mathbf{q}(t_A)$ and $\mathbf{u}_A = \mathbf{u}(t_A)$ as the generalized coordinates and velocities at time t_A. The objective is to determine their values at the end of the integration interval, i.e., $\mathbf{q}_E = \mathbf{q}(t_E)$ and $\mathbf{u}_E = \mathbf{u}(t_E)$. This is done in four main steps:

Step 1: Determine the mid-point t_M of the integration interval I, and the corresponding states of the generalized coordinates $\mathbf{q}_M$

$$t_M = t_A + \frac{1}{2}\Delta t, \tag{4.35}$$
$$\mathbf{q}_M = \mathbf{q}_A + \frac{1}{2}\mathbf{F}(\mathbf{q}_A)\mathbf{u}_A\Delta t, \tag{4.36}$$

where Δt is the step size.

Step 2: At t_M, determine the set of closed contacts $\mathcal{H} = \{i \mid g_{N_i}(\mathbf{q}_M, t_M) \leq 0\}$ by solving the contact kinematics (4.14).

Step 3: Solve the contact problem. In time-discretized form, the equality of measures at time t_M (4.30) reads

$$\mathbf{M}(\mathbf{u}_E - \mathbf{u}_A) - \mathbf{h}\Delta t = \sum_{i \in \mathcal{H}} \mathbf{w}_{N_i} \mathrm{d}P_{N_i} + \mathbf{w}_{T_i} \mathrm{d}\mathbf{P}_{T_i}, \tag{4.37}$$

where $\mathbf{h} = \mathbf{h}(\mathbf{q}_M, \mathbf{u}_A, t_M)$. Two cases are distinguished:

Case 1: $\mathcal{H} = \emptyset$**.** All the contacts are open, and the contact impulse measures P_{N_i} and $\mathbf{P}_{T_i}$ are zero. We find the velocity $\mathbf{u}_E$ from (4.37) as

$$\mathbf{u}_E = \mathbf{u}_A + \mathbf{M}^{-1}\mathbf{h}\Delta t. \tag{4.38}$$

Case 2: $\mathcal{H} \neq \emptyset$**.** Closed contacts exist, and we have

$$\mathbf{u}_E = \mathbf{u}_A + \mathbf{M}^{-1}\left(\mathbf{h}\Delta t + \sum_{i \in \mathcal{H}} \mathbf{w}_{N_i} P_{N_i} + \mathbf{w}_{T_i} \mathbf{P}_{T_i}\right), \tag{4.39}$$

with unknowns P_{N_i} and $\mathbf{P}_{T_i}$. They are given as inclusions (4.33) and (4.34), and solved iteratively by rewriting them as proximal point equations based on the equivalence (4.5) as

$$-P_{N_i} \in N_{C_{N_i}}(\xi_{N_i}) \quad \Leftrightarrow \quad P_{N_i} = \mathrm{prox}_{\mathbb{R}_0^+}(P_{N_i} - r_N \xi_{N_i}) \tag{4.40}$$

$$-\mathbf{P}_{T_i} \in N_{C_{T_i}}(\boldsymbol{\xi}_{T_i}) \quad \Leftrightarrow \quad \mathbf{P}_{T_i} = \mathrm{prox}_{C_{T_i}}(\mathbf{P}_{T_i} - r_T \boldsymbol{\xi}_{T_i}) \tag{4.41}$$

with the admissible sets

$$C_{N_i} = \mathbb{R}_0^+, \text{ and} \tag{4.42}$$

$$C_{T_i} = \left\{\mathbf{P}_{T_i} \mid ||\mathbf{P}_{T_i}|| \leq \mu P_{N_i}\right\}, \tag{4.43}$$

the combined relative velocities

$$\xi_{N_i} = \gamma_{N_i E} + \varepsilon_N \gamma_{N_i A}, \text{ and} \tag{4.44}$$

$$\boldsymbol{\xi}_{T_i} = \boldsymbol{\gamma}_{T_i E}, \tag{4.45}$$

and the convergence parameters r_N and r_T. The larger r_N and r_T are chosen, the faster the Newton-Raphson method used to solve the proximal point equations (4.40) and (4.41) may converge. The solutions of (4.40) and (4.41) are then used in (4.39) to determine $\mathbf{u}_E$. However, convergence is not guaranteed, and too large values r_N and r_T may cause divergence. Therefore, a critical examination of the results is necessary.

Note that (4.45) may be extended similarly to (4.44) with a term $\varepsilon_T \boldsymbol{\gamma}_{T_i A}$ comprising a tangential restitution coefficient ε_T. This may be interesting when modeling springy ball effects. Yet, in this thesis, we will always assume $\varepsilon_T = 0$ unless otherwise specified.

Step 4 Determine the final states of the system

$$t_E = t_M + \frac{1}{2}\Delta t, \tag{4.46}$$

$$\mathbf{q}_E = \mathbf{q}_M + \frac{1}{2}\mathbf{F}(\mathbf{q}_M)\mathbf{u}_E\Delta t, \tag{4.47}$$

and use $\mathbf{q}_E$ and $\mathbf{u}_E$ as the start values for the next time step integration.

In conclusion, by performing steps 1—4 at each timestep, we can solve the initial value problem for the motion of a multi-body system with friction and impact (even frictional impact). Since the procedure involves Euler integration, the error is approximately of order $\mathcal{O}(\Delta t^2)$, thus the timestep Δt must be chosen sufficiently small to avoid numerical drift and sufficient frequency resolution.

Event-Driven Schemes

As an example for an event-driven scheme, consider the model by Pawashe et al. [2009] to describe the stick/slip motion of a microrobot. The authors explain that, during the numerical integration of the equations of motion, three possible solutions can occur: a) physically impossible cases (e.g. microrobot lost contact with surface), b) possible stick↔slip transitions depending on the friction force, and c) sticktion. These conditions must be evaluated at each time step and appropriate solutions must be then taken.

Clearly, the advantage of using the previously described time-stepping scheme over such an event-driven algorithm is its robustness, as it does not require the explicit distinction between the impact, stick and slip phases.

4.2.6 Solution from a Linear Complementarity Problem

As shown by Glocker and Studer [2005] for planar systems, the non-smooth equations of motion (4.24) and (4.28) can also be combined and rewritten as a linear complementarity problem (LCP). Thus, the contact problem can be solved with standard LCP solvers, providing an alternative to the iterative approach using the contact impulse measures. For many contacts, the iterative approach above is favorable as it uses the results from the previous time-step and can thus increase the computation speed. Also, the iterative approach is the sole possibility to model spatial friction, thus it is more general than the LCP description.

On the other hand, for few contacts and planar problems, both methods are comparable. In this work, we will employ the LCP method since we will consider a planar problem with only two contacts. For the solution of the LCP problem, Lemke's algorithm is used from a freely available source[1].

[1] `http://people.sc.fsu.edu/~jburkardt/m_src/lemke/lemke.html`

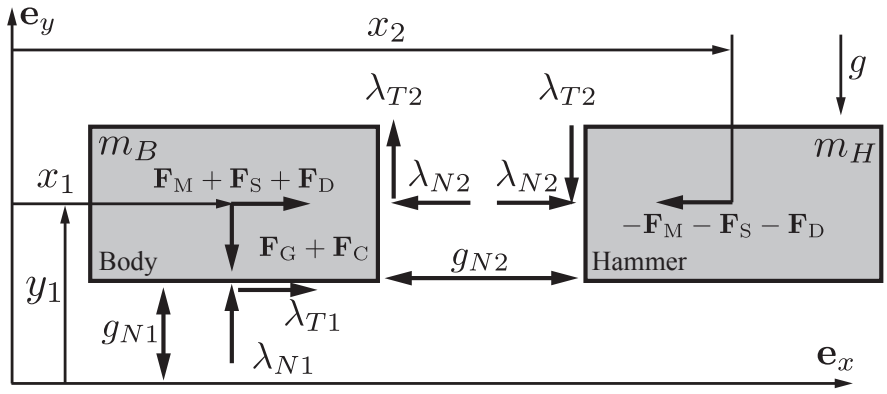

Figure 4.3: Free body diagram of the WRMMA.

4.3 Wireless Resonant Magnetic Microactuator—System Overview

In this Section, we review the parameters and forces required to model the motion of the Wireless Resonant Magnetic Microactuator (WRMMA)[2] presented by Vollmers et al. [2008].

The magnetic torque on the WRMMA will act such that the easy axis of the device, typically the long axis (but could be a diagonal, too), will align with the applied field. Since rotational inertia scales down faster with size compared to the mass, we assume that the forward motion begins after the WRMMA is aligned with the field. This assumption is well supported by experimental observations. Thus, a 1D model will be employed to describe its motion.

Figure 4.3 shows the free body diagram of the WRMMA. The position of the body is described with coordinates (x_1, y_1) and the hammer with coordinate x_2. Note, that y_1 is only necessary for consistency in the numerical integration procedure, since we consider only unilateral contacts that are allowed to open.

The λ_{Ni} and λ_{Ti} in Fig. 4.3 designate normal and tangential non-impulsive contact forces respectively. The other terms are explained in the following sections. Section 4.3.1 summarizes the forces stemming from the structure of the device, i.e., gravity, spring and damping forces and their parameters as determined by experiments. Then, we derive the forces applied to the microrobot, that is the magnetic driving force and the electrostatic clamping force in Section 4.3.2 and 4.3.3 respectively.

[2]The terms WRMMA, MagMite or microrobot are used interchangeably

4.3.1 Mass, Spring, Damper

The size of the device is such that it fits roughly a $300 \times 300 \times 50\mu m^3$ total volume [3]. In the first prototypes the body and the hammer each had a length of about 150µm, a width of $W = 130\mu m$ and a height of $H = 50\mu m$ as detailed in Vollmers et al. [2008]. The density of nickel is $\rho_{Ni} = 8900 kg/m^3$, which results in masses of the order of $10 \times 10^{-9} kg$ for each part. Experimental characterization and the determination of the parameter values used in the following has been carried out by Frutiger [2010].

As for modeling the geometry, we will consider devices with asymmetrical mass distribution. We denote by m_B the mass of the body and by $m_H = \alpha\, m_B$ the mass of the hammer, where $\alpha = m_H/m_B$ is the mass ratio. Further, we assume the same width and height for the body and the hammer, only the lengths differing. We consider a total device length of $L_{\text{device}} = L_H + L_B + g_0 = 300\mu m$, where L_H and L_B are the length of the hammer and the body respectively, and g_0 is the equilibrium gap (see (4.54) below). Because of equal height and width, we have

$$L_H = \alpha L_B \tag{4.48}$$
$$L_B = (L_{\text{device}} - g_0)/(1+\alpha) \tag{4.49}$$

and thus α equivalently designates a length ratio.

Neglecting the mass of the spring and the frame, the total mass m_T of the device is $m_T = m_B + m_H = (1+\alpha)m_B$, and the gravitational force $\mathbf{F}_G$ acting on the WRMMA is given by

$$\mathbf{F}_G = -F_G\, \mathbf{e}_y \tag{4.50}$$
$$= -\beta m_T g\, \mathbf{e}_y \tag{4.51}$$
$$= -\beta(1+\alpha) m_B g\, \mathbf{e}_y \tag{4.52}$$

where $g = 9.81 kg/m^2$, and $\beta > 0$ is a non-dimensional parameter to study the effect of unknown vertical forces, such as additional mass due to the gold frame and spring or parasitic electrostatic forces, leading to changing frictional behavior of the robot.

The spring stiffness k in the $\mathbf{e}_x$ direction has been found to be linear, thus the spring force acting on the body is given by

$$\mathbf{F}_S = F_S\, \mathbf{e}_x \tag{4.53}$$
$$= k\,(x_2 - x_1 - g_0)\ \mathbf{e}_x \tag{4.54}$$
$$= k\, g_{N2}\, \mathbf{e}_x \tag{4.55}$$

where g_{N2} is the gap between the body and the hammer, g_0 is the gap at rest, and $k = 10.6 N/m$ is a typical value.

[3] This was a requirement in the 2007 RoboCup Nanogram Demonstration Competition organized by NIST

As for the damping force $\mathbf{F}_\mathrm{D}$, we assume a linear drag coefficient c, stemming from squeeze-film damping, which has been described by Cheng and Fang [2005] or Andrews et al. [1993]. Thus, we have

$$\begin{aligned}\mathbf{F}_\mathrm{D} &= F_\mathrm{D}\,\mathbf{e}_\mathrm{x} && (4.56)\\ &= c\,(\dot{x}_2 - \dot{x}_1)\;\mathbf{e}_\mathrm{x}, && (4.57)\\ &= c\,\dot{g}_{N2}\,\mathbf{e}_\mathrm{x}, && (4.58)\end{aligned}$$

with $\dot{g}_{N2} = (\dot{x}_2 - \dot{x}_1)$ being the relative velocity of the body and the hammer, and $c \approx 1 \times 10^{-6}$Ns/m, well supported by experiments.

4.3.2 Magnetic Force

In a homogeneous magnetic field, no net force is exerted on a single, ideally soft, magnetic body because of the lack of magnetic field gradients (see (3.4)). Thus, the force between the parts of the WRMMA arises solely due to the interaction of both magnetizations.

The two nickel parts basically act as a magnetic flux concentrator, amplifying the applied magnetic flux $\mathbf{B}$ in the air gap between them, i.e., $B_\mathrm{gap} = A_m(g_{N2})\mathbf{B}$ with $A_m(g_{N2})$ being the amplification factor as a function of the gap. The magnetic energy in the sufficiently small air gap g_{N2} with volume $V = A \cdot g_{N2}$, where $A = W \cdot H$ is the facing pole area, is given by

$$\begin{aligned}E_\mathrm{gap} &= \frac{1}{2}\int_V B_\mathrm{gap} H_\mathrm{gap}\,\mathrm{d}V && (4.59)\\ &= \frac{A||\mathbf{B}||^2}{2\mu_0} g_{N2} A_m^2(g_{N2}), && (4.60)\end{aligned}$$

with $H_\mathrm{gap} = B_\mathrm{gap}/\mu_0$. From the energy, the force on the body (and on the hammer) is determined as

$$\begin{aligned}\mathbf{F}_\mathrm{M} &= F_\mathrm{M}\,\mathbf{e}_\mathrm{x} && (4.61)\\ &= -\frac{\mathrm{d}E_\mathrm{gap}}{\mathrm{d}g_{N2}}\,\mathbf{e}_\mathrm{x} && (4.62)\\ &= -\frac{A||\mathbf{B}||^2}{2\mu_0} A_m^2(g_{N2})\left(1 + \frac{2g_{N2}}{A_m(g_{N2})}\frac{\mathrm{d}A_m(g_{N2})}{\mathrm{d}g_{N2}}\right)\mathbf{e}_\mathrm{x}. && (4.63)\end{aligned}$$

The amplification factor $A_m(g_{N2})$ has been approximated from numerical experiments by Brugger and Paul [2010] as

$$A_m(g_{N2}) = \frac{c_g \mu_\mathrm{eff} + \tilde{g}_{N2}}{c_g + \tilde{g}_{N2}}. \quad (4.64)$$

Here $\tilde{g}_{N2}$ is the gap normalized with the total magnetic length of the device, i.e., $\tilde{g}_{N2} = g_{N2}/(L_H + L_B)$, and c_g is a geometry dependent fit factor. The effective permeability μ_eff is given by (2.36), and for the geometry dominant case we have $\mu_\mathrm{eff} = 1/n_x$, where again n_x must be calculated for the device with (magnetic) length $L_H + L_B$ (i.e., not the body or hammer only). Because the result has been derived from a numerical fit, the demagnetizing factor

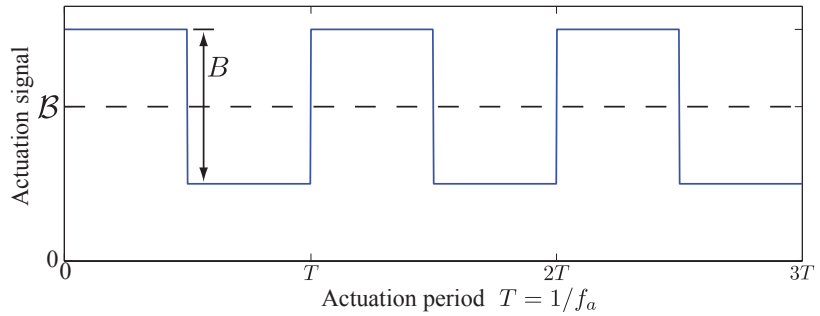

Figure 4.4: Schematic of the magnetic driving signal with peak-to-peak amplitude B and offset $\mathcal{B}$

$n_x =: n_{xB}$ used by Brugger and Paul [2010] has to be used. It is approximated by

$$n_{xB} = \tilde{W}\tilde{H}\left(\ln\left(\frac{4}{\tilde{W}+\tilde{H}}\right)-1\right), \tag{4.65}$$

where again $\tilde{(\cdot)}$ refers to the values normalized by the total magnetic length. We find $n_{xB} = 0.0687$.

Since a numerical fit has to be used in any case, we wish to simplify the force expression in (4.63) by replacing the expression in the brackets by a fit factor κ^2 and modify the amplification factor as

$$A_\kappa^2(g_{N2}) = \frac{c_g\mu_{\text{eff}} + \tilde{g}_{N2}}{(c_g+\tilde{g}_{N2})^2}. \tag{4.66}$$

This form has been found through observing the numerical fit with respect to FEM results as shown below. This modification results in the more compact force description

$$\mathbf{F}_{\text{M}} = -\frac{A||\mathbf{B}||^2}{2\mu_0}\kappa^2 A_\kappa^2(g_{N2})\mathbf{e}_{\text{x}} \tag{4.67}$$

For consistency with the previous chapter, we calculate the demagnetizing factor using the procedures from Beleggia et al. [2006] and find $n_x = 0.1161$.

The magnitude of the applied magnetic field $\mathbf{B}$ is a square wave signal with frequency f_a, peak-to-peak amplitude B and DC offset $\mathcal{B}$. It is shown in Fig. 4.4 and described mathematically by

$$||\mathbf{B}(t)|| = \frac{1}{2}B\Big(\operatorname{sgn}(\sin(2\pi f_a t)) + \mathcal{B}\Big), \tag{4.68}$$

where $\operatorname{sgn}(\cdot)$ is the signum function

$$\operatorname{sgn}(x) = \begin{cases} -1, & \text{for } x < 0 \\ 0, & \text{for } x = 0 \\ 1, & \text{for } x > 0 \end{cases}. \tag{4.69}$$

For $\mathcal{B} = 1$, (4.68) describes an on/off signal which is typically used in the experiments.

In conclusion, by inserting (4.68) in (4.67), we obtain the time-varying magnetic force between the body and he hammer as

$$\mathbf{F}_{\mathrm{M}}(g_{N2}, t) = \frac{A||\mathbf{B}(t)||^2}{2\mu_0}\kappa^2 A_\kappa^2(g_{N2})\,\mathbf{e}_{\mathrm{x}} \tag{4.70}$$

$$= \underbrace{\frac{AB^2}{8\mu_0}\kappa^2 A_\kappa^2(g_{N2})}_{:=F_M(g_{N2})} \Big(\operatorname{sgn}\left(\sin\left(2\pi f_a t\right)\right) + \mathcal{B}\Big)^2 \mathbf{e}_{\mathrm{x}} \tag{4.71}$$

and the influence of the shape only on the magnitude of the force can be analyzed with $\mathcal{B} = 1$ and $t = 0$ by normalizing as

$$\frac{8\mu_0||\mathbf{F}_{\mathrm{M}}||}{AB^2} = \kappa^2 A_\kappa^2(g_{N2}) \tag{4.72}$$

As for the exact amplification factor A_m, the normalization results in

$$\frac{8\mu_0||\mathbf{F}_{\mathrm{M}}||}{AB^2} = A_m^2(g_{N2})\left(1 + \frac{2g_{N2}}{A_m(g_{N2})}\frac{\mathrm{d}A_m(g_{N2})}{\mathrm{d}g_{N2}}\right). \tag{4.73}$$

To determine the fit parameters for both cases, we perform a finite element analysis (Ansoft Maxwell 3Dv13) with $\mu_r = 600$ as the permeability value for bulk nickel, i.e., sufficiently high to neglect the influence of the material, and the mass ratios $\alpha = \{0.5, 1, 1.5\}$. We have $n_x = 0.1161$ using Beleggia et al. [2006] and $n_{xB} = 0.0687$ using Brugger and Paul [2010].

The FE results, together with both fits are shown in Fig. 4.5(a). Both fits are excellent as shown by their goodness parameters, small root means square error (RMSE) and $R^2 \approx 1$, in 4.1 together with the fit parameters. The approximated version using κ (straight lines) has an RMS error half as big as the fit using the more complex version (dashed lines). Also, it predicts slightly better the area around the simulated equilibrium gap and the nonlinear behavior for smaller gaps. In addition it has a simpler form. Therefore, we will use this approximated version using κ for further analysis and the numerical implementation.

We observe in Fig. 4.5(a) that the curves are identical for identical mass ratios, and that they differ slightly for different mass ratios. This is an important result for experimental design, as it shows that as long as the magnetic volume is the same, the magnetic force between the body and the hammer will stay similar. This means that fabrication imperfections, resulting in slightly different magnetic volumes will still yield the same force between the body and the hammer and thus effects resulting from a different force can be excluded. In addition, the mass ratio can be neglected for an approximate force calculation. Also, since the mass influences the resonant frequency of the device, this result shows that the same magnetic force is obtained for different designs, as long as the total magnetic volume is kept constant.

	α	c_g	κ	RMSE	R^2
Brugger					
	0.5	0.105		16.00	0.982
	1	0.110		19.03	0.981
	1.5	0.108		18.29	0.981
κ **approx.**					
	0.5	0.027	2.823	7.032	0.997
	1	0.025	3.074	6.768	0.998
	1.5	0.025	3.028	6.740	0.998

Table 4.1: Fit parameters and goodness of fit values for the magnitude of the magnetic force

For $\alpha = 1$, and the corresponding values for c_g and κ, Fig. 4.5(b) shows (4.72) for various μ_r, showing the effect of the permeability of the material. As it is expected, lower permeability tend to lower forces.

4.3.3 Electrostatic Clamping Force

In the experimental setup, the substrate on which the microrobot is moving is patterned with a set of electrodes that can be set to a specific electrostatic potential. This results in charge separation in the gold frame of the robot, and consequently in an electrostatic clamping force $\mathbf{F}_\mathrm{C}$ that acts vertically on the body

$$\mathbf{F}_\mathrm{C} = -F_\mathrm{C}(t)\,\mathbf{e}_\mathrm{y}. \tag{4.74}$$

Similarly to the magnetic field, the applied potential is varied as an on/off signal which results in a square dependency of the force on the potential. In addition, the signal is shifted by a phase $\varphi \in [-\pi/2, \pi/2]$ with respect to the magnetic field, or

$$F_\mathrm{C}(t) = F_\mathrm{Co}\Big(\operatorname{sgn}\left(\sin\left(2\pi f_a t + \varphi\right)\right) + 1\Big)^2. \tag{4.75}$$

The actual numerical value of F_Co is not of interest. In the simulations it is chosen sufficiently high ($F_\mathrm{Co} = 1\mathrm{N}$), such that the body sticks to the substrate, i.e., it is immobile. The effect for lower values, i.e., when the body is still moving, can be examined by varying the parameter β in (4.52).

Experimental Findings

Vollmers et al. [2008] and Frutiger et al. [2010] describe the effect of clamping as to smoothen the velocity of the robot. In addition, it was determined experimentally that a phase shift of $\varphi = \pm\pi/2$ changed the sign of the direction of the velocity of the robot. It was also found, that, contrary to initial thoughts, clamping is not necessary for the motion. We will discuss these findings further in our numerical results in Section 4.6.

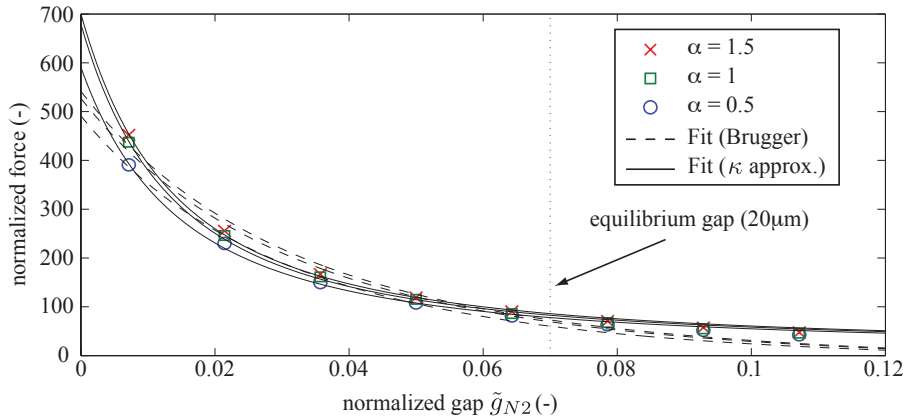

(a) Each curve (or symbol dataset) represents the identical results for different applied fields $B \in \{1, 3, 5\}$mT. Both fits are very satisfactory. We use the approximated version using κ due to its simpler description and because it captures the data around the equilibrium gap and the non-linear transition at small gaps somewhat better.

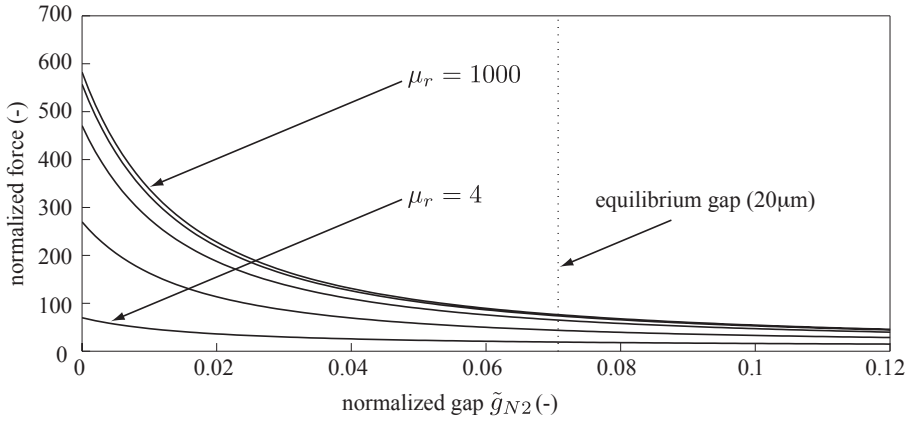

(b) As expected, lower permeabilities will result in lower forces

Figure 4.5: (a) Normalized magnetic force for different mass ratios α. (b) Normalized magnetic force for different permeabilities $\mu_r = \{0.4, 15, 63, 251, 1000\}$. ($\alpha = 1$). In both figures, the dotted vertical line represents the equilibrium gap (20μm) used in the numerical simulations.

4.4 A Linear Model for the Dynamics

Before solving the equations of motion numerically, we analyze the equations of motions of the WRMMA analytically and derive its characteristic parameters. After stating the assumptions for the analysis, we derive the equations of motion. Then, we give their solution for sticktion, stick↔slip transitions and sliding.

4.4.1 Assumptions

1. no damping, i.e., $c = 0$, to keep the equations simple, but also because experimentally c has been found very small
2. no clamping, i.e., $F_{\mathrm{Co}} = 0$, to focus on the natural motion principle
3. small oscillations, i.e., $g_{N2} \approx g_0$
4. sinusoidal magnetic field, i.e.,

$$||\mathbf{B}(t)|| = \frac{1}{2}B\Big(\frac{4}{\pi}\sin(2\pi f_a t) + \mathcal{B}\Big). \tag{4.76}$$

A consequence of assumption 3 is that impact between the body and the hammer is not considered. In addition, the amplitude of the magnetic force can be assumed independent of the gap and constant, i.e.,

$$F_M(g_{N2}) \approx F_M(g_0) =: F_0. \tag{4.77}$$

The justification of assumption 4 lays in the Fourier expansion of a square wave: a square wave can be described by $\mathrm{sgn}(\sin(2\pi f_a t))$ whose Fourier expansion is

$$\mathrm{sgn}(\sin(2\pi f_a t)) = \frac{4}{\pi}\sum_{k=1}^{\infty}\frac{\sin((2k-1)2\pi f_a t)}{2k-1} \tag{4.78}$$

$$= \frac{4}{\pi}\left(\sin(2\pi f_a t) + \frac{1}{3}\sin(6\pi f_a t) + \cdots\right). \tag{4.79}$$

Using only the first term of the expansion is a necessary simplification to treat the problem analytically with reasonable effort. Also, since the magnetic field is squared to calculate the force, higher order terms would give rise to higher order harmonics with small, and thus negligible, amplitudes. The resulting force is obtained as (dropping the unit vector $\mathbf{e}_{\mathrm{x}}$)

$$\mathbf{F}_{\mathrm{M}}(t) = \underbrace{\frac{AB^2}{8\mu_0}\kappa^2 A_\kappa^2(g_0)}_{:=F_0}\underbrace{\left(\frac{4}{\pi}\sin(2\pi f_a t) + \mathcal{B}\right)^2}_{:=f(t)} \tag{4.80}$$

$$= F_0\left(\frac{4}{\pi}\sin(2\pi f_a t) + \mathcal{B}\right)^2 \tag{4.81}$$

$$= F_0\left(\mathcal{B}^2 + 2\frac{4}{\pi}\mathcal{B}\sin(2\pi f_a t) + \frac{16}{\pi^2}\sin^2(2\pi f_a t)\right) \tag{4.82}$$

$$= F_0\left(\mathcal{B}^2 + \frac{8}{\pi^2} + \frac{8}{\pi}\mathcal{B}\sin(2\pi f_a t) - \frac{8}{\pi^2}\sin(4\pi f_a t + \pi/2)\right) \tag{4.83}$$

where in the last equality we have used the trigonometric identity $\sin^2(x) = \frac{1}{2}(1-\cos(2x)) = \frac{1}{2}(1-\sin(2x+\pi/2))$.

4.4.2 Equations of Motion

In general, when both the body and the hammer are moving, the system is described by the following system of two coupled second order differential equations

$$\begin{cases} m_B\ddot{x}_1(t) = F_S + F_M(t) + F_T(\dot{x}_1(t)) \\ m_H\ddot{x}_2(t) = -F_S - F_M(t) \end{cases} \tag{4.84}$$

where the dot designates differentiation with respect to time, m_B and $m_H = \alpha m_B$ are the mass of the body and the hammer respectively, F_S is the spring force and F_M the magnetic force (see Section 4.3). The friction force F_T is described by an inclusion

$$F_T(\dot{x}_1) \in -\mu F_G \operatorname{sgn}(\dot{x}_1) \tag{4.85}$$

or, equivalently

$$F_T(\dot{x}_1) = \begin{cases} -\mu F_G, & \dot{x}_1 > 0 \\ [-1,1]\mu F_G & \dot{x}_1 = 0 \\ \mu F_G, & \dot{x}_1 < 0 \end{cases}. \tag{4.86}$$

with $F_G = \beta m_T g$ from (4.51).

The advantage of the set-valued force law is now apparent. If the sgn function is regularized, or smoothened, by some arctan function to obtain an equation rather than an inclusion, the slope around $\dot{x}_1 = 0$ will be very steep causing numerically stiff equations. In addition, and worse, the body can practically never stick, and hence the physics are not correctly modeled. In contrast, a set-valued friction law as (4.86) allows us to clearly define the motion states and the transition conditions as follows

$$\dot{x}_1 = 0 \Rightarrow \begin{cases} \text{body sticks as long as } |F_T| < \mu F_G \\ \quad \text{body sticks until } |F_T| = \mu F_G \text{ (stick}\rightarrow\text{slip transition)} \end{cases} \tag{4.87}$$

$$\dot{x}_1 \neq 0 \Rightarrow \begin{cases} \text{body slides as long as } \dot{x}_1 \neq 0 \\ \quad \text{body slides until } \dot{x}_1 = 0 \text{ (slip}\rightarrow\text{stick transition)} \\ \quad\quad \textit{or} \\ \quad \text{body keeps sliding: } \dot{x}_1 \neq 0 \\ \text{body switches velocity (forward}\leftrightarrow\text{backward slip transition)} \end{cases} \tag{4.88}$$

Using (4.54) for F_S, and the mass ratio $\alpha = m_H/m_B$, the system (4.84) can be rewritten as

$$\begin{cases} m_H\ddot{x}_1(t) = \alpha k(x_2(t) - x_1(t) - g_0) + \alpha F_M(t) + \alpha F_T(\dot{x}_1(t)) \\ m_H\ddot{x}_2(t) = -k(x_2(t) - x_1(t) - g_0) - F_M(t) \end{cases} \tag{4.89}$$

where k is the stiffness of the spring, and g_0 the rest gap of the spring. We now define

$$s(t) \coloneqq x_1(t) + x_2(t), \text{ and } d(t) \coloneqq x_2(t) - x_1(t) - g_0. \tag{4.90}$$

Inversely, we have of course $x_1(t) = \frac{1}{2}(s(t) - d(t))$, $\dot{x}_1 = \frac{1}{2}(\dot{s}(t) - \dot{d}(t))$, and $\ddot{x}_1 = \frac{1}{2}(\ddot{s}(t) - \ddot{d}(t))$, and similarly for $x_2(t), \dot{x}_2(t)$ and $\ddot{x}_2(t)$. With these definitions, the system now reads

$$\begin{cases} m_H \ddot{s}(t) = (\alpha - 1)kd(t) + (\alpha - 1)F_{\mathrm{M}}(t) + \alpha F_{\mathrm{T}}(\dot{s}(t) - \dot{d}(t)) \\ m_H \ddot{d}(t) = -(\alpha + 1)kd(t) - (\alpha + 1)F_{\mathrm{M}}(t) - \alpha F_{\mathrm{T}}(\dot{s}(t) - \dot{d}(t)) \end{cases}, \tag{4.91}$$

or, written as a second order differential inclusion system

$$\begin{cases} m_H \ddot{s}(t) - (\alpha - 1)kd(t) \in (\alpha - 1)F_{\mathrm{M}}(t) - \alpha\mu F_{\mathrm{G}} \operatorname{sgn}(\dot{s}(t) - \dot{d}(t)) \\ m_H \ddot{d}(t) + (\alpha + 1)kd(t) \in -(\alpha + 1)F_{\mathrm{M}}(t) + \alpha\mu F_{\mathrm{G}} \operatorname{sgn}(\dot{s}(t) - \dot{d}(t)) \end{cases}. \tag{4.92}$$

Noting that $F_{\mathrm{M}}(t) = F_0 f(t)$ (see (4.80)), we now introduce the non-dimensional parameters σ, δ, τ and η, and the characteristic variables s_c, d_c, and t_c as

$$t = t_c\tau, \qquad s(t) = s_c\sigma(\tau), \qquad d(t) = d_c\delta(\tau), \qquad \eta = \frac{d_c}{s_c}, \tag{4.93}$$

with

$$\frac{1}{t_c} = \sqrt{\frac{k}{m_H}} = \omega_1 = 2\pi f_1, \qquad d_c = \frac{F_0}{k}, \quad \text{and} \quad \eta = \frac{F_0}{\mu F_{\mathrm{G}}}, \tag{4.94}$$

where ω_1 and f_1 are the natural frequency of the hammer-spring oscillator (keeping the body fixed or tethered) in rad/s and Hz respectively. The characteristic displacement d_c represents the change of the gap given the magnetic force and the spring since $F_0 = kd_c$. Finally, η is a non-dimensional parameter representing the ratio of the maximal magnetic force to the maximal friction force.

By substituting (4.93)—(4.94) into (4.92), noting that

$$\frac{\mathrm{d}(\,\cdot\,)}{\mathrm{d}t} = \frac{1}{t_c}\frac{\mathrm{d}(\,\cdot\,)}{\mathrm{d}\tau}, \text{ and } \quad \frac{\mathrm{d}^2(\,\cdot\,)}{\mathrm{d}t^2} = \frac{1}{t_c^2}\frac{\mathrm{d}(\,\cdot\,)}{\mathrm{d}\tau}, \tag{4.95}$$

and observing that

$$\operatorname{sgn}\left(\frac{\mathrm{d}s(t)}{\mathrm{d}t} - \frac{\mathrm{d}d(t)}{\mathrm{d}t}\right) = \operatorname{sgn}\left(\frac{s_c}{t_c}\frac{\mathrm{d}\sigma(\tau)}{\mathrm{d}\tau} - \frac{d_c}{t_c}\frac{\mathrm{d}\delta(\tau)}{\mathrm{d}\tau}\right) \tag{4.96}$$

$$= \operatorname{sgn}\left(\frac{\mathrm{d}\sigma(\tau)}{\mathrm{d}\tau} - \eta\frac{\mathrm{d}\delta(\tau)}{\mathrm{d}\tau}\right), \tag{4.97}$$

we can non-dimensionalize the system (4.92). For this, we note that for the remainder of this section, a dot $\dot{(\,)}$ represents differentiation with respect to the non-dimensional time τ. We find

$$\begin{cases} \ddot{\sigma}(\tau) - (\alpha - 1)\eta\delta(\tau) \in (\alpha - 1)\eta f(\tau) - \alpha \operatorname{sgn}(\dot{\sigma}(\tau) - \eta\dot{\delta}(\tau)) \\ \ddot{\delta}(\tau) + (\alpha + 1)\delta(\tau) \in -(\alpha + 1)f(\tau) + \dfrac{\alpha}{\eta} \operatorname{sgn}(\dot{\sigma}(\tau) - \eta\dot{\delta}(\tau)) \end{cases} \tag{4.98}$$

and with the non-dimensional actuation frequency $\tilde{f} := f_a / f_1$, we have

$$f(\tau) = \left(\frac{4}{\pi} \sin\left(2\pi f_a t_c \tau\right) + \mathcal{B} \right)^2 \tag{4.99}$$

$$= \left(\frac{4}{\pi} \sin\left(\frac{f_a}{f_1}\tau\right) + \mathcal{B} \right)^2 \tag{4.100}$$

$$= \left(\frac{4}{\pi} \sin\left(\tilde{f}\tau\right) + \mathcal{B} \right)^2. \tag{4.101}$$

The non-dimensional system states and stick↔slip conditions equivalent to (4.87) and are (4.88)

$$\dot{\sigma} = \eta\dot{\delta} \Rightarrow \begin{cases} \text{body sticks as long as } |F_{\mathrm{T}}| < \dfrac{1}{\eta} F_0 \\ \qquad \text{body sticks until } |F_{\mathrm{T}}| = \dfrac{1}{\eta} F_0 \text{ (stick→slip transition)} \end{cases} \tag{4.102}$$

$$\dot{\sigma} \neq \eta\dot{\delta} \Rightarrow \begin{cases} \text{body slides as long as } \dot{\sigma} \neq \eta\dot{\delta} \\ \qquad \text{body slides until } \dot{\sigma} = \eta\dot{\delta} \text{ (slip→stick transition)} \\ \qquad\qquad \textit{or} \\ \quad \text{body keeps sliding: } \dot{\sigma} \neq \eta\dot{\delta} \\ \text{body switches velocity (forward↔backward slip transition)} \end{cases} \tag{4.103}$$

In conclusion, the dynamics of the system are described by the second order non-dimensional differential inclusion system (4.98) with the non-dimensional parameters α, η and $\tilde{f}$.

Note, that η is a key parameter for the design and actuation of the system; on the one hand the magnetic force depends amongst others on the material, the geometry of the device and the actuation field strength. On the other hand, the maximal friction force strongly depends on the environmental conditions such as surface roughness or humidity.

This finding illustrates that as long as the non-dimensional parameters remain constant, the effects of individual parameters on the overall performance of the system, say the velocity of the robot, may compensate each other. Thus, care must be taken during the experimental investigation to isolate individual effects. Of course, the mathematical model allows more insight at the cost of simplification.

We now further investigate the special cases of sticktion and stick→slip transition.

4.4.3 Solution for Sticktion

During sticktion, we have $\dot{\sigma}(\tau) = \eta\dot{\delta}(\tau)$, thus $\operatorname{sgn}(\dot{\sigma}(\tau) - \eta\dot{\delta}(\tau)) = 0$. Substituting this into (4.98) eliminates the set-valued parts and yields two equations

$$\begin{cases} \ddot{\delta}(\tau) - (\alpha - 1)\delta(\tau) = (\alpha - 1)f(\tau) \\ \ddot{\delta}(\tau) + (\alpha + 1)\delta(\tau) = -(\alpha + 1)f(\tau) \end{cases} \tag{4.104}$$

and we can sum up both equations to reduce the system to a single equation

$$\ddot{\delta}(\tau) + \delta(\tau) = -f(\tau) \Leftrightarrow \ddot{\delta}(\tau) = -\delta(\tau) - f(\tau) \tag{4.105}$$

which represents a forced oscillation with driving force $-f(\tau)$. For its solution, we rewrite the driving force to bring it into standard form. With (4.83) written in non-dimensional form, we have

$$-f(t) = -\left(\mathcal{B}^2 + \frac{8}{\pi^2} + \frac{8}{\pi}\mathcal{B}\sin(2\pi f_a t) - \frac{8}{\pi^2}\sin(4\pi f_a t + \pi/2)\right) \tag{4.106}$$

$$= -\left(\mathcal{B}^2 + \frac{8}{\pi^2}\right) - \frac{8}{\pi}\mathcal{B}\sin(\tilde{f}\tau) + \frac{8}{\pi^2}\sin(2\tilde{f}\tau + \pi/2) \tag{4.107}$$

$$= \underbrace{-\left(\mathcal{B}^2 + \frac{8}{\pi^2}\right)}_{:=A_0} + \underbrace{\frac{8}{\pi}}_{:=A_1}\mathcal{B}\sin(\tilde{f}\tau + \pi) + \underbrace{\frac{8}{\pi^2}}_{:=A_2}\sin(2\tilde{f}\tau + \pi/2) \tag{4.108}$$

where in the last equation we have used that $-\sin(x) = \sin(x + \pi)$. With a coordinate shift $q(\tau) := \delta(\tau) - A_0$ we obtain the standard equation of a driven oscillator as

$$\ddot{q}(\tau) + q(\tau) = \sum_{n=1}^{2} A_n \sin(n\tilde{f}\tau + \pi/n) \tag{4.109}$$

Since linear superposition holds, the solution $q(\tau)$ is the sum of the solutions to the individual excitations of the system, i.e.,

$$q(\tau) = q_1(\tau) + q_2(\tau) \tag{4.110}$$

where the $q_n(\tau)$ are the solutions of

$$\ddot{q}_n(\tau) + q_n(\tau) = A_n \sin(n\tilde{f}\tau + \pi/n), \qquad n = 1, 2. \tag{4.111}$$

They are found to be

$$q_n(\tau) = \frac{A_n}{n\tilde{f}Q_n}\sin(n\tilde{f}\tau + \pi/n - \varphi_n), \qquad n = 1, 2, \tag{4.112}$$

where φ_n is the phase-shift of the response with respect to the driving phase that can be approximated for driven oscillators without damping as

$$\varphi_n(\tilde{f}) = \lim_{\nu \to 0} \arctan\left(\frac{\nu}{1 - (n\tilde{f})^2}\right). \tag{4.113}$$

In (4.112) the Q_n are given by

$$Q_n = \frac{1}{n\tilde{f}} \left|1 - (n\tilde{f})^2\right| \iff n\tilde{f}Q_n = \left|1 - (n\tilde{f})^2\right|. \tag{4.114}$$

Finally, the solution is found substituting (4.114) into (4.112), by summing up the $q_n(\tau)$ and by changing back to the original variable $\delta(\tau) = q(\tau) + A_0$ as

$$\delta(\tau) = A_0 + \sum_{n=1}^{2} \frac{A_n}{\left|1 - (n\tilde{f})^2\right|} \sin(n\tilde{f}\tau + \pi/n - \varphi_n), \tag{4.115}$$

for $n = 1, 2$. We observe resonant behavior for $\tilde{f} \to 1/n$, i.e., the amplitudes of the sin terms grow to infinity and $\varphi_n(\tilde{f} \to 1/n) \to \pi/2$.

In conclusion, (4.115) describes the motion of the WRMMA, during sticktion, i.e., the oscillation of the hammer. The numerical approximations of the A_n are

$$A_0 = -\left(\mathcal{B}^2 + \frac{8}{\pi^2}\right) \approx -\left(\mathcal{B}^2 + 0.81\right) \tag{4.116}$$

$$A_1 = \frac{8}{\pi}\mathcal{B} \approx 2.55\mathcal{B} \tag{4.117}$$

$$A_2 = \frac{8}{\pi^2} \approx 0.81 \tag{4.118}$$

4.4.4 Frequency Range for Sticktion→Sliding Transition

We now derive the conditions on the driving frequency $\tilde{f}$ to transition the system from pure sticktion to a sliding behavior, and thus to actual propulsion. The solution for sticktion, the inclusions (4.104), can be written as inequalities and read

$$\begin{cases} \left|\ddot{\delta}(\tau) - (\alpha - 1)\delta(\tau) - (\alpha - 1)f(\tau)\right| < \dfrac{\alpha}{\eta} \\ \left|\ddot{\delta}(\tau) + (\alpha + 1)\delta(\tau) + (\alpha + 1)f(\tau)\right| < \dfrac{\alpha}{\eta} \end{cases}, \tag{4.119}$$

where the $|\cdot|$ takes care of both negative and positive transitions, and the system remains in sticktion as long as these conditions are fulfilled. Substituting the oscillator equation (4.105) into the inequalities yields the same sticktion condition

$$\left|\delta(\tau) + f(\tau)\right| < \frac{1}{\eta}, \tag{4.120}$$

which is independent of the mass ratio α. Now, we can insert the solution for $\delta(\tau)$, (4.115), into the condition and find

$$\left|A_0 + \sum_{n=1}^{2} \frac{A_n}{\left|1 - (n\tilde{f})^2\right|} \sin(n\tilde{f}\tau + \pi/n - \varphi_n) + f(\tau)\right| < \frac{1}{\eta}, \tag{4.121}$$

with $n = 1, 2$. Now, rather than attempting to solve this condition for $\tilde{f}$ in general, we observe that for $1 - (n\tilde{f})^2 \to 0$, that is, for $\tilde{f}$ sufficiently close to $1/n$, the term $A_n / \left|1 - (n\tilde{f})^2\right|$ will dominate the expression on the left as it

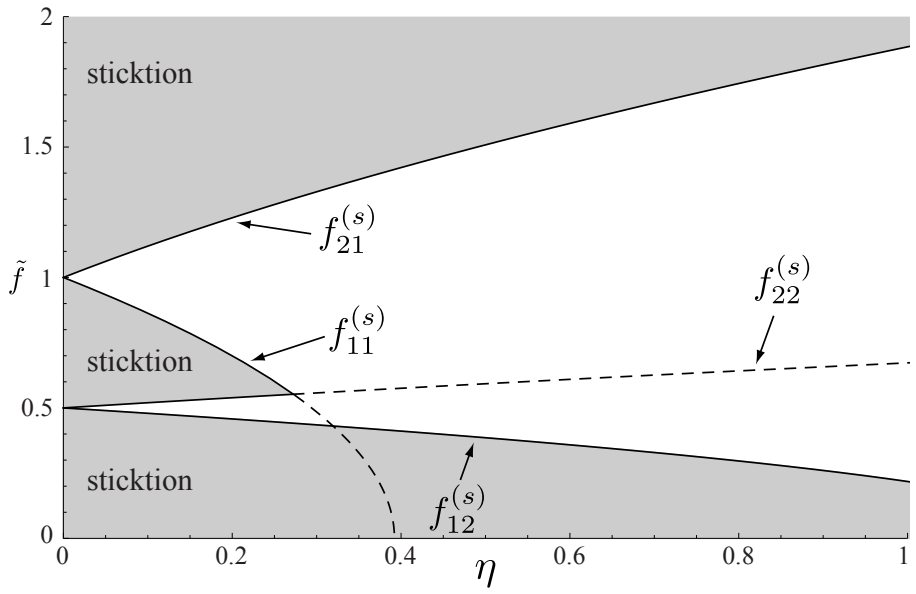

Figure 4.6: Frequency range for sticktion

tends towards infinity. Then, because $|\sin(x)| \leq 1 \, \forall x$, the condition reduces to

$$\frac{A_n}{\left|1-(n\tilde{f})^2\right|} < \frac{1}{\eta} \Longleftrightarrow \left|1-(n\tilde{f})^2\right| > \eta A_n \tag{4.122}$$

$$\Longleftrightarrow \begin{cases} 1-(n\tilde{f})^2 > \eta A_n \\ 1-(n\tilde{f})^2 < -\eta A_n \end{cases}, \quad n = 1,2. \tag{4.123}$$

which finally yields the sticktion conditions on $\tilde{f}$ as

$$\tilde{f} < \sqrt{\frac{1-\eta A_n}{n^2}} =: f_{1n}^{(s)} \tag{4.124}$$

and

$$\tilde{f} > \sqrt{\frac{1+\eta A_n}{n^2}} =: f_{2n}^{(s)} \tag{4.125}$$

for $n = 1,2$. Figure 4.6 shows the sticktion areas in the $\tilde{f} - \eta$ diagram for $\mathcal{B} = 1$. For $\tilde{f}$ in the vicinity of $1/n$, the system will remain in sticktion if $\tilde{f} < f_{1n}^{(s)}$ or if $\tilde{f} > f_{2n}^{(s)}$. If these conditions are not fulfilled, the system transitions into sliding. Thus, we have related a key parameter of the system, η, to the frequency ranges at which the WRMMA will move, and because $A_n = A_n(\mathcal{B})$, also to DC offset $\mathcal{B}$ of the actuation signal.

Also, note that the limit $f_{1n}^{(s)}$ only exists if

$$1 - \eta A_n \geq 0 \Leftrightarrow \eta \leq \frac{1}{A_n}, \qquad n = 1,2. \tag{4.126}$$

For $n = 1$, we have $1/A_1 \approx 0.39/\mathcal{B}$, and the existence condition yields

$$\eta = \frac{F_0}{\mu F_G} \leq \frac{0.39}{\mathcal{B},} \tag{4.127}$$

in other words, for the typically value $\mathcal{B} = 1$, the limit exists for maximal magnetic forces that are less than half of the maximal friction force.

To conclude, conditions (4.124) and (4.125) capture the most important parameters of the system, and allow for successful design and actuation.

4.4.5 Solution for Sliding

During sliding we have $\dot{\sigma}(\tau) > \eta\dot{\delta}(\tau)$ or $\dot{\sigma}(\tau) < \eta\dot{\delta}(\tau)$, the friction force is maximal, and thus the inclusion system can be written as a system of differential equations

$$\begin{cases} \ddot{\sigma}(\tau) - (\alpha-1)\eta\delta(\tau) + \gamma\alpha = (\alpha-1)\eta f(\tau) \\ \ddot{\delta}(\tau) + (\alpha+1)\delta(\tau) - \gamma\dfrac{\alpha}{\eta} = -(\alpha+1)f(\tau) \end{cases} \tag{4.128}$$

with $\gamma := \operatorname{sgn}(\dot{\sigma}(\tau) - \eta\dot{\delta}(\tau)) = \pm 1$.

For the solution of the system (4.128), we note that the second equation does not involve $\sigma(\tau)$, and that it describes again a driven linear oscillator. Therefore, the solution for $\delta(\tau)$ has the same form as in the case for pure sticktion. Inspired by its solution (4.115), we describe $\delta(\tau)$ with two frequency components as

$$\delta(\tau) = a_0 + \sum_{n=1}^{2} a_n \sin(n\tilde{f}\tau + \pi/n - \phi_n), \tag{4.129}$$

and unknowns a_0, a_n and ϕ_n for $n = 1, 2$. We have for the second derivative

$$\ddot{\delta}(\tau) = -\sum_{n=1}^{2} \left(n\tilde{f}\right)^2 a_n \sin(n\tilde{f}\tau + \pi/n - \phi_n). \tag{4.130}$$

Then, from (4.108) we have

$$-f(t) = A_0 + \sum_{n=1}^{2} A_n \sin(n\tilde{f}\tau + \pi/n), \tag{4.131}$$

and inserting (4.129)—(4.131) into the second equation of (4.128) allows to identify the unknown coefficients a_n as

$$a_0 = A_0 - \frac{\gamma}{\eta}\frac{1}{1+\frac{1}{\alpha}}, \text{ and} \tag{4.132}$$

$$a_n = \frac{1}{1 - \left(\frac{n\tilde{f}}{\sqrt{1+\alpha}}\right)^2} A_n, \tag{4.133}$$

and the phase shift can be approximated as

$$\phi_n(\tilde{f}) = \lim_{\nu \to 0} \arctan\left(\frac{\nu}{1 - \left(\frac{n\tilde{f}}{\sqrt{1+\alpha}}\right)^2} \right). \tag{4.134}$$

As in the sticktion case, we observe the possibility for resonant behavior. But opposed to the sticktion case, where resonance occurs for $\tilde{f} \approx 1/n$, during sliding, resonance occurs for

$$\tilde{f} \approx \frac{\sqrt{1+\alpha}}{n}, \tag{4.135}$$

that is, increased by the factor $\sqrt{1+\alpha}$. This is consistent with the fact that a symmetrical two mass spring oscillator ($\alpha = 1$) has a resonant frequency at $\tilde{f} = \sqrt{2}$.

It is important that the coefficients of the periodic terms in (4.129), i.e., a_1 and a_2 are not dependent on the motion direction of the device, since γ is not appearing in the expressions. This means that they are not influenced by the current motion direction of the body.

We now turn to investigate $\ddot{\sigma}(\tau)$, noting that the actual solution of $\sigma(\tau)$ is of little interest. Rather, we turn to investigate the expression $\frac{1}{2}\left(\ddot{\sigma}(t) - \eta\ddot{\delta}(\tau)\right)$, that is, the acceleration of the body. From (4.128), we have

$$\ddot{\sigma}(\tau) = (\alpha - 1)\eta\delta(\tau) + (\alpha - 1)\eta f(\tau) - \gamma\alpha \tag{4.136}$$

$$= (\alpha - 1)\eta\Big(\delta(\tau) + f(\tau)\Big) - \gamma\alpha \tag{4.137}$$

and

$$-\eta\ddot{\delta}(\tau) = (\alpha + 1)\eta\Big(\delta(\tau) + f(\tau)\Big) - \gamma\alpha, \tag{4.138}$$

and, thus, finally

$$\frac{1}{2}\left(\ddot{\sigma}(t) - \eta\ddot{\delta}(\tau)\right) = \alpha\eta\Big(\delta(\tau) + f(\tau)\Big) - \gamma\alpha. \tag{4.139}$$

Now, knowing that the solutions for $\delta(\tau)$ and $f(\tau)$ are periodic, their sum is periodic as well, and takes the form

$$\delta(\tau) + f(\tau) = g_0 + \sum_{n=1}^{2} g_n \sin(n\tilde{f}\tau + \beta_n), \tag{4.140}$$

with unknowns g_n, $g_0 = a_0 - A_0$, and with (4.132) we have

$$g_0 = -\frac{\gamma}{\eta}\frac{\alpha}{\alpha + 1}. \tag{4.141}$$

Inserting (4.141) and (4.140) into (4.139), we find after some manipulations

$$\frac{1}{2}\left(\ddot{\sigma}(t) - \eta\ddot{\delta}(\tau)\right) = -\gamma\alpha\frac{2\alpha + 1}{\alpha + 1} + \alpha\eta\sum_{n=1}^{2} g_n \sin(n\tilde{f}\tau + \beta_n). \tag{4.142}$$

This expression allows for the following interpretation: There are two forces acting on the body, a constant and a periodic one. The constant force depends only on the mass ratio α, represents frictional effects as its direction is opposed to the velocity of the body (because of the $-\gamma$ term) and thus effectively decelerates the body. On the other hand, the periodic force depends (in addition to α) on the maximal magnetic force and maximal friction force (through η) and indirectly on the spring through $\tilde{f}\tau$. It does not depend on γ and can thus both accelerate and decelerate the body.

4.4.6 Summary of the Linear Model

In summary, we have derived the following non-dimensional and characteristic parameters to describe the motion of the device:

Characteristic time t_c relating the mass of the hammer and the spring through the natural frequency $t_c = 1/\omega_1 = \sqrt{m_H/k}$. t_c is of course the natural period of the oscillator.

Characteristic (relative) displacement d_c for given spring and magnetic force

Non-dimensional time $\tau = t/t_c$ **and frequency** $\tilde{f} = f_a/f_1$ allowing to compare different designs

Non-dimensional coordinates $\sigma(\tau)$ **and** $\delta(\tau)$ to describe the kinematics of the device

Ratio of maximal magnetic to maximal friction force η that allows to derive actuation frequency limits in case of sliding, $\eta = F_0/(\mu F_G)$

It is interesting that some of these parameters are pure design parameters, such as the characteristic time t_c, while others are both design and actuation parameters, such as the characteristic displacement d_c. The ratio η relates magnetic and friction force, both being design and actuation parameters, since the magnetic force depends on the geometry of the magnetic bodies as well as on the applied field strength, and the friction force depends on the properties of the involved surfaces, but may also be varied through clamping.

The presented analytical model, especially the conditions for the transition of complete sticktion to sliding, are valid in the vicinity of $\tilde{f} \approx 1$. For the complete frequency range, a numerical investigation is indispensable and the subject of the next section.

4.5 Numerical Model for the Dynamics

To solve the equations of motion of the WRMMA without assumptions, we use the non-smooth dynamics approach as described in Section 4.2. This approach provides a mathematically sound formalism for the dynamics of rigid bodies with set-valued interaction laws for the description of unilateral contact, friction and impact.

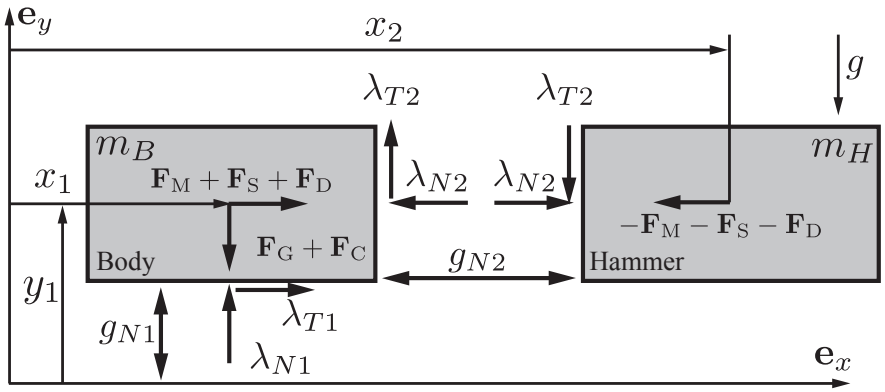

Figure 4.7: Free body diagram of the WRMMA.

As mentioned, the numerical integration is performed using a mid-point time-stepping method introduced by Moreau [1988], discretizing the equality of measures

$$\mathbf{M}\mathrm{d}\mathbf{u} - \mathbf{h}(\mathbf{q},\mathbf{u},t)\mathrm{d}t - \sum \mathbf{w}_{Ni}\mathrm{d}P_{Ni} - \sum \mathbf{w}_{Ti}\mathrm{d}P_{Ti} = \mathbf{0}, \tag{4.143}$$

which is a combined description of the non-impulsive and impulsive motion. In the following we describe the individual terms of (4.143).

Figure 4.7 recalls the free body diagram of the WRMMA consisting of the body with coordinates (x_1, y_1) and the hammer with coordinate x_2. The generalized coordinates and the associated velocities are

$$\mathbf{q} = \begin{pmatrix} x_1 & y_1 & x_2 \end{pmatrix}^\mathrm{T}, \qquad \mathbf{u} = \begin{pmatrix} v_{x,1} & v_{y,1} & v_{x,2} \end{pmatrix}^\mathrm{T} \tag{4.144}$$

with $\dot{\mathbf{q}} = \mathbf{u}$ for almost all t. The system has a frictional contact between the body and the floor with a gap g_{N1}. We assume that this contact always remains closed, i.e., $g_{N1} = 0$, and, therefore, consider it to be a frictional bilateral contact with sliding velocity $\gamma_{T1}(\mathbf{u}) = v_{x,1}$ and friction coefficient μ. Furthermore, there is a frictionless unilateral contact between the body and the hammer with gap $g_{N2} \geq 0$ and restitution coefficient ε. The matrices $\mathbf{W}_N = \begin{pmatrix} \mathbf{w}_{N1} & \mathbf{w}_{N2} \end{pmatrix}$ and $\mathbf{W}_T = \begin{pmatrix} \mathbf{w}_{T1} & \mathbf{w}_{T2} \end{pmatrix}$ of generalized force directions are

$$\mathbf{W}_N = \begin{pmatrix} 0 & 1 & 0 \\ -1 & 0 & 1 \end{pmatrix}^\mathrm{T}, \qquad \mathbf{W}_T = \begin{pmatrix} 1 & 0 & 0 \\ 0 & 1 & 0 \end{pmatrix}^\mathrm{T}. \tag{4.145}$$

The mass matrix $\mathbf{M} = \mathrm{diag}\,(m_B, m_B, m_H)$ is constant and the vector $\mathbf{h}$ of the non-contact forces is composed of the gravitational force $\mathbf{F}_\mathrm{G}$, the clamping force $\mathbf{F}_\mathrm{C}$, the spring force $\mathbf{F}_\mathrm{S}$, damping $\mathbf{F}_\mathrm{D}$ and magnetic force $\mathbf{F}_\mathrm{M}$ between the body and the hammer; i.e.,

$$\mathbf{h} = \mathbf{F}_\mathrm{G} + \mathbf{F}_\mathrm{C} + \mathbf{F}_\mathrm{D} + \mathbf{F}_\mathrm{M}, \tag{4.146}$$

which have been derived in Section 4.3 as

$$\mathbf{F}_{\mathrm{G}} = \begin{pmatrix} 0 & -\beta(m_B + m_H)g & 0 \end{pmatrix}^{\mathrm{T}}, \tag{4.147}$$

$$\mathbf{F}_{\mathrm{S}}(x_1, x_2) = \begin{pmatrix} -k(x_2 - x_1 - g_0) & 0 & k(x_2 - x_1 - g_0) \end{pmatrix}^{\mathrm{T}}, \tag{4.148}$$

$$\mathbf{F}_{\mathrm{D}}(v_{x,1}, v_{x,2}) = \begin{pmatrix} c(v_{x,2} - v_{x,1}) & 0 & -c(v_{x,2} - v_{x,1}) \end{pmatrix}^{\mathrm{T}}, \tag{4.149}$$

$$\mathbf{F}_{\mathbf{m}}(g_{N2}, t) = \begin{pmatrix} f_m(g_{N2}, t) & 0 & -f_m(g_{N2}, t) \end{pmatrix}^{\mathrm{T}} \tag{4.150}$$

$$\mathbf{F}_{\mathbf{c}}(t) = \begin{pmatrix} 0 & -f_c(t) & 0 \end{pmatrix}^{\mathrm{T}}. \tag{4.151}$$

with

$$f_m(g_{N2}, t) = \frac{AB^2}{8\mu_0}\kappa^2 A_\kappa^2(g_{N2})\Big(\operatorname{sgn}\left(\sin\left(2\pi f_a t\right)\right) + \mathcal{B}\Big)^2 \tag{4.152}$$

$$f_c(t) = F_{\mathrm{Co}}\Big(\operatorname{sgn}\left(\sin\left(2\pi f_a t + \varphi\right)\right) + 1\Big)^2. \tag{4.153}$$

and $\mathcal{B} = 1$ unless otherwise specified.

4.5.1 Numerical Integration Procedure

The midpoint integration scheme is implemented in MATLAB to find the velocity and the position of both the body and the hammer. The integration is performed by sweeping over system parameters such as the actuation frequency f_a. In these parameter sweeps, the initial conditions at a specific frequency are the results of the simulation at the previous frequency. When sweeping the parameters in different directions, this may result in different steady-state solutions—an inherent phenomenon of a nonlinear system.

The goal parameter of interest in all of our studies is the mean velocity of the robot, which we define to be the mean displacement of the body per actuation period $T = 1/f_a$, i.e.,

$$u_{\mathrm{robot}} := \frac{x_1(t+T) - x_1(t)}{T}. \tag{4.154}$$

This definition is reasonable since we have seen before that the hammer has an oscillatory motion, and thus no net displacement.

For a given frequency, the number of periods for the integration procedure is determined iteratively until a convergence criteria is reached. This is either the absolute error threshold of $5 \times 10^{-4}\mu\mathrm{m/s}$ between to consecutive periods, or the maximal number of iterations. The latter is 300 for the first frequency, and then 100 for the next. This ensures that the system has reached steady state and yields a good compromise between accuracy and computational time.

To avoid numerical problems due to the occurring small numbers, we describe the parameters in the scaled μMKSfA unit system as shown in Tab.4.2[4].

[4]This table and other scaled unit systems can be found in the manual of the finite element software ANSYS (`www.ansys.com`)

Parameter	MKS Unit	multiply by	to obtain µMKSfAUnit
Length	m	10^6	µm
Force	N	10^9	nN
Time	s	1	s
Mass	kg	10^3	g
Pressure	Pa	10^{-3}	kPa
Velocity	m/s	10^6	µm/s
Acceleration	m/s²	10^6	µm/s²
Density	kg/m³	10^{-15}	g/µm³
Mag. Field Intensity	A/m	10^9	fA/µm
Mag. Flux Density	T	10^{-12}	(no unit descr.)
Permeability	H/m	10^{-21}	(no unit descr.)

Table 4.2: Using the scaled µMKSfA unit system rather than the MKS system allows to study phenomena at the microscale without numerical problems.

Parameter	Description	Value	Unit
ρ_{Ni}	density of nickel	8900	kg/m³
c	linear damping	1×10^{-3}	g/s
g_0	equilibrium gap	20	µm
μ	friction coefficient	0.5	-
ε	coefficient of restitution	0.5	-

Table 4.3: Constant parameters throughout the numerical analysis

Since this uses the µm as one of its base units, it represents a natural choice to model phenomena at the microscale.

The time-step for the integration dt is set to one thousandth of the actuation period, $\mathrm{d}t = 10^{-3}T$, in order to ensure sufficient temporal resolution.

4.5.2 Parameter Sets

The parameter sets investigated in this work are as follows.

For the frequency sweeps, we typically scan a frequency range of $\tilde{f} \in \{0.3, 2.25\}$ in 75 equidistant steps. The investigated parameters are the strength of the magnetic field $B = \{1, 3, 5\}$mT, the friction $\beta = \{8, 16, 32, 48, 96\}$, and the effect of the periodic clamping force with a phase shift $\varphi = (-\pi/2, 0, \pi/2)$ with respect to the magnetic force. The total length of the device is kept constant at $L_{\text{device}} = L_H + L_B + g_0 = (\alpha + 1)L_B = 300$µm, and the considered mass (and length) ratios are $\alpha \in \{0.5, 1, 1.5\}$. Table 4.3 shows parameters that are kept constant throughout the numerical analysis.

The resonant frequency is set to $f_n = 2300$Hz and the spring stiffness is calculated from $k = m_H(2\pi f_n)^2$.

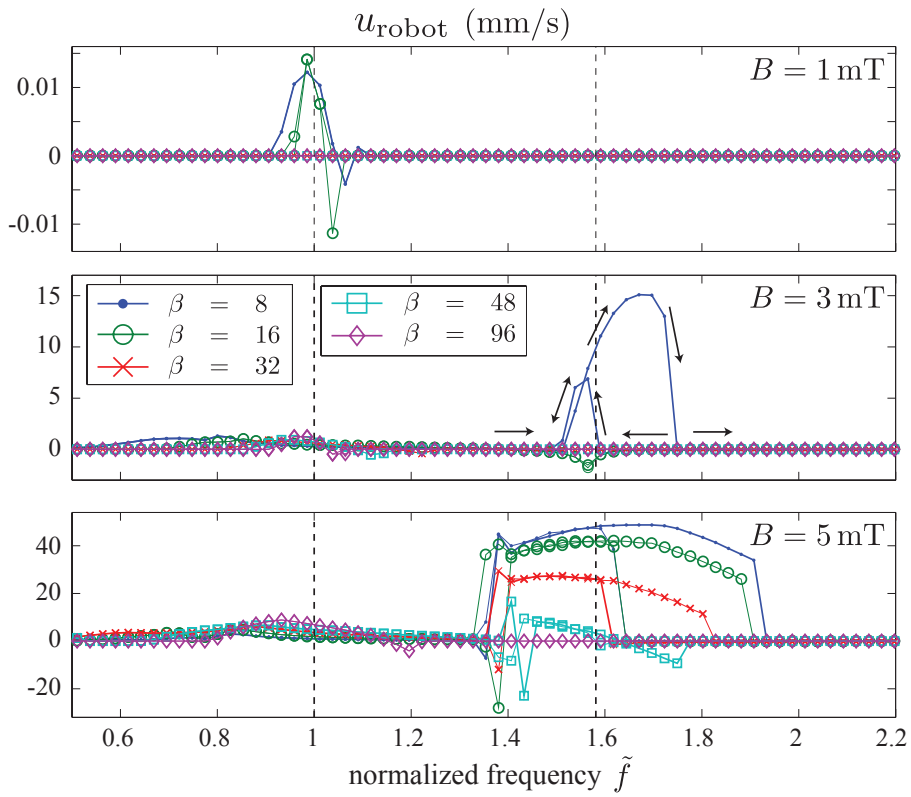

Figure 4.8: Robot velocity vs. actuation frequency for $\alpha = 1.5$ and $B = \{1, 3, 5\}$mT. The dashed vertical lines represent the resonant frequencies $\tilde{f} = 1$ and $\tilde{f} = 1.58$.

4.6 Simulation Results

We discuss the simulation results. First, we give insight into the motion principles of the device and the influence of the parameters. Then, we investigate the influence of the clamping signal.

4.6.1 No Clamping: Natural Motion Principle

For the unclamped mode ($f_c = 0$), Figure 4.8 shows the results for $\alpha = 1.5$ and $\beta = \{8, 16, 32, 48, 96\}$ for the applied flux densities $B = 1, 3$ and 5mT. The main resonant frequency for the two mass spring oscillator is $\tilde{f} = \sqrt{\alpha + 1} = \sqrt{2.5} \approx 1.58$ and is shown as vertical dotted line together with the tethered resonant frequency $\tilde{f} = 1$. Figure 4.9 shows again the results for $B = 3$mT without the plot for $\beta = 8$ and 96 to show better the behavior around $\tilde{f} = 1$.

For each applied field, we observe reversible (non-hysteretic) motion around $\tilde{f} = 1$, that has both positive and negative directions. For larger fields, $B = 3, 5$mT, we also observe peaks around $\tilde{f} = 1.58$. These are hysteretic, i.e., up-sweeping and down-sweeping the frequency does not result in the

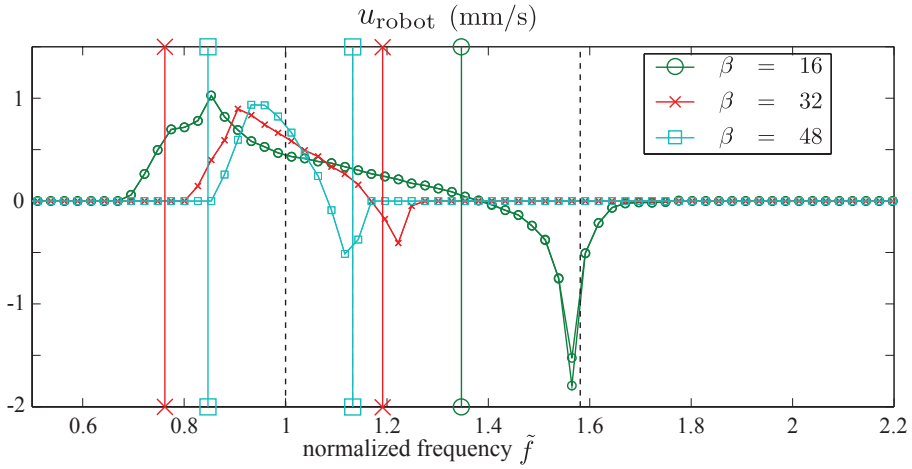

Figure 4.9: Robot velocity vs. actuation frequency for $B = 3\text{mT}$, $\alpha = 1.5$. The vertical lines represent the actuation limits from the analytical model (correspondence is through the plot marker). Note that the lower limit for $\beta = 16$ does not exist. The dashed vertical lines represent the resonant frequencies $\tilde{f} = 1$ and $\tilde{f} = 1.58$.

same velocity. This is indicated by the arrows for $B = 3\text{mT}$ and $\beta = 8$. The same can be observed for $B = 5\text{mT}$ and $\beta = 8, 16, 32$. This hysteretic behavior corresponds very well with empirical observations by Vollmers et al. [2008].

We also see that for increasing friction (increasing β) the magnitude of the velocity decreases for the frequency range around $\tilde{f} = 1.58$ and vanishes for sufficiently large values of β. On the other hand, for the range around $\tilde{f} = 1$, the magnitude of the velocity remains relatively constant, and only the frequency range decreases with increasing β. This can also be seen in Fig. 4.9 together with the corresponding frequency limits for the actuation as derived by the analytical model. We can observe that the analytical limits (4.124) and (4.125) correspond fairly well to the actual limits (correspondence is through color or the markers at the top/bottom of the vertical lines).

The motion principle can be observed in phase plots showing the gap versus the velocity of the body. Figure 4.10 shows these phase plots for $\tilde{f} = \{1, 1.58\}$, that is, for both the tethered and the two-mass-spring resonant frequency and for varying β. In both cases, the motion is periodic as predicted by the analytical model. However, we observe a fundamental difference in the phase plots and hence in the actuation principle. For the frequency range around $\tilde{f} = 1$, the motion is a stick-slip motion identifiable by the horizontal lines corresponding to $\dot{x}_1 = 0$. For the range around $\tilde{f} = 1.58$, impact occurs, identifiable by the vertical line and the corresponding velocity jump. However, note that the occurring impact does not necessarily means that the body is pushed forward by the hammer. In fact, the velocities in Fig. 4.8 are mostly in the positive direction, indicating that the hammer is pulling the body.

This finding is in clear contrast to the speculations by Vollmers et al. [2008] and Frutiger et al. [2010], where it is assumed that the impact of the hammer onto the body breaks the static friction of the body and moves it forward, e.g. the hammer *pushing* the body. Instead, our results indicate that natural motion may occur by pure sliding (for low β around $\tilde{f} = 1$) or stick/slip motion of the body (larger β, $\tilde{f} = 1$), or by impact ($\tilde{f} = \sqrt{1+\alpha}$), still the latter occurring through the hammer *pulling* the body.

Our results also show that for the right field/friction combination motion in both directions is possible when sweeping the frequency. Figure 4.11 shows the phase plots for frequencies where positive and negative net motion is observed for $\beta = 48$ and $B = 5$mT. No fundamental difference can be observed to explain forward and backward motion for the individual frequency ranges. This indicates the sensitivity of the device to small changes in the environment, especially on the friction.

Figure 4.12 shows the effect of the mass ratio α for $B = 5$mT. Because the resonant frequencies $\tilde{f} = \sqrt{1+\alpha}$ for the two mass spring oscillator decrease with decreasing α, and because the actuation range around those frequencies is relatively large, these areas for small α merge with the actuation areas around $\tilde{f} = 1$ and show an erratic behavior. Again positive and negative motion directions are possible. For certain β, only positive, for certain only negative, and for certain, the velocity changes direction with changing frequency. Also, for smaller α, motion for a larger friction range is possible.

From these results, we conclude that the mass ratio α and the friction represented by β influence significantly the frequency range of motion of the device. This is interesting for multi-agent control scenarios, i.e., where multiple devices are actuated on the same substrate. Yet, rather than focusing only on designing the resonant frequencies appropriately through α (or equivalently through the spring stiffness k) as suggested previously by Frutiger et al. [2010], the friction in the system has to be taken into account as well.

4.6.2 Effect of Clamping

Figure 4.13 shows the results when a periodic clamping force with a phase shift φ with respect to the magnetic signal is applied to the body (see (4.153)). The other parameters are set as $\alpha = 1.5$, $B = 5$mT, and we show the results for $\beta = 8$ and 96, together with the respective curve for no clamping as a reference.

We observe for $\beta = 8$ that the actuation range is shifted to lower frequencies, from $\tilde{f} = 1.58$ to about $\tilde{f} = 1.2$. The net maximal velocity remains about the same as in the no-clamping case for $\varphi = \pm\pi/2$. Clearly, changing φ from $-\pi/2$ to $\pi/2$ reverses the direction of the velocity. The motion in this cases is rather smooth and also changes direction for changing frequencies (keeping φ constant). A slight hysteresis is observed for $\varphi = \pi/2$ around $\tilde{f} = 1.1$. For $\varphi = 0$, higher velocities are possible, however, we also observe erratic motion between $\tilde{f} = 1.2$ and 1.58, that is, exactly in the range of smooth motion for

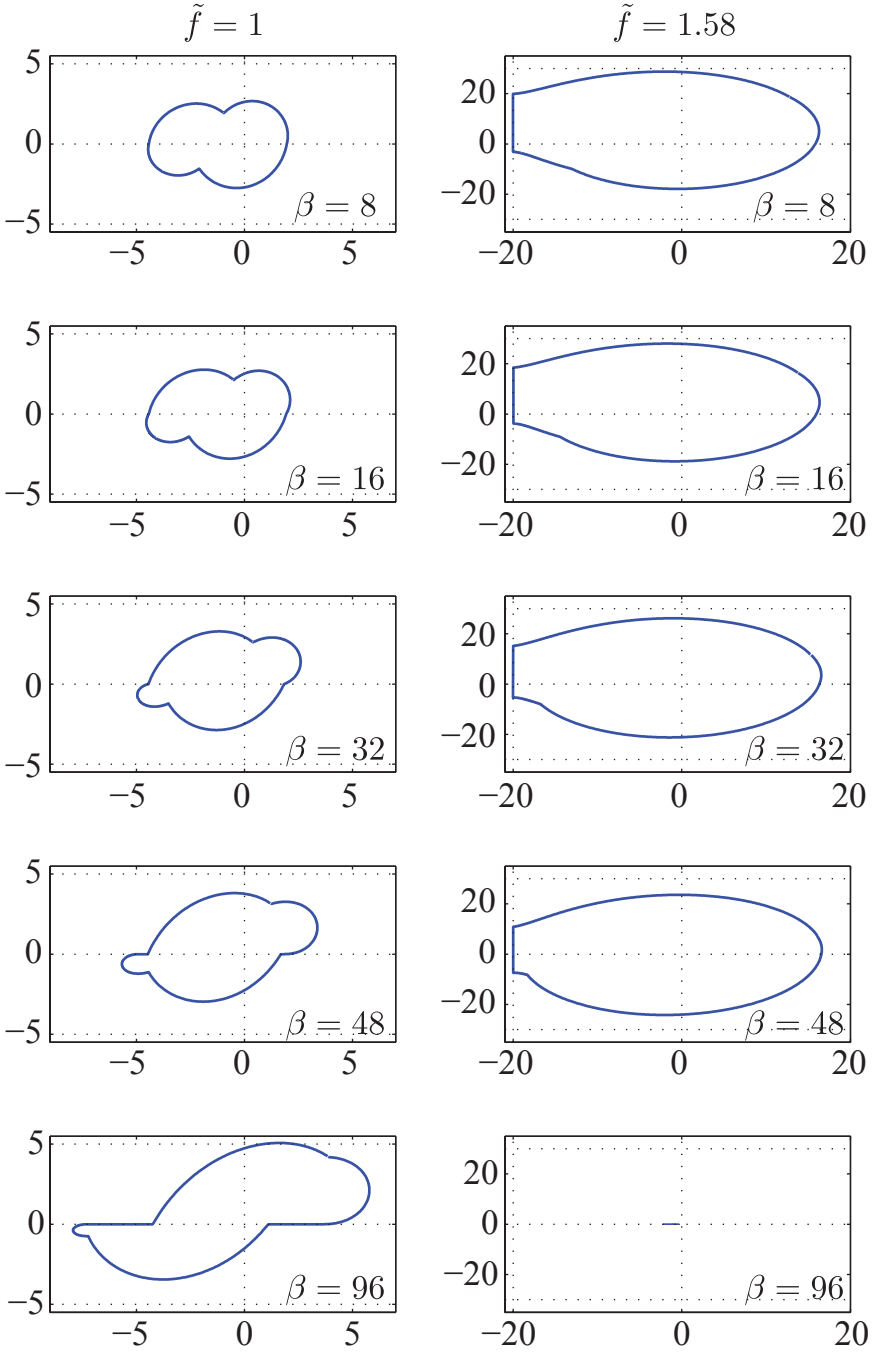

Figure 4.10: Phase plots for $\tilde{f} = 1$ (left column) and $\tilde{f} = \sqrt{1+\alpha}$ (right column) with $\alpha = 1.5$ and $B = 5$mT. The vertical axis is the velocity of the body, $\dot{x}_1$ in mm/s, and the horizontal axes is the gap between the body and the hammer, $g_{N2} = x_2 - x_1 - g_0$ in µm. The rows correspond to increasing β, thus friction in the system. For motion at $\tilde{f} = 1$, we can identify oscillatory sliding ($\beta = 8, 16, 32$) or stick/slip behavior ($\beta = 48, 96$). At $\tilde{f} = 1.58$ impact can be observed, even though the net motion does not occur by the hammer pushing the body, but rather the hammer pulling on it. For $\beta = 96$ no motion occurs for $\tilde{f} = 1.58$.

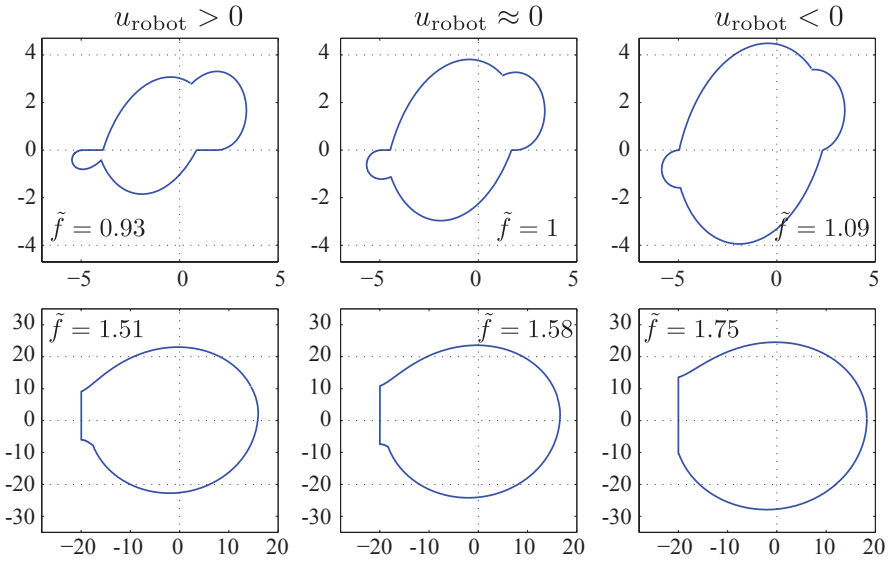

Figure 4.11: Phase plots around $\tilde{f} = 1$ (top row) and $\tilde{f} = 1.58$ (bottom row) for $\beta = 48$ and $B = 5$mT. The vertical axes is again the velocity of the body, $\dot{x}_1$ in mm/s, and the horizontal axes is the gap between the body and the hammer, $g_{N2} = x_2 - x_1 - g_0$ in µm. In the left column, we have positive net motion of the robot, in the middle column negligible net motion occurs, and in the right column there is negative net motion. Yet, no significant difference is observable in the motion mechanism.

$\varphi = \pm\pi/2$. Smooth motion occurs around $\tilde{f} = 1.58$ and higher. Thus, for the same frequency, we can have both smooth motion ($\varphi = \pm\pi/2$) or erratic or even no motion ($\varphi = 0$). This effect has been described by Frutiger et al. [2010]. Finally, we also observe that for $\varphi = 0$ changing the frequency does not lead to change in the direction of the velocity.

For $\beta = 96$, we see that compared to the no clamping case, the frequency of actuation remains constant and that the overall velocity is increased. Again, the velocity is smooth and changes direction when switching φ between $-\pi/2$ and $\pi/2$. For these cases, the motion is unidirectional. On the other hand, for $\varphi = 0$, we observe smooth motion, with changing velocity directions as the frequency is changed. Around $\tilde{f} = 1$ the motion may stop completely, again an effect described by Frutiger et al. [2010].

Figure 4.14 shows the continuous variation of φ from $-\pi/2$ to $\pi/2$ for the two cases of $\beta = 96, \tilde{f} = 1$ and $\beta = 8, \tilde{f} = 1.58$. Clearly, a phase shift from $-\pi/2$ to $\pi/2$ induces a change in the velocity direction with about the same magnitude. However, this change may occur monotonically (for $\beta = 96, \tilde{f} = 1$) or show an optimum as in the case of $\beta = 8, \tilde{f} = 1.58$ around $\varphi = 0$. Interestingly, we remark that the phase shift that leads to a maximum velocity of the robot for $\beta = 8$, is very close to the phase shift that will stop its motion for $\beta = 96$.

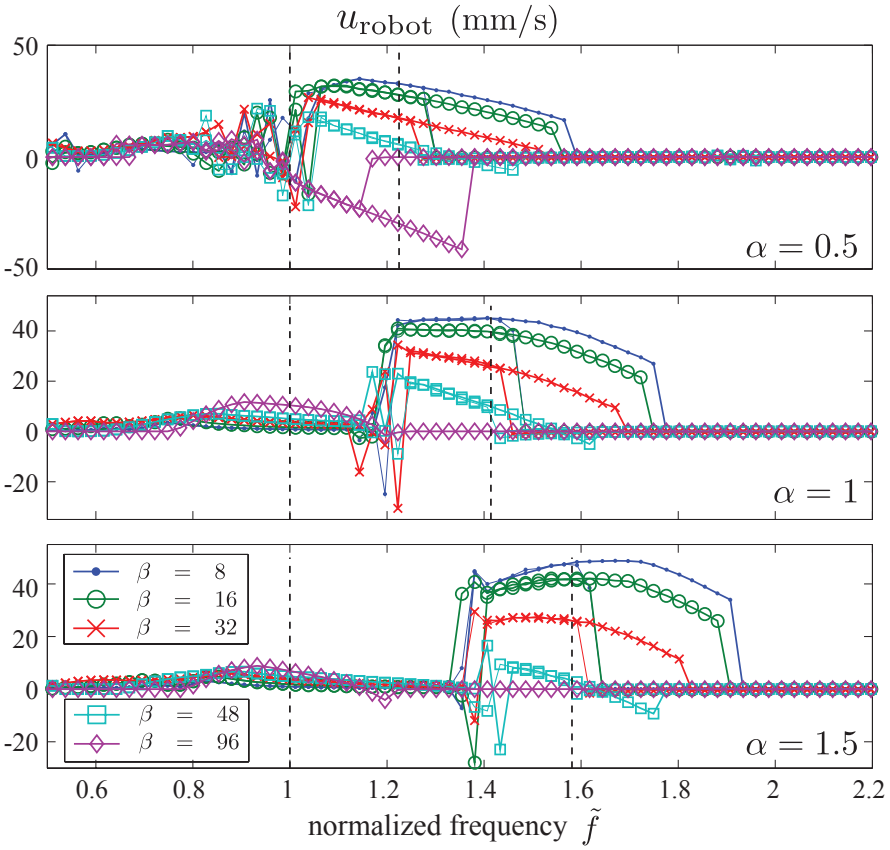

Figure 4.12: The effect of the mass ratio α for $B = 5$mT. The dashed vertical lines represent the resonant frequencies $\tilde{f} = 1$ and $\tilde{f} = \sqrt{1+\alpha}$. We can observe how the actuation range around the decreasing resonant frequency $\tilde{f} = \sqrt{1+\alpha}$ merges with those around $\tilde{f} = 1$ resulting in an increasingly erratic behavior with decreasing α.

Now, our model allows further insight and we can observe the effect of clamping in the phase plots shown in Fig. 4.15. In (a), we have $\beta = 96$ and $\tilde{f} = 1$. We observe that the stick/slip motion remains the driving mechanism. However, clamping acts to rectify based on the phase shift φ. For $\varphi = -\pi/2$ the body is only moving in the negative direction, while for $\varphi = \pi/2$ only in the positive direction. This, and the larger motion amplitude explain the increase in the overall velocity of the robot. In these two cases, the bidirectional stick/slip motion is transformed into a unidirectional stick/slip motion of the body. For $\varphi = 0$, we have positive and negative motion of the body, showing basically a snap-shot of the transition from positive only to negative only motion.

In Fig. 4.15(b),we have $\beta = 8$ and $\tilde{f} = 1.58$, and we can identify the impact driven motion for the no clamping case. However, in the clamping cases, we

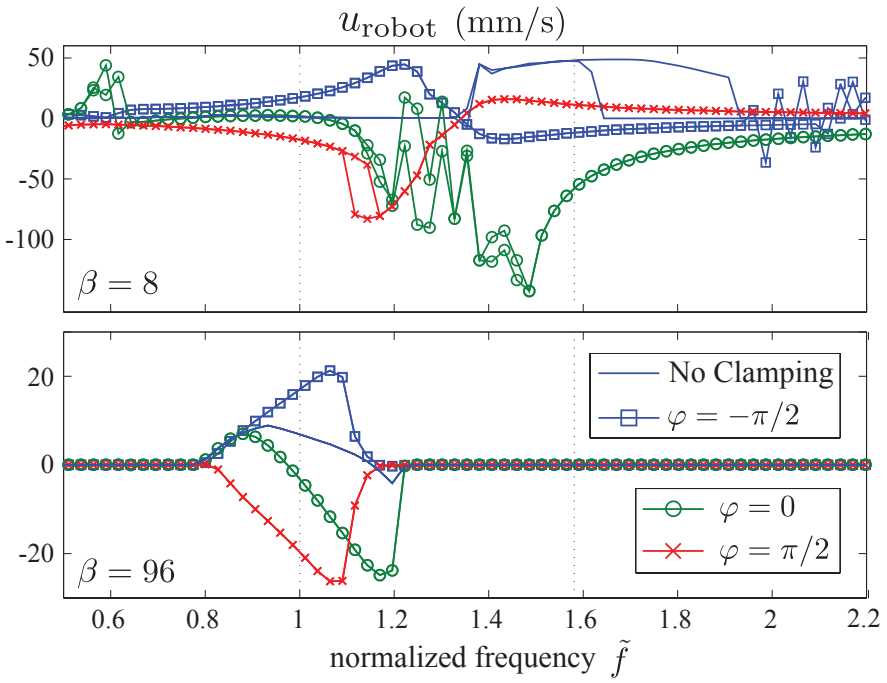

Figure 4.13: The effect of the clamping signal. For low friction ($\beta = 8$), the actuation range is shifted to lower frequencies. For larger friction ($\beta = 96$) the net velocity is increased. For a given frequency, changing the phase shift φ from $-\pi/2$ to $\pi/2$ changes the direction of the velocity. Still, for low friction, for $\varphi = -\pi/2$ or $\varphi = \pi/2$, sweeping the frequency also changes the direction of the velocity. No phase shift $\varphi = 0$ induces erratic motion for low friction at frequencies where smooth motion was observed before (around $\tilde{f} = 1.2$), followed by smooth motion for $\tilde{f} = 1.58$ and higher. For $\beta = 96$, no phase shift leads to smooth motion that is bidirectional when the frequency is swept.

see stick/slip motion with much smaller body velocities. The motion of the body has again been rectified by the clamping force as the sliding is mostly only in one direction, positive for $\varphi = \pi/2$, and negative for $\varphi = 0, -\pi/2$. Thus, the clamping force has changed the motion mechanism from impact to stick/slip driven motion. For this case, the lower body velocities still lead to net velocities comparable to the no clamping case.

Note, that this finding, especially the one for the impact case, indicates that clamping has a different effect of what has been speculated by Vollmers et al. [2008] and Frutiger et al. [2010]. There, it was thought that impact allows for clamping down the body and thus to achieve higher impact velocities of the hammer and thus larger propulsion of the robot. Our results indicate that impact may be completely eliminated, and the effect of clamping is a change from impact driven to a stick/slip motion.

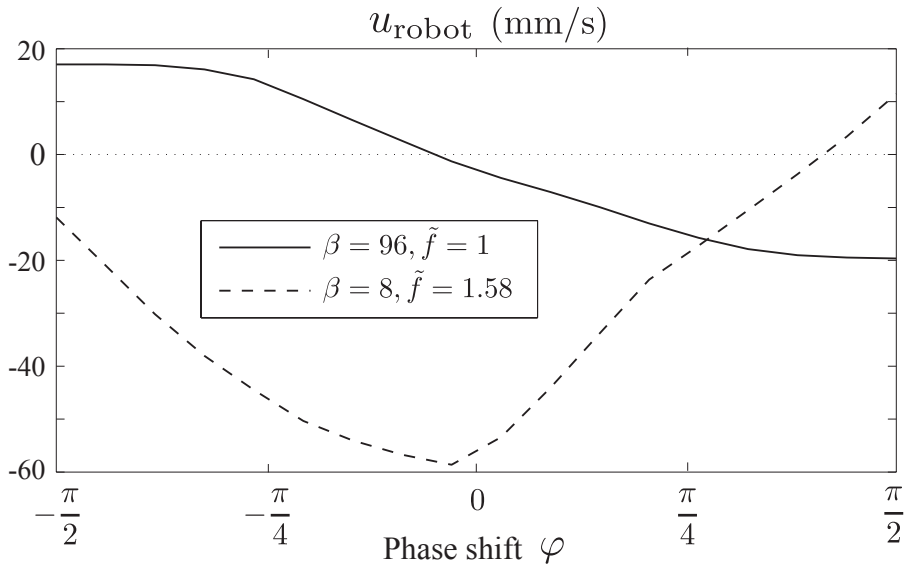

Figure 4.14: Influence of the clamping phase shift φ for two special cases. Clearly, a phase shift from $-\pi/2$ to $\pi/2$ induces a change in the velocity direction with about the same magnitude. However, this change may occur monotonically (for $\beta = 96, \tilde{f} = 1$) or show an optimum as in the case of $\beta = 8, \tilde{f} = 1.58$ around $\varphi = 0$.

To conclude, clamping has a significant effect on the velocity of the robot. It acts by inducing a stick/slip regime to the body independently of its no clamping motion mechanism. A phase shift of $\varphi = \pm\pi/2$ rectifies the oscillatory motion of the body and leads to a smoother motion of the robot. Moreover, in the frequency range around the resonant frequency $\tilde{f}$ of the tethered device, the velocities are increased and the motion still remains smooth. This suggests that this configuration is useful for controlled and repeatable motion.

4.7 Summary and Contributions

This chapter has reviewed the mathematical background of non-smooth dynamics necessary for modeling the motion of complex microrobots in general, and the Wireless Resonant Magnetic Microactuator (WRMMA) or MagMite in particular. We gave an overview of the WRMMA system and the occurring forces in it.

We then integrated the non-smooth equations of motion numerically and derived the frequency/velocity curves of the robot which are qualitatively consistent with the experimental findings by Vollmers et al. [2008] and Frutiger et al. [2010]. These include a shift of the actuation frequency between the tethered and the untethered mode, the occurrence of the change of the direction of the velocity with changing frequency, and the rectifying effect of the

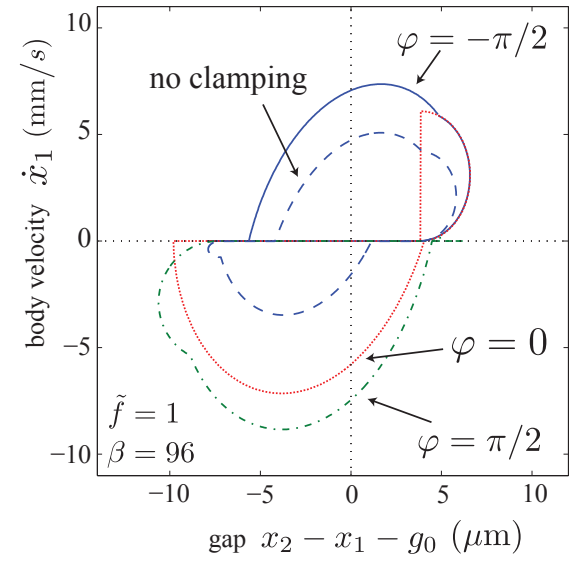

(a) $\tilde{f} = 1, \beta = 96$

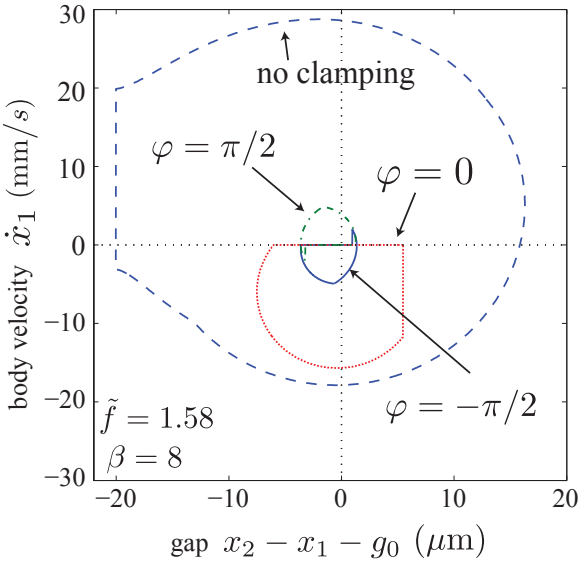

(b) $\tilde{f} = 1.58, \beta = 8$

Figure 4.15: The effect of clamping shown in the phase plots ($\alpha = 1.5$, $B =$ 5mT). We see that clamping changes the motion mechanism fundamentally. In (a) the stick/slip motion remains but is rectified from bidirectional (no clamping) to unidirectional ($\varphi = \pm\pi/2$). In (b) there is a change from impact driven to stick/slip motion.

clamping force.

This chapter has mainly four general contributions. For one, we propose an analytical model around the resonant frequency of the tethered device, allowing us to identify non-dimensional and characteristic parameters of the system that help comparing different designs. Furthermore we can predict the frequency range in which motion will occur. This range corresponds well with the numerical findings. We have also shown that the magnetic force between the body and the hammer varies insignificantly as long as the total magnetic volume is the same. Thus, the magnetic force itself does not contribute to variations in the behavior of the devices with same total magnetic volume.

Second, a numerical parameter study to investigate and predict the overall behavior of the microrobot. This is only possible numerically, given the large variations in the fabrication of the devices and the large number of experimental parameters that need to be controlled. We identified two main regions of motion: around $\tilde{f}$ and $\sqrt{1+\alpha}\tilde{f}$. Around $\tilde{f}$, we have smooth motion stemming from stick/slip behavior, around $\sqrt{1+\alpha}\tilde{f}$, the motion is impact driven, may be hysteretic or even non-predictable/erratic. For small mass ratios, these regions overlap. For large ones, they are separated. To profit from the smooth motion around $\tilde{f}$, the mass ratio should be increased. At the same time, using clamping, the overall velocity is increased resulting in smooth, repeatable velocities, that can controllably change the direction by changing the frequency.

Third, using the numerical results, we can explain the motion mechanism of the WRMMA, which is impossible using current experimental methods due to the high frequency oscillations and simultaneous net motion. We show that there are two fundamentally different mechanisms, a stick/slip motion around the resonant frequency of the tethered device, and a much faster, impact driven motion around the resonant frequency of the two-mass oscillator. We also show that the impact may not lead to the expected forward impulse transfer; rather the pulling of the hammer dominates. This is in contrast with the speculations by Vollmers et al. [2008] and Frutiger et al. [2010] which are based on experimental observations of the overall velocities only.

Fourth, our results also suggest that the effect of clamping is different than it was thought before, namely to clamp down the robot to achieve higher impact velocities and thus higher net velocities and smoother motion of the robot. We see that the effect of clamping is to transform the motion mechanism to stick/slip motion and rectification occurs by fixing the robot during forward or backward sliding for the right phase shift. Experimentally, the exact same effect has been observed which indicates the validity of our results.

Finally, considering multi-agent control scenarios, we found that the large driving frequency ranges can be reduced by the friction. We can conclude that not only the mass ratio (or equivalently the resonant frequency) is the important parameter to separate driving regions of individual robots. In-

stead, one must consider the friction (represented by β) as well. Increasing the normal force, thus β on the device can be done by a small constant clamping force sufficiently small not to stop the device completely. Of course, when designing robots, care must be taken to avoid that the multiple individual frequency ranges of motion overlap. Again, the friction helps here to reduce this range.

To conclude, we have successfully applied non-smooth multi-body dynamics to describe the motion of a complex microrobot. We have given the general theory to describe motion including planar friction and frictional impact with unilateral contacts. It is believed that this method is readily applied to other microrobots as well, as it does not contain any specificities. On the contrary, mechanical systems with friction and frictional impacts are amongst the most complex ones, thus the method described herein will apply to a large range of different microrobots and will guide through their design and actuation phase.

4.8 References

Andrews, M., Harris, I., and Turner, G. (1993). A comparison of squeeze-film theory with measurements on a microstructure. *Sensors and Actuators A: Physical*, 36(1):79 – 87.

Beleggia, M., De Graef, M., and Millev, Y. T. (2006). The equivalent ellipsoid of a magnetized body. *J. Physics D*, 39(5):891–899.

Brugger, S. and Paul, O. (2010). Magnetic field amplification by slender cuboid-shaped magnetic concentrators with a single gap. *Sensors and Actuators A: Physical*, 157(1):135 – 139.

Cheng, C.-C. and Fang, W. (2005). Tuning the quality factor of bulk micromachined structures using squeezed-film damping. *Microsystem Technologies*, 11:104–110.

Frutiger, D. R. (2010). *MagMites: Design, Fabrication, and Control of Wireless Resonant Magnetic Micromachines for Dry and Wet Environment*. PhD thesis, ETH Zurich.

Frutiger, D. R., Kratochvil, B. E., Vollmers, K., and Nelson, B. J. (2010). Small, fast, and under control: wireless resonant magnetic micro-agents. *Int. J. Robotics Research*, 29(5):pp. 613–636.

Glocker, C. (2001). *Set-Valued Force Laws*, volume 1 of *Lecture Notes in Applied Mechanics*. Springer Verlag, Berlin, Heidelberg, New-York.

Glocker, C. and Studer, C. (2005). Formulation and preparation for numerical evaluation of linear complementarity systems in dynamics. *Multibody System Dynamics*, 13(4):447–463.

Leine, R. and Nijmeijer, H. (2004). *Dynamics and Bifurcations of Non-Smooth Mechanical Systems*, volume 18 of *Lecture Notes in Applied and Computational Mechanics*. Springer Verlag, Berlin, Heidelberg, New-York.

Leine, R. and van de Wouw, N. (2008). *Stability and Convergence of Mechanical Systems with Unilateral Constraints*, volume 36 of *Lecture Notes in Applied and Computational Mechanics*. Springer Verlag, Berlin, Heidelberg, New-York.

Mita, M., Arai, M., Tensaka, S., Kobayashi, D., and Fujita, H. (2003). A micromachined impact microactuator driven by electrostatic force. *J. Microelectromech. Syst.*, 12(1):37–41.

Moreau, J. (1988). Unilateral contact and dry friction in finite freedom dynamics. In Moreau, J. and Panagiotopoulos, P., editors, *Non-Smooth Mechanics and Applications*, volume 302 of *CISM Courses and Lectures*, pages 1–82. Springer Verlag, Wien.

Pawashe, C., Floyd, S., and Sitti, M. (2009). Modeling and Experimental Characterization of an Untethered Magnetic Micro-Robot. *Int. J. Robotics Research*, 28(8):1077–1094.

Transeth, A. A., Leine, R. I., Glocker, C., and Pettersen, K. Y. (2008). 3-d snake robot motion: Nonsmooth modeling, simulations, and experiments. *IEEE Trans. on Robotics*, 24(2):361–376.

Vollmers, K., Frutiger, D. R., Kratochvil, B. E., and Nelson, B. J. (2008). Wireless resonant magnetic microactuator for untethered mobile microrobots. *Applied Physics Letters*, 92(14):144103–3.

Zhao, X., Dankowicz, H., Reddy, C. K., and Nayfeh, A. H. (2004). Modeling and simulation methodology for impact microactuators. *J. of Micromechanics and Microengineering*, 14(6):775–784.

Maybe an asteroid will hit or something will happen to the magnetic polar fields, ... Or maybe the guy who was making calendars ran out of paper. Who knows?

George Noory (b. 1950) American radio talk show host

CHAPTER 5

Summary and Contributions

In this thesis we presented the necessary background to understand and predict the magnetization, torque, and motion of soft-magnetic bodies when placed in externally applied magnetic fields. From an engineering perspective, we provided methods and results that help build intuition and that guide during the design of complex untethered soft-magnetic microrobots.

We have generalized the computation procedure for the magnetization. Capitalizing on this, we have converted it from an unstructured minimization to a root-solving problem. We proposed an interpretation of the root and derived its boundaries, allowing us to derive boundaries on its dependent quantities.

We also derived two approximations of the root. This allows us to decrease computation times considerably, which in turn allows for real-time model-based controllers. The advantage of our method is that the standard results are obtained as limit cases, and the transition between these limits can be investigated analytically.

Next, we used our description to investigate and analyze the torque resulting on a single soft-magnetic shape when placed in an external field. We demonstrated that the standard results are obtained by limit considerations. In addition, based on the boundary of the root, we can derive minimal torque values, allowing for design considerations. We can also predict that for fields applied at angles smaller than 45°, the torque will always increase with the applied field and asymptotically reach its large field limit.

Then, we investigated superposition on shapes and gave phenomenological arguments that in most of the cases superposition can be neglected. We argued that configurations may exist where one or just a few shapes dominate the total torque on assembled structures. As a consequence, we propose that assembled devices should be modeled as the superposition of simple geometries, and validate this experimentally and numerically with a micro-

robot assembled from electroplated nickel parts.

After this, we turned our investigations to the motion of complex microrobots and proposed to use results from non-smooth multi-body system to model their behavior. The applied method allows for the investigation of systems that include friction, and frictional impact between an arbitrary number of bodies.

As an example, we studied the Wireless Resonant Magnetic MicroActuator that is driven by oscillating fields in the kHz range. The proposed numerical method is the sole method for gaining further insight into the actual propulsion mechanism. For this, we analyzed the system analytically and derived frequency limits for actuation. Then, using a numerical parameter study, we identified two main regions of motion, showing two fundamentally different motion mechanisms, stick/slip and impact driven, which are in clear contrast to previous speculations based on observations of the overall velocities of the robot.

The applied method can be readily used to model other microrobots. As mechanical systems with friction and frictional impacts are amongst the most complex mechanical systems to analyze, the method described in this work will apply to a large range of different microrobots and will guide engineers through their design and actuation phase.